Atomistically-informed discrete dislocation dynamics modeling of plastic flow in body-centered cubic metals

Acknowledgements

This thesis would not have been possible without the support of many people from all walks of life, to whom I would like to express my gratitude.

Firstly, I am highly indebted to Prof. Dr. rer. nat. Peter Gumbsch for giving me the opportunity to do my PhD thesis at his institute. Without his constant support and invaluable feedback and freedom to pursue new directions of research, this work would not have been possible. His enthusiasm for research and diverse interests have always been a source of motivation for me. His honest feedback on scientific writing helped me a lot in shaping my approach while writing this thesis.

I am thankful to Prof. Dr. rer. nat. Oliver Kraft for agreeing to be the second referee for my PhD work.

I would like to express my deep sense of gratitude and sincere thanks to Dr. Daniel Weygand for his valuable guidance and numerous discussions and support with the development of the DDD code for my thesis work. His feedback and suggestions led to improvement of my work.

I am grateful to Dr. Roman Gröger who provided me with the atomistic data which is input to the model developed in this work. I would also like to thank Dr. Matous Mrovec for the discussions and feedback on several aspects related to atomistic modeling.

Special thanks are due to Dr. Cecile Marichal and Prof. Helena van Swygenhoven for sharing their data on tungsten pillar experiments.

I am highly grateful to Mrs. Andrea Doer who has always been very helpful in both administrative and personal matters, in all the years which made my time at the institute easier.

I would also like to thank Dr. Stefan Sandfeld who has been a great friend since the days of my master studies and who encouraged me to pursue research.

I am also highly thankful to my former office colleague Dr. Rudolf Baumbusch for many fruitful discussions which always helped me reorganize

Abstract

The plastic flow of body-centered cubic (*bcc*) metals is controlled by the $a/2\langle 111 \rangle$ screw dislocation. An accurate description of the dynamics of screw dislocations in a mesoscale model requires a physical description of the mobility of screw dislocation. In this thesis, a computational framework for discrete dislocation dynamics simulations of *bcc* metals, which naturally accounts for core-effects on screw dislocation mobility based on atomistic simulation results, is developed. The application of the new framework is done for tungsten. The finite temperature mobility of the $a/2\langle 111 \rangle$ screw dislocation is based on the thermally-activated motion via nucleation of kink-pairs. The fundamental physical quantity controlling the kink-pair nucleation, the stress-dependent activation enthalpy, is obtained by fitting the line-tension model to atomistic data.

Many of the experimentally observed phenomena in *bcc* metals like temperature dependence of tension-compression asymmetry, orientation dependence, temperature dependence of yield stress and crystallography of slip can be explained qualitatively in terms of a single screw dislocation.

The mechanism of repulsive interaction between screw dislocations is investigated which shows that screw dislocations glide collectively maintaining an equilibrium distance between them. Local dislocation interactions directly control the activation enthalpy of a screw dislocation. From the simulations of compression on micrometer-sized pillars, a new mechanism responsible for slip on low-stressed planes called anomalous slip is identified. The mechanism attributes anomalous slip as a multi-dislocation process occurring due to the formation of cross-kinks, topological configurations generated by prior dislocation interactions. The new mechanism can account very well for the occurrence of coarse-crystallographic slip traces observed in experiments on tungsten pillars of the same geometry. The simulations also show that in addition to the screw dislocations, mixed dislocations and the local stress variations caused during their glide play a significant role during deformation of *bcc* metals.

Zusammenfassung

Die Plastizität kubisch-raumzentrierter (krz) Metalle wird maßgeblich durch $a/2\langle 111\rangle$-Schraubenversetzungen beeinflusst. Um die Dynamik von Schraubenversetzungen zu beschreiben, muss ein physikalisch basiert-es Modell der der Mobilität der Schraubenversetzung entwickelt und implementiert werden. Dieser Ansatz ermöglicht es für krz Metalle allgemeingültig die Versetzungsdynamik basierend auf der Mobilität der Schraubenversetzungskerne zu modellieren, basierend auf atomistischen Ergebnissen. Die temperaturabhängige Mobilität der Schraubenversetzungen resultiert aus dem thermisch aktivierten Mechanismus der Kinkenpaarbildung. Die für Kinkenpaarbildung maßgebliche physikalische Größe ist die spannungsabhängige Aktivierungsenthalpie, welche durch Anpassung eines Linienspannungs-Modell an atomistische Daten parametrisiert wurde. Viele experiment-ell bekannte Phänomene der krz Metalle, wie die Temperaturabhängigkeit der Zug-Druck-Asymmetrie, die Orientierungs- und Temperaturabhängig-keit der Fließspannung, sowie die kristallographischen Eigenarten der Gleitprozesse sind in diesem Modell qualitativ auf das Verhalten der einzelnen Schraubenversetzungen zurückführbar.

Die Eigenschaften der abstoßenden Wechselwirkung zwischen Schraubenversetzungen wurde analysiert, und es lässt sich zeigen, dass Schraubenversetzungen kollektiv gleiten, wobei sich Gleichweichtsabstände zwischen ihnen einstellen. Die Aktivierungsenthalpie einer Schraubenversetzung hängt stark von der Wechselwirkung mit anderen Versetzungen ab. Anhand Simulationen von Druckversuchen mikrometergroßen Säulen konnte ein neuer Mechanismus identifizeirt werden, der für das sogenannte Phänomen der anomalen Gleitung („anomalous slip") verantwortlich ist, also für die Gleitprozesse auf Ebenen niedriger Spannung. Der Mechanismus erklärt anomales Gleiten als einen Mehr-Versetzungs-Effekt, im Zusammenhang mit der Bildung von sogenannten "Cross-Kinken", deren Topologie die Folge vorangegangener Versetzungsreaktionen ist. Der vorgeschlagene Mechanismus harmoniert bestens mit der Ausbildung kristallographischer Gleitbänder, die experimentell an Wolfram-Säulen mit vergleichbarer Geometrie beobachtet wird. Die Simulation zeigt ferner, dass nicht nur reine Schraubenversetzungen, sondern auch solche mit gemischtem Charakter einen erheblichen Einfluss auf die plastischen Prozesse in Wolfram-Säulen haben.

Contents

Abbreviations

bcc	Body-Centered Cubic
BOP	Bond Order Potential
C-D-S	Co-planar Double Slip
CRSS	Critical Resolved Shear Stress
DDD	Discrete Dislocation Dynamics
DFT	Density Functional Theory
EAM	Embedded-Atom Method
EI	Elastic Interaction
FEM	Finite Element Method
fcc	Face-Centered Cubic
FS	Finnis-Sinclair potential
hcp	Hexagonal Close Packed
MD	Molecular Dynamics
MRSSP	Maximum Resolved Shear Stress Plane
NEB	Nudged Elastic Band
PK	Peach-Koehler
SE	Surface-Effect
TEM	Transmission Electron Microscopy

Nomenclature

a_0	Lattice constant
a	Distance between Peierls valleys
ν_D	Debye frequency
$\mathbf{b}$	Burgers vector
μ	Shear modulus
χ	MRSSP angle
ψ	Planes at 60° to the $(\bar{1}01)$ plane
$\bar{\psi}$	Macroscopic slip plane angle
Σ	Stress tensor in MRSSP coordinate system
τ	Stress parallel to glide direction in MRSSP coordinate system
σ	Stress perpendicular to glide direction in MRSSP coordinate system
u	Displacement field
$\mathbf{t}$	Traction force
ΔH	Activation enthalpy
ΔH_C	Scaling enthalpy term
ΔH_{hb}	Activation enthalpy of habit plane
ΔH_{cs}	Activation enthalpy of cross-slip plane
η	Loading ratio in MRSSP
α	Reference slip system
$\mathbf{m}_\alpha$	Reference slip direction
$\mathbf{n}_\alpha$	Reference slip plane normal
α	Reference slip system
λ	Angle between loading direction and [111] direction
ρ	Dislocation density
ξ	Dislocation coordinate
ξ_0	Initial position of straight screw dislocation
ξ_c	Dislocation position at critical kink-pair configuration
V	Peierls potential
Δz	Height of kink pair
$\mathbf{R}$	Position vector

T	Temperature
T_K	Knee temperature
$\hat{T}$	Upper bend temperature
$\breve{T}$	Lower bend temperature
τ_P	Peierls stress
$\tau_P^{\{112\}}$	Peierls stress on $\{112\}$ planes
k_B	Boltzmann constant
L	Length of screw dislocation
l_c	Critical kink-pair
γ	Shear-strain

1. Introduction

Metals have been the milestones marking the progress of human civilization ever since the bronze age. A precursor to designing new metals with enhanced mechanical properties is an understanding of the fundamental mechanisms governing its deformation. Conventional metals research has largely been experimental in nature, relying on experience and intuition, to carefully deduce and formulate laws governing material behavior. The Schmid law [1] is a classical example of such a law, which can still be reliably used to predict the onset of plastic flow in hexagonal-close packed (*hcp*) and face-centered cubic (*fcc*) metals. Extensive experimental testing was still required to gain further insights into the underlying mechanisms governing the strength of a metal.

With the advent of computing power over the last fifty years, computational material science has evolved as an indispensable tool for research and a reliable counterpart to experiments. A computer simulation has at its heart a computational model, which critically affects the ability to capture and describe the physical phenomena that are investigated. To understand the mechanisms of dislocation plasticity, computer modeling has been widely used to investigate the properties of single dislocations. The benefits of computer based modeling are manifold. Not only does this approach help save time and money by reducing the number of experiments, but also allows to investigate the material properties by varying a wide range of parameters in a controlled manner not possible in experiments. This helps identify the critical parameters affecting the mechanical behavior of materials. It also allows to investigate and identify the microscopic laws governing dislocation motion like the relation between the stress and velocity of a dislocation, which can then be incorporated as constitutive laws into discrete dislocation dynamics (DDD) models. Since

such laws cannot always be deduced directly from experiments and are too complicated to be derived analytically, computer models remain the only means to study these processes. In the end, validation experiments serve as the ultimate benchmark for the predictions of a computational or theoretical model.

Critical aspects of metal plasticity are governed by the long-range elastic strain fields of dislocations which can be accurately described by continuum linear elasticity theory. It is however known that unlike in *fcc* metals, where yielding follows the predictions of the Schmid law, body-centered cubic (*bcc*) metals exhibit a much more complicated response to applied stress. This observed difference in mechanical properties raises a fundamental question: What is the origin of the difference between the properties of *bcc* and other close-packed metals since the elastic fields of dislocations are independent of the underlying crystal structure [2]. It is the answer to this critical and long-standing question that has been one of the most significant achievements of the computer modeling.

Using atomistic simulations, it has been established that the $a/2\langle 111 \rangle$ screw dislocation core is non-planar due to its extension onto the $\{110\}$ planes of its zone [3](see [4–6] for review). This concept of a non-planar screw dislocation core, first proposed by Hirsch [7], is fundamentally different from the planar core structures in *fcc* metals. The non-planar character results in two peculiar properties of the dislocation core, firstly, the dislocation core is sessile and requires large stresses to move the dislocation and secondly, components of stress other than glide stresses also influence the behavior of screw dislocations and thereby influence the yielding. The latter is also referred to as non-Schmid stress and collectively they are a characteristic feature of *bcc* metals. Owing to the large stresses required to move screw dislocations, they are assumed to govern the plastic flow in *bcc* metals. Additionally, the large stresses may be overcome by the stress-assisted thermally activated formation of kink-pairs and their subsequent propagation along the screw dislocation line. This thermally activated glide mechanism is called the kink-pair mechanism [8].

Coarse-grained simulation methods like the discrete dislocation dynamics (DDD) are widely used to study the collective motion of dislocations and understand the mechanisms responsible for plastic flow in metals. At the mesoscale of DDD, the phenomena of interest are the arrangement and

formation of dislocation patterns which arise primarily from collective motion and interaction of dislocations. These interactions are governed by the long-range fields of dislocations. The most critical input to a DDD simulation is a constitutive relation describing the relation between stress and the dislocation mobility. An accurate description of the dislocation mobility is the first step in understanding the collective motion and interaction of dislocations and achieving the ultimate aim of identifying statistically averaged quantities that can be compared to macroscopic experiments or transferred to a crystal plasticity model. Due to the dominant role played by the dislocation core in the dynamics of individual $a/2\langle 111\rangle$ screw dislocations in *bcc* metals, a multiscale approach is required which provides a simplified description of the relevant atomistic information.

1.1. Objectives of this work

The focus of the current work is to develop and implement a multiscale model that can account for the core-effects on $a/2\langle 111\rangle$ screw dislocation mobility observed on the atomistic scale [9,10] in a DDD simulation tool. Accordingly, this thesis is divided as follows: The physical and numerical aspects of the computational model, suitable for use in the DDD simulation tool are presented on the example of tungsten. Mobility rules for the $a/2\langle 111\rangle$ dislocations are based on the kink-pair mechanism. The stress components which critically influence the activation parameters of a screw dislocation at finite temperatures in a *bcc* metal, including the effects on the dislocation core structure, are accounted for. The fundamental physical quantity controlling the kink-pair nucleation, the stress-dependent activation enthalpy, is obtained by fitting the line-tension model to the atomistic data extending the approach by Gröger et al. [9–11]. It is demonstrated that such an atomistic based description of dislocation mobility provides a physical basis to naturally explain many experimentally observed phenomena in *bcc* metals like the tension-compression asymmetry, orientation dependence of loading, temperature dependence of yield stress and the crystallography of slip.

Once the essential aspects of the models for an isolated screw dislocation are presented, the influence of dislocation-dislocation interactions on the

activation parameters of a screw dislocation is examined. Repulsive interaction between two screw dislocations is studied since the mechanistic details of how they interact are not yet understood. The interaction between mixed and screw dislocations is also investigated and its significance within the context of *in situ* experiments is discussed.

Finally, the response of micrometer sized pillars with randomly distributed initial dislocation-sources in both tension and compression is examined for middle-oriented pillars. The results of the simulations are in good agreement with concurrent experiments performed on micropillars at the Paul-Scherrer Institute, Switzerland. A new mechanism for anomalous slip is identified which can account for many features reported in experiments on other *bcc* metals at low temperatures [4].

2. Literature review

2.1. Concept of a dislocation

In this section, the concept of dislocations is briefly presented to familiarize the reader with the terminology used in the rest of this work. For a more detailed description of the theory of dislocations, the reader is referred to references [2, 12].

The concept of a dislocation was developed independently by Orowan, Polanyi and Taylor in 1934 [13–15] to account for the discrepancy between theoretically predicted yield stresses based on perfect crystal lattices and experimentally observed yield stresses.A dislocation is characterized by its Burgers vector $\mathbf{b}$ equal to one of the smallest repeat vectors of the crystal lattice and its line direction $\boldsymbol{\zeta}$. Three fundamental dislocation types have been identified which differ in their geometry. These are edge, screw and mixed dislocations and are defined depending on whether the line direction of the dislocation $\boldsymbol{\zeta}$ is perpendicular, parallel, or at an arbitrary orientation to its Burgers vector $\mathbf{b}$. The glide planes on which the dislocation can move under stress are preferably the densest packed planes which are called the elementary slip planes of the underlying crystal lattice.

The center of the dislocation line is called its core. The total energy of a dislocation consists of a core energy contribution and the energy due to the long-range strain field. To describe the dislocation core, the most commonly used analytical model is the Peierls-Nabarro model [2,16] which takes into account the discreteness of the lattice. In this model, the dislocation is defined by means of a disregistry between atoms above and below the slip plane of the dislocation. The width of the dislocation core depends on the interatomic forces and therefore requires input from ab-initio methods. Another approach to study the core structure of a dislocation is by atomistic simulations which will be discussed in detail in section 2.3.

The total force per unit length acting on a dislocation is given by the Peach-Koehler (PK) expression [2, 17]

$$\frac{\mathbf{f}_{PK}}{L} \; = \; (\mathbf{b} \cdot \boldsymbol{\sigma}_{tot}) \times \boldsymbol{\zeta} \tag{2.1}$$

where $\boldsymbol{\sigma}$ is the total stress on the dislocation with Burgers vector $\mathbf{b}$ and line direction $\boldsymbol{\zeta}$. The force expression has two components: a glide component

$$\frac{\mathbf{f}_{gl}}{L} \; = \; \frac{[(\mathbf{b} \cdot \boldsymbol{\sigma}_{tot}) \times \boldsymbol{\zeta}] \cdot [\boldsymbol{\zeta} \times (\mathbf{b} \times \boldsymbol{\zeta})]}{|\mathbf{b} \times \boldsymbol{\zeta}|} \tag{2.2}$$

and a climb component

$$\frac{\mathbf{f}_{cl}}{L} \; = \; \frac{[(\mathbf{b} \cdot \boldsymbol{\sigma}_{tot}) \times \boldsymbol{\zeta}] \cdot (\mathbf{b} \times \boldsymbol{\zeta})}{|\mathbf{b} \times \boldsymbol{\zeta}|} \tag{2.3}$$

Dislocation climb is a process by which the dislocation can move out of its slip plane. Climb is driven by diffusion and occurs only at high temperatures.

It must be emphasized here that only the glide component of the PK force contributes directly to dislocation glide and hence to plastic slip despite the non-planar core-structure of screw dislocations in *bcc* metals. The other stress components only influence the core-structure.

Dislocation lines typically contain steps of atomic sizes which are called either kinks if they can glide conservatively along the dislocation line, or jogs if the step is out of the slip plane and cannot glide conservatively. Jogs can be sources and sinks for vacancies. These steps can therefore alter the dynamics of dislocations by acting as pinning points.

2.2. Mechanical properties of *bcc* metals

2.2.1. Experiments on bulk crystals

The first systematic attempt to quantify mechanical behavior of close-packed metals was derived from tensile experiments in cadmium and condensed into the Schmid law [1, 18]. This law provided the first framework to predict the onset of plastic flow in close-packed metals. It states that the plastic flow in metals occurs when the shear stress on a slip plane in the direction of densest atomic packing (slip direction) reaches a critical value (critical resolved shear stress CRSS) which was termed "Schubspannungsgesetz" [18](shear-stress law). There are two major implications of this law. Firstly, there exists a well-defined CRSS to initiate plastic flow in metals, that is independent of the orientation of applied loading and the sense of shearing on a crystallographic plane. Secondly, it is not affected by components of the stress tensor other than the resolved shear stress [3]. Accordingly, plastic flow is expected to initiate on the plane having the highest resolved shear stress. However, already the early studies of plastic flow in α-Fe [19] and $\beta-$brass [20] indicated the complex nature of yielding in *bcc* metals which cannot be described by the Schmid law. These experiments revealed two important characteristics of slip common to *bcc* metals: 1) The slip geometry and the yield stress depended on the orientation of the applied loading 2) No well-defined close-packed plane of slip could be identified.

Later investigations of the yield stress dependence on temperature of several *bcc* metals also revealed that the deformation behavior and slip geometry of *bcc* metals is temperature and orientation dependent [21, 22]. The observed temperature dependence of yield and flow-stress of *bcc* metals was at first attributed to the thermally activated unpinning of dislocations at solute atoms [4]. Availability of new sample growing techniques like the electron beam floating zone method and subsequent refinement like the ultra-high vacuum annealing enabled the preparation of samples free from interstitial impurities [4]. Systematic experiments on several pure *bcc* metals unambiguously demonstrated that the strong temperature behavior of flow stress is indeed an intrinsic property of all *bcc* metals. Furthermore, from extensive investigations on $\alpha-$Fe [23–27], Nb [28–34] , Fe-Si

alloys [35–37], refractory metals constituting the group VB like V [29, 38] and Ta [39–43] and group VIB like Mo [22, 44–48], W [42, 46, 49–53] the following fundamental deformation characteristics could be attributed to all *bcc* metals:

1. The yield and flow-stress for a given orientation depends on the sense of loading referred to as the tension-compression asymmetry which was already observed on $\beta-$brass by Taylor et al. [20]. This constitutes a striking violation of the Schmid law

2. Twinning-antitwinning asymmetry is also intrinsic to *bcc* metals, which means that the CRSS depends on the sense of shear. Its existence was confirmed by pure shear experiments on Mo by Guiu [54]

3. Yield and flow-stress is temperature dependent and this property is intrinsic to all *bcc* metals

4. Orientation dependence of flow stress is a characteristic property of *bcc* metals

5. Slip geometry is varied and complex and is temperature dependent. Slip direction is always a $\langle 111 \rangle$ direction

6. Work-hardening rate is orientation and temperature dependent. While at high-temperatures most *bcc* metals exhibit the three stage hardening similar to that in *fcc* metals (see for example [28]), low temperature stress-strain curves are highly orientation dependent. Specimens oriented for single slip typically show quasi-parabolic stress-strain curves at low temperatures (see [4, 55] for review)

Since the deformation behavior of *bcc* metals deviates from the Schmid law, these features are together termed non-Schmid effects [4, 56]. The theoretical and experimental aspects of plastic deformation in several *bcc* metals have been well-reviewed in [4, 57].

Due to the complex slip behavior, mechanical tests were complemented with *in situ* and *ex situ* transmission electron microscopy (TEM) studies to gain insight into the dynamics of dislocations and dislocation arrangements. The presence of long-screw dislocations in the post-deformation TEM images at low temperatures led to the notion that the screw dislocations may be rate-controlling in *bcc* metals [24, 44, 45]. This view was

further confirmed by *in situ* experiments [58,59] which showed the screw dislocations moving rigidly at low temperatures. Based on these observations, it is now understood that : 1) Screw dislocation motion occurs via kink-pair mechanism and 2) The kink-pair nucleation time is larger than their propagation along a screw dislocation. These two aspects are also utilized for modeling the screw dislocation motion in the present work. Despite numerous investigations to understand the mechanisms controlling controlling the plastic deformation in *bcc* metals, a consistent overall understanding of mechanical behavior remained elusive.

Temperature and strain rate dependence of flow stress
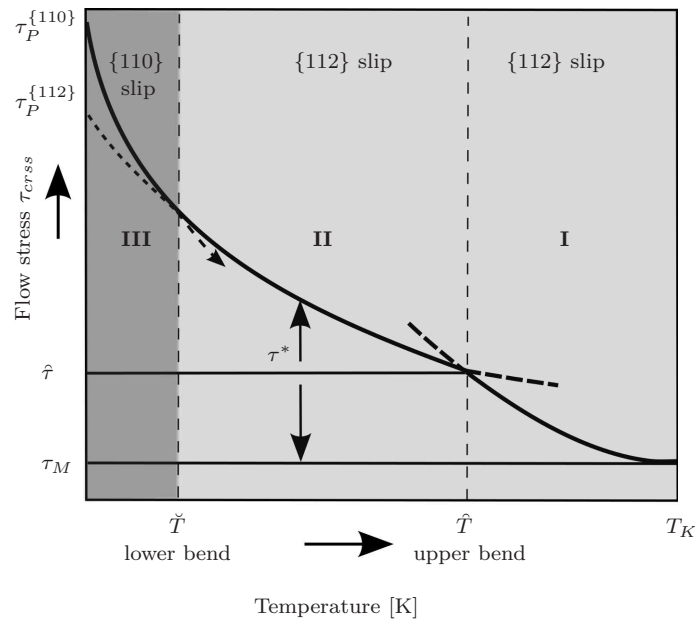
Figure 2.1.: Schematic representation of typical flow stress-temperature relationship of *bcc* metals adapted from reference [60].

The dependence of flow-stress on temperature and strain rate investigated for several *bcc* metals like W [55, 61, 62], α-Fe [63–65], Mo [66], Nb [67], and Ta [68] reveals a generic form shown schematically in Fig. 2.1. Below the so-called knee-temperature T_K (also referred to as athermal temperature [1]), there exist three distinct regimes I, II and III [71, 72] characterized by different slopes of the flow-stress vs temperature curve.

Seeger [8, 71] proposed the quantitative tools to interpret the flow-stress data of *bcc* metals in terms of the kink-pair nucleation theory [73, 74]. It is assumed that a reliable experimental determination of temperature dependent flow stress can be justified by the following equation

$$\tau_{crss} \; = \; \tau_a \; + \; \tau^*(\dot{\gamma}, T) \qquad (2.4)$$

The equation expresses that below the transition temperature T_K, the effective CRSS τ_{crss} is assumed to consist of a thermal component τ^* [75] and a smaller athermal component τ_a. The athermal component is very small (about 15 MPa for W [62]) and includes contributions from the long-range internal strain field whose temperature dependence results from the dependence of the elastic moduli on temperature [8, 75]. It is therefore assumed that the applied strain rate $\dot{\gamma}$ is maintained by screw dislocations only.

For W, the experimental measurements of the temperature dependence of flow stress by Brunner [61, 62] upto $T_K = 800$ K have shown that the transition from regimes I and II and regimes II and III occur at 600 K and 220 K respectively. These transition temperatures are also called upper and lower bend temperatures [8] respectively. Similar regimes and transition temperatures also exist in other *bcc* metals. It must be noted that deformation below 100 K in W and other *bcc* metals [61, 76] is limited by cleavage fracture and twinning. Therefore, at such temperatures different size of specimens were used to determine the flow-stress. The experimental value of the Peierls stress is obtained by extrapolating the stress-temperature dependence to 0 K.

---

[1]The notation T_k for the athermal temperature used here is due to Sestak and Seeger [69]. This notation is used to interpret experimental results on W by Brunner [55] and is also followed in the present work. However, in the modern literature [70], the athermal temperature is also denoted by T_a.

To account for the different regimes, two different kink-pair models are assumed to be active [71] in the respective regimes. Regime I of small applied stresses (and high temperatures), is attributed to the screw dislocation being connected to the neighboring Peierls valley by a pair of elastically-interacting kinks [74]. In other two regimes of moderate to high-stresses, a line tension approximation has to be used to describe the kinks on a screw dislocation. This is because owing to large stresses the kink-pairs are so close that they cannot be accurately described by the linear-elastic theory. These two models will be discussed in detail in section 3.2.3.

Fracture experiments on W single crystals [77–79] also show that the fracture toughness and the brittle to ductile transition are both directly correlated with the temperature and strain rate dependent changes of dislocation mobility [80]. This further emphasizes the necessity for an accurate description of dislocation mobilities in a computational model in order to properly link the microscopic mechanisms with macroscopic behavior.

Elementary slip planes in *bcc* metals

Another fundamental aspect of deformation in *bcc* metals, which has been a subject of controversy over the years, concerns the elementary planes of slip on which dislocation motion occurs. In *fcc* metals the elementary plane of slip is well-known to occur on the {111} planes. In *bcc* metals however, the elementary slip planes are less clear. A feature common to all *bcc* metals in experiments is the occurrence of well-defined crystallographic slip on {110} planes at low temperatures and on the maximum resolved shear stress plane at higher temperatures [4]. At medium and high-temperatures {112} (or {123}) slip has also been reported in *bcc* metals (see for example [49, 55, 81] for W or [45, 46, 66] for Mo).

Taylor and Elam [19] first introduced the notion of pencil glide as a mechanism of slip in *bcc* crystals according to which the direction of slip is the ⟨111⟩ direction but the slip plane coincides with the maximum resolved shear stress plane. While it is now accepted that slip occurs along the ⟨111⟩ direction, the microscopic slip planes on which slip occurs are still unclear. The most common interpretations are:

1. The elementary slip planes are {110} in the entire temperature range and the MRSSP slip is composed of slip events on {110} planes [82, 83].

2. The elementary slip planes are {110}, {112} and {123} [46, 84, 85].

3. The elementary slip plane changes from {110} at low temperatures to {112} at higher temperatures [8, 86]. The change in slip plane of the screw dislocations at higher temperatures is attributed to a core transformation of a/2⟨111⟩ screw dislocations which is hypothesized to make it easier for the screw dislocation to glide by elementary steps on the {112} planes [87].

The interpretations 1 and 2 above are based on the macroscopic slip traces. The interpretation 3 is based on the height of kinks (i.e. the distance between the Peierls valleys connected by a kink), which is inferred from experiments from the flow-stress vs temperature data. Specifically from the measurements on W by Brunner [62], the heights of kinks in regime I and II correlate well with the kink-pair nucleation on {112} planes and in the regime III on the {110} planes. However, this interpretation is not unique for all *bcc* metals since for $\alpha-$Fe, Brunner and Diehl [63, 88] conclude that dislocations glide on {110} planes in regime II.

More recently Caillard [89, 90] concluded from in-situ experiments on thin foils of $\alpha-$Fe that the elementary slip planes are always of the {110} type. Luft et al. [91] performed sub-surface microstructure analysis to correlate the slip planes with the underlying microstructure and obtain information on the elementary slip planes. However, they concluded that little reliable information on the slip activity in the bulk can be obtained from the analysis of surface slip traces alone due to the insufficient resolution of the optical methods. In summary, there is no reliable method to directly determine the slip traces which has led to the ambiguity of elementary slip planes in *bcc* metals.

Anomalous slip

The understanding of the mechanical properties of several *bcc* metals is further complicated by the occurrence of so called anomalous slip. The

term "anomalous" refers to the occurrence of slip on a plane of very low resolved shear stress. Classically, it refers to the occurrence of significant slip on the low-stressed $(0\bar{1}1)$ plane for any orientation of loading inside the $[001] - [011] - [\bar{1}11]$ stereographic triangle. Anomalous slip was first observed in Nb by Duesbery et al. [30] as the dominant slip plane at low temperatures. Other *bcc* metals like W [46], V [92, 93] and Ta [94–97] also showed anomalous slip, though in these metals it is thought to occur in the early stages of straining. The role of other slip systems when accompanied by anomalous slip is highly orientation dependent. No anomalous slip to date has been observed in $\alpha-$Fe [76].

The key features of anomalous slip based on slip traces and TEM observations can be summarized as follows:

1. Anomalous slip in *bcc* metals is associated with sharp and straight slip lines and occurs only at low temperatures. It occurs mostly in high-purity metals [4]. The slip traces are coarse crystallographic occurring on well-defined {110} planes.

2. A network of dislocations joined by $\langle 100 \rangle$ junctions has been found on the anomalous slip plane and the conservative motion of the network has been attributed to be responsible for anomalous slip [98].

3. The anomalous slip planes are the same in both tension and compression and the contribution of anomalous slip plane to total deformation is orientation dependent.

4. The Schmid factor of the anomalous slip system is typically fourth or fifth highest. Recent compression experiments in Mo [99] show slip on other low-Schmid factor planes as well.

Surface orientation is also known to significantly influence the slip morphology in *bcc* metals. Vesely [100, 101] conducted tensile experiments on thin foils of Mo single crystals at room temperature for different specimen geometries subjected to the same loading direction. The surface orientation influenced the activity of slip systems and led to unexpected plastic flow on several low-stressed slip systems. However, a mechanistic explanation of this behavior is still elusive.

In the present work, the phenomenon of anomalous slip is investigated in greater detail on micrometer sized pillars and compared directly with experiments on pillars of the same geometry. A new mechanism for anomalous slip consistent with the features of anomalous slip listed above is presented and is discussed within the context of dislocation-dislocation interaction in micropillars in chapter 4.

2.2.2. Small-scale metallic structures

The mechanical properties described in the previous sections have been established on bulk *bcc* single crystals in which the microstructural length scales (typically of the order of μ m) are small compared with the specimen size (order of mm and higher). In bulk-specimens, the mechanical properties are known to be independent of the sample size. However, when the specimen sizes are in the range of few tens of microns or lower, the flow-stress depends on the smallest critical dimension [102] and this phenomena is called the size effect. A size effect has been observed in several single crystalline *fcc* [103, 104] and *bcc* metals [105, 106]. The flow stress σ_y depends on the specimen size d and this relation can be described by the power law $\sigma_y \propto d^{-n}$. The value of the exponent n varies between 0.6 for Ni [103] to 0.97 [107] for Au. Bcc metals like W show an orientation dependent but much weaker size-dependence with $n \approx 0.16$ for single-slip orientation at room temperature [108]. The dominant mechanisms responsible for size-effect in *fcc* single crystals are attributed to either collective effects of dislocation multiplication and resulting forest hardening from junction formation in larger crystals or single source controlled plasticity in smaller pillars [104]. However, the role of these mechanisms in the size-effect in *bcc* metals is unknown. Interestingly, despite differences in the magnitude of exponent n, both *fcc* and *bcc* metals exhibit similar strain-burst characteristics i.e. nearly elastic loading regions followed by frequent dislocation avalanches. One possible implication of the same strain-burst characteristic is that similar mechanisms may control the size-dependent behavior in these metals [109]. Furthermore, Bei et al. [110] found that in micro samples of directionally solidified Mo, the flow-stress depends on the initial-dislocation density.

Schneider et al. [106] have shown that at a given test temperature T_{test} the

scaling exponent n in bcc metals varies inversely with the athermal temperature T_k. Their results show two different regimes of size-dependence: for metals with high T_{test}/T_k, an fcc like size dependence is observed and for low T_{test}/T_k much weaker dependence has been observed. In other words, since amount of thermal activation depends on T_{test}, the screw dislocation mobility strongly influences the scaling exponent n in bcc metals. Similar results have also been obtained by Han et al. [111].

Using DDD simulations, Greer et al. [112] observe that in fcc pillars, a single dislocation glides and exits the volume without multiplying. Comparatively in a bcc pillar, a single screw dislocation can easily multiply and further generate new screw dislocations due to its ease of cross-slip. The screw dislocations reside longer in the volume owing to their large CRSS and therefore are expected to contribute more to strain-hardening. Based on these observations the authors propose that dislocation-dislocation interactions play a much more important role in bcc metals and this fundamental difference in dislocation behavior may possibly be responsible for the different scaling exponents in fcc metals and bcc metals. However, Schneider et al. [113] showed that pre-straining had little effect on the size-effect coefficient of Mo single crystals. While for fcc metals several large-scale fully 3D DDD simulations have been performed to investigate the mechanisms of size effect in fcc metals [103, 104], in bcc metals such simulations are difficult owing to the lack of good models that can account for the plastic anisotropy of bcc metals in a reliable manner.

2.3. Atomistic investigations of dislocation core properties at 0 K

2.3.1. Properties of a/2$\langle 111 \rangle$ screw dislocation core

Atomistic simulations have been performed since the sixties to investigate the properties of dislocation cores in bcc metals at 0 K. Simple pair potentials [114, 115], which display the stability of a bcc structure, have been used to describe the interactions between atoms. These investigations have

confirmed the non-planar spreading of the dislocation core of screw dislocations in agreement with the Neumann principle [116] which states that the symmetry of any physical property of a crystal must also include the symmetry of the crystal lattice. First proposed by Hirsch [7], this also provided a plausible explanation for the large lattice resistance (Peierls stresses) and lower mobility of screw dislocations as being the reason for the observation of the long screw dislocations in experiments on *bcc* metals [4]. The other aspects of non-Schmid behavior like the orientation dependent CRSS and twinning-antitwinning asymmetry could also be qualitatively interpreted in terms of single screw dislocation behavior [117,118] at 0 K. However, all the early calculations have shown two energetically equivalent configurations of the screw dislocation core which are related to each other by a {110} diad symmetry and have hence been termed as degenerate.

The validity of a degenerate core structure has always been questioned as the pair potentials could not accurately describe the mixed metallic and covalent type of bonding characteristic of transition metals [119]. Using more sophisticated yet empirical central-force many-body potentials like the Finnis-Sinclair (FS), or the embedded atom method (EAM) also revealed a degenerate core [56, 120]. The empirical potentials being computationally efficient are used for molecular dynamics simulations (see for example [121]). However, since the dynamics of screw dislocation is directly related to the core transformation due to atomic rearrangement induced by the applied loading, the clarification of the true nature of screw dislocation core is therefore significant.

Ab-initio density functional theory (DFT) based studies on Mo and Ta [122–124] and other transition metals [125] predict a non-degenerate core structure which symmetrically spreads on all the {110} planes of the zone of the ⟨111⟩ direction. Ab-initio methods being more credible, the equilibrium core structure of a screw dislocation is now accepted to be non-degenerate. However, owing to their computational intensity, the ab-initio methods are limited by the size of the simulation cell and periodic boundary conditions and cannot be used to study the finite temperature behavior of dislocations.

Semi-empirical schemes like the Bond Order Potentials (BOP) which provide a tradeoff between the accuracy of ab-initio based methods and the

computational efficiency of empirical methods are being used to study the properties of dislocation cores of transition metals [126, 127]. They can successfully describe the directional nature of covalent bonds in *bcc* transition metals. They predict a non-degenerate core in agreement with DFT calculations. The BOP developed in [126] has been used to obtain the atomistic data used in the present work.

Ito et al. [120] investigated in detail the stress components which affect the glide of screw dislocation using FS potential for Mo and Ta. They found that even though the stress state on a dislocation may be quite complex, the only components of stress tensor affecting the CRSS of screw dislocation are 1) the shear stress parallel to the slip direction and 2) the shear stress perpendicular to the slip direction. Other components of the stress tensor do not significantly influence the CRSS of screw dislocation. This has also been confirmed by the recent investigations of Gröger et al. [9, 128] using BOP on W and Mo [126, 127].

Gröger systematically calculated the dependence of the Peierls stress of a $\langle 111 \rangle$ dislocation on the orientation of the maximum resolved shear stress plane (MRSSP) in uniaxial loading and on the magnitude of the shear stress perpendicular to the slip direction. They have found a strong twinning-antitwinning asymmetry in Mo but virtually none in W. Additionally, the most active slip system does not systematically coincide with the most highly stressed $\{110\}\langle 111 \rangle$ glide system but varies with both the orientation of the MRSSP and the magnitude of the shear stress perpendicular to the slip direction. At the discrete atomic level, this is attributed to the presence of small edge components of displacement within the non-planar screw dislocation core which are affected by the applied loading. Based on these results, they have developed an atomistic yield criterion utilizing the non-Schmid framework of Qin and Bassani for Ni_3Al [129, 130]. The yield criterion has been utilized to construct a two-dimensional Peierls potential that changes its shape in response to the non-glide stress components and orientation of the MRSSP [11]. The constructed Peierls potential has been then utilized to develop a thermodynamic model of the dislocation glide at finite temperatures, which is based on the classical works of Seeger [74] and Dorn and Rajnak [73]. It is thus possible to obtain physically justified flow criteria for Mo and W that originate from the level of isolated a/2$\langle 111 \rangle$ screw dislocations. By scaling the atomistically obtained stresses by a factor of roughly 3-4, this mul-

tiscale approach has shown to yield reasonable macroscopic predictions of cavitation instability and the occurrence of strain bursts in *bcc* metals [11, 131]. However, no attempt has been made to directly employ the atomistic simulation results to study general dislocation-dislocation interactions at arbitrary stresses in *bcc* metals.

MD simulations have been employed to directly observe and confirm that the screw dislocations indeed glide by the kink-pair nucleation mechanism [121, 132]. All atomistic simulations (both 0 K and finite temperature) to date suggest that kink-pair nucleation occurs only on the {110} planes and any other slip occurs as a result of composite slip on these elementary planes (see for example [133]). The determination of the elementary slip planes however, is critical for both the DDD and crystal plasticity models which assume a set of slip systems on which the dislocation evolution occurs.

2.3.2. Properties of non-screw dislocations

Atomistic simulations have revealed that the non-screw dislocations have a planar core structure and the Peierls stress of the edge dislocations in *bcc* metals is much smaller than that of the screw dislocations [134, 135]. For example, using the FS potential for W, the Peierls stress for an edge dislocation is 10^{-4} μ [136] which is about two orders of magnitude smaller than that of screw dislocations (about 10^{-2} μ), where μ is the shear modulus.

Using different interatomic potentials, Yamaguchi et al. [137] showed that despite having a planar core structure, a mixed orientation which is at about 71° to the a/2$\langle 111 \rangle$ Burgers vector and referred to as the M111 orientation, also has a high Peierls stress [138]. Kang et al. [139] investigated the dependence of Peierls stress on the orientation of the dislocation line using the FS potential for Ta. They report that in addition to the screw orientation, several other orientations of dislocation line exist which have significantly higher Peierls stress compared to the pure edge orientation.

An unresolved issue in the *bcc* dislocation theory is why the CRSS of screw dislocation obtained from atomistic studies at 0 K using different interatomic potentials is consistently a factor of about $2 - 3$ higher than

that obtained from experimentally determined flow-stress extrapolated to 0 K (see [140] for a review). This points towards an inadequacy in understanding the fundamental deformation mechanisms governing the plastic flow in *bcc* metals. One major hypothesis attributes that the experimentally measured flow-stress reflects the collective motion of dislocations where the mutual interaction of dislocations compensates the remaining stress needed for continued motion of screw dislocations [140]. In this respect, DDD simulations are most suited to verify this hypothesis since the effective yield stresses in these simulations directly reflect the collective motion of dislocations and will also be addressed in this work.

2.4. Screw dislocation mobility at finite temperatures

The atomistic calculations of the properties of the dislocation core are all performed at 0 K on an isolated and infinitely long screw dislocation. At finite temperatures, the mobility of screw dislocations via the kink-pair mechanism [73, 141] is described using the transition state theory. The average forward velocity of a screw dislocation is given by the equation [142]

$$v = \frac{ba_0 L}{l_c^2}\nu_D \ exp(\frac{-\Delta H(\Sigma)}{k_B T}) \qquad (2.5)$$

where ν_D is the Debye frequency, b the magnitude of the Burgers vector, a_0 the height of the kink ($a_0 = a\sqrt{2/3}$) where a the lattice constant, L the length of the screw dislocation, l_c the critical length for the nucleation of a kink pair, k_B the Boltzmann constant, T the absolute temperature and $\Delta H(\Sigma)$ the stress-dependent activation enthalpy. The term L/l_c gives the number of possible nucleation sites for kink-pairs implying that the rate of kink nucleation is dependent on the length L of the screw dislocation. The critical length l_c is a variable quantity and is a function of stress. It can be obtained from the activation volume V ($l_c \approx \frac{V}{a_0 b}$) [73, 143]. The activation volume is a dislocation parameter

which gives information about the barrier experienced during the thermal activation process and is generally defined as

$$V = \frac{-\partial \Delta H(\Sigma)}{\partial \tau} \tag{2.6}$$

The activation enthalpy ΔH links the atomistic and mesoscale models and its description within a DDD model based on atomistic studies is the primary focus of this work.

2.4.1. Activation enthalpy of kink-pair nucleation

The dominating term in the velocity Eq. (2.5) is the stress-dependent activation enthalpy because of its exponential dependence. Hence its determination plays a crucial role in describing the kinetics of screw dislocations. There are several approaches to describe the activation enthalpy:

In the phenomenological approach due to Kocks [144], the activation enthalpy is given by the following form

$$\Delta H(\tau) = \Delta H_c [1 - (\frac{\tau_{eff}}{\tau_0})^p]^q \tag{2.7}$$

In Eq. (2.7), τ_{eff} is the effective shear stress resolved on the slip plane, τ_0 the Peierls stress at 0 K, ΔH_c a scaling enthalpy term and p and q are parameters which are fitted to experiments. The activation enthalpy ΔH is a function of effective global resolved shear stress and does not account for the core effects on screw dislocation mobility like tension-compression asymmetry which from atomistic simulations [5] are known to influence the glide of screw dislocations.

The classic works of Seeger [74] and Dorn and Rajnak [73] provide two different phenomenological models to describe the kink-pair nucleation process and provide a theoretical basis to determine the activation enthalpy. These models will be discussed in detail in chapter 3.

2.5. Overview of DDD methods

The DDD method is a tool to understand the complex link between collective motion of a large number of dislocations and the macroscopic plastic response of crystals. Within the framework of hierarchical modeling, study of ensembles of dislocations can be used to provide a plastic constitutive relationship for input into higher time and length scale models.

The first attempts to model the dynamics of dislocations in 3D have been advanced by Kubin and co-workers [145–147]. The model is based on the concept of following the evolution of dislocations inside a volume subjected to loading. The dislocation lines are represented by a combination of discretized pure screw and edge orientations of predefined elementary lengths. This model is also called as the called edge-screw model. The dislocation lines move in a discretized space, whose points are chosen so that they coincide with the lattice points of the crystal to be simulated. Other methods differing in geometric formulation but based on the same principle of following the evolution of dislocation ensembles have also been developed [148–153]. It must be emphasized that in a mesoscale simulation like DDD, the core structure of dislocation is not explicitly modeled. This is because the most important phenomena occur are governed by long-range strain and stress fields fields of dislocation, at distances far enough from the core and can be well described by linear elastic theory [2, 5, 154].

Current *bcc* modeling approaches in DDD are based on describing the mobility of screw dislocations by parametrizing the activation enthalpy ΔH of kink-pair nucleation in Eq. (2.5) using the phenomenologically based Kocks law [143,155] (Eq. (2.7)). More recently, Chaussidon et al. [156] have partially incorporated non-Schmid behavior via cross-slip rules in DDD simulations based on atomistic information. These rules give rise to an asymmetric glide in tension and compression loadings. Wang et al. [157] utilize atomistic information to incorporate the effects of the non-glide components of the stress-tensor on screw dislocation mobility within the Kocks model framework. In their model, {112} planes are additionally considered as elementary planes of slip.

The most accurate description of the screw dislocation mobility would be to provide the stress-dependence of activation enthalpy through an analytical function that can reflect all the non-Schmid effects on the Peierls

barrier. However, obtaining such a function is indeed formidable, due in part not only to the difficulty in determining the shape of the Peierls barrier but also because of the additional complexity of its dependence on the non-Schmid stress components.

The activation enthalpy can in principle be directly provided from MD simulations as an input to DDD simulations as a function of stress. However, this would necessitate the determination of the critical stress at which an infinite screw dislocation glides at a given temperature [132]. The MD simulations are inherently limited due to their smaller time and length scales and are therefore performed at high strain rates (10^6 to 10^9 s^{-1}) (see for example [121]). Comparatively, the strain rates at which experiments are conducted are much lower (10^{-5} to 1 s^{-1}) [65, 99]. At such high strain rates of MD simulations, other mechanisms like kinetic roughening of screw dislocation, debris formation and self-pinning or even twinning [121] may be dominant deformation mechanisms which may not be active at the low strain rates of experiments.

A straightforward implementation of the atomistic information into DDD is therefore not feasible. Mesoscopic models such as DDD have to handle longer length and time scales, which necessitates a systematic information transfer from the atomistic scale to dislocation properties in the form of a constitutive law for the dislocation mobility, which at the same time, retains the fundamental physics.

As a first step towards understanding collective motion of dislocations, an approach to transfer the results of atomistic studies on isolated a/2$\langle 111 \rangle$ screw dislocation to a mesoscopic DDD model, which takes into account the dislocation core effects on dislocation mobility at the scale of DDD, is presented in chapter 3 of this work. The motion of each screw dislocation in DDD is governed by the local stress state along the dislocation. The details of the modeling approach are presented in the next chapter.

3. Discrete Dislocation Dynamics

In this chapter, the physical principles and the numerical aspects of the DDD tool and the relevant modeling aspects for modeling dislocation dynamics in *bcc* crystals are presented.

3.1. Generalized description of the DDD tool

3.1.1. The physical model

In a DDD model, dislocations are represented as lines embedded in an elastic continuum. Each dislocation is characterized by its line direction and Burgers vector. The elementary planes on which the dislocation glides are defined *a priori* in a typical DDD simulation. The description of plasticity follows naturally from the change in internal elastic energy of the crystal when a dislocation moves under stress. Non-conservative motion of dislocations due to jogs, vacancy formation and climb, is neglected in this model.

Associated with each dislocation are the corresponding stress and strain fields which are described within the framework of linear elasticity. Only isotropic elasticity is considered here. Each dislocation feels the effect due to other dislocations through their long-range elastic strain fields. When two dislocations approach each other, the nature of interaction can be quite complex and depends both on the orientation of both the dislocation line and the glide plane. Additional constitutive laws are needed to capture the result of such interactions and are discussed in section 3.2.5.
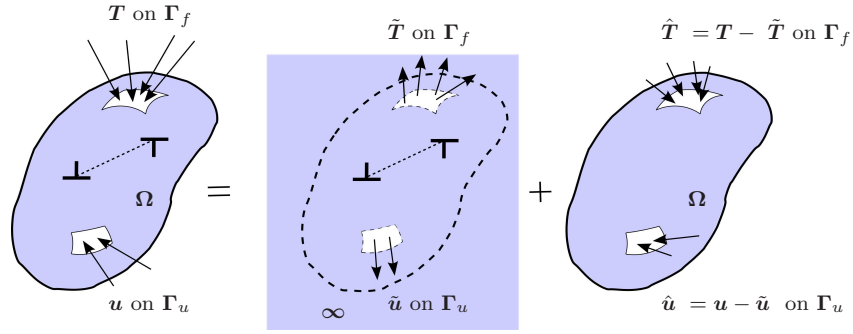
Figure 3.1.: Decomposition of the finite boundary value problem.

3.1.2. Boundary value problem

The boundary value problem is used to represent the class of problems in which certain conditions prescribed on the boundary of the specimen must always be satisfied. Boundary conditions are necessary to describe the complete response of any continuum model. Consider a specimen as shown in Fig. 3.1 with volume $\mathbf{\Omega}$ and surfaces Γ_u and Γ_f on which the following displacement $\boldsymbol{u}$ and traction boundary conditions $\mathbf{t}$ respectively are prescribed

$$\mathbf{u} = \mathbf{U}_0 \qquad \text{on } \Gamma_u \qquad (3.1)$$
$$\mathbf{t} = \mathbf{t}_0 \qquad \text{on } \Gamma_f \qquad (3.2)$$

To solve such a problem, the approach developed by van der Giessen et al. [158] is used. It is based on the principle of superposition of the field variables (strain, displacements etc.) characterizing the response of the specimen. The desired fields (displacement, strain etc.) associated with the boundary value problem are decomposed into two sub-problems: (a) An infinite-space field associated with the analytical equations describing the stress and strain fields of the dislocations and (b) an elastic problem associated with a linear elastic continuum representing the volume Ω without dislocations.

The infinite-space field associated with a dislocation are denoted by ($\tilde{}$) and is readily obtained from direct analytical expressions [2, 159–161]. Assuming N_{disloc} dislocations are present in the current state, the total fields (displacement, strain and stress) due to all dislocations can be obtained by superposition

$$\tilde{\boldsymbol{u}} \; = \; \sum_i \tilde{\boldsymbol{u}}_i \quad \tilde{\boldsymbol{\varepsilon}} \; = \; \sum_i \tilde{\boldsymbol{\varepsilon}}_i \quad \tilde{\boldsymbol{\sigma}} \; = \; \sum_i \tilde{\boldsymbol{\sigma}}_i \quad (i = 1, 2, 3 \ldots N_{disloc}) \quad (3.3)$$

The traction vector on any surface with normal $\mathbf{n}$ due to the stress field $\tilde{\boldsymbol{\sigma}}$ is given by

$$\tilde{\mathbf{t}} \; = \; \tilde{\boldsymbol{\sigma}} \cdot \mathbf{n} \tag{3.4}$$

The resulting fields associated with the dislocation are generally inconsistent with the applied boundary conditions on the corresponding surfaces. Hence correction fields denoted by ($\hat{}$) on the modified elastic continuum are required which are coupled to the ($\tilde{}$) fields via the boundary conditions.

$$\hat{\mathbf{u}} \; = \; \mathbf{U}_0 - \tilde{\boldsymbol{u}} \qquad \text{on } \Gamma_u \tag{3.5}$$

$$\hat{\mathbf{t}} \; = \; \mathbf{t}_0 - \tilde{\boldsymbol{t}} \qquad \text{on } \Gamma_f \tag{3.6}$$

This equation merely states that the solution to the finite boundary value problem 3.1 and 3.2 is equivalent to solving a modified linear elastic problem on a finite volume Ω in which the effect of dislocations has been accounted for.

The corresponding balance equations in the volume Ω are

$$\nabla \cdot \hat{\boldsymbol{\sigma}} \; = \; \vec{0} \tag{3.7}$$

$$\hat{\boldsymbol{\varepsilon}} \; = \; \nabla \hat{\boldsymbol{u}} \tag{3.8}$$

$$\hat{\boldsymbol{\sigma}} \; = \; \mathcal{L} : \hat{\boldsymbol{\varepsilon}} \tag{3.9}$$

where $\mathcal{L}$ is the stiffness matrix. As written in Eq. (3.9), this approach is valid for small-strains.

The total stress on any dislocation inside the continuum is then given by summation of the stresses due to the modified boundary value problem and the stresses due to dislocation-dislocation interactions via their long-range elastic fields. This can be mathematically represented as

$$\boldsymbol{\sigma}_{tot} \;=\; \sum_{j=1}^{N_{disloc}} \tilde{\boldsymbol{\sigma}}_j + \hat{\boldsymbol{\sigma}} \tag{3.10}$$

The total force acting on a segment of length $\mathbf{dl}$ of the dislocation due to the total stress $\boldsymbol{\sigma}_{tot}$ is given by the Peach-Koehler (PK) expression [2,17]

$$\mathbf{f}_{PK} \;=\; (\boldsymbol{\sigma}_{tot} \cdot \mathbf{b}) \times \mathbf{dl} \tag{3.11}$$

The relevant force component which affects the glide of the dislocation is the one which acts only in the glide plane. Climb of dislocation is not considered.

The aspects described above constitute the general framework of the DDD tool applicable to both *fcc* and *bcc* crystals. For a complete description, the physical representation must be supplemented with appropriate constitutive laws for dislocation motion and are described in the next section.

3.2. Modeling aspects for bcc crystals

In the present work, an existing code for *fcc* metals developed by Weygand et al. [162–164] is advanced to account for the *bcc* crystallography. The large difference in mobilities of the edge/mixed and screw dislocations in *bcc* metals necessitates a different approach than modeling *fcc* crystals, since the specific dislocation properties must be separately accounted for. The properties of isolated $\langle 111 \rangle$ screw dislocations are obtained from the atomistic studies. Since at the mesoscale we are obviously not interested in describing every elementary process, an empirical law is required

that can account for the effect of these smaller scale processes and yet retain its coarse-grained nature.

3.2.1. Modeling of non-screw dislocations

In the model presented in this work, the glide of all non-screw segments is assumed to be athermal. Their motion is assumed to be limited by phonon-drag and parametrized by a viscous kinetic law that takes into account the inertial effects similar to that for *fcc* metals [164–166].

$$m_0\frac{\partial v}{\partial t} + Bv = \tau_{glide}b \tag{3.12}$$

$$\tau_{glide} = \mathbf{b} \cdot \boldsymbol{\sigma}_{tot} \cdot \mathbf{n} \tag{3.13}$$

where m_0 is the mass per unit length of dislocation and v is the speed. B is a material specific temperature-dependent drag-coefficient that can be obtained from molecular dynamics (MD) studies. The glide component of the PK-force $\tau_{glide}\ b$ on a dislocation is obtained from the local stress state using Eq. (3.13). The total local stress σ_{tot} is given by Eq. (3.10).

3.2.2. Atomistics of single dislocations and parametrization of loading

The development of a model describing the mobility of $\langle 111 \rangle$ screw dislocations based on atomistic data is the primary objective of this work. This physically based model describing the mobility of a/2$\langle 111 \rangle$ screw dislocations suitable for use within a DDD framework is presented in this section. The parameters of the mobility law are based on the atomistic results of Gröger et al. [9–11]. Within the DDD framework, the local stresses acting on the screw dislocation are known and therefore a local mobility law can be formulated. To connect both the atomistic and DDD framework, the parametrization used for the atomistic results is presented in section 3.2.2. The 0 K atomistic studies reveal that the core

structure of screw dislocation, due to its non-planar nature, can be affected by non-glide components of the stress tensor. Since the dislocation core structure is not explicitly modeled at the DDD scale, the asymmetry induced in the core structure and its effect on dislocation mobility due to applied loading must be accounted for in the simulations by appropriate parametrization.

Here we introduce some basic definitions used throughout this work in a similar manner as in the literature [4,9]. These definitions are with respect to a loading axis within the $[001] - [011] - [\bar{1}11]$ stereographic triangle for a $\langle 111 \rangle$ screw dislocation as shown in Fig. 3.2. For macroscopic uni-axial loading, all possible loading axes in a *bcc* crystal can be symmetrically mapped into the stereographic triangle.
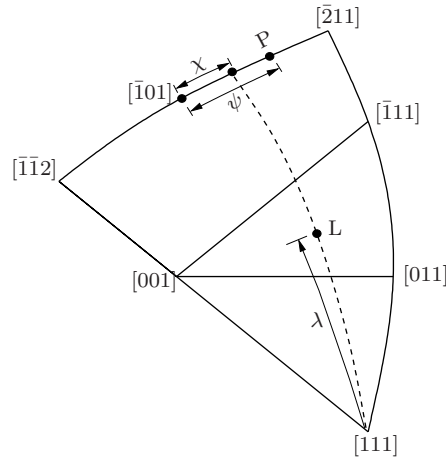
Figure 3.2.: Loading axis in the $[001] - [011] - [\bar{1}11]$ stereographic triangle. The point L represents the orientation of the loading axis, P the direction normal to the slip plane and N is the direction normal to the MRSSP.

1. *MRSSP*: The maximum resolved shear stress plane as shown in Fig. 3.3, whose orientation is defined as the angle χ it makes with the $(\bar{1}01)$ plane. For reasons of crystal symmetry, it is sufficient to consider $-30° \leq \chi \leq 30°$.

2. The *twinning* ($\chi < 0$) and *antitwinning* ($\chi > 0$) sense of shearing
on the nearest {112} plane Fig. 3.3.

3. *CRSS*: The critical resolved shear stress acting on the *MRSSP* which
indicates the shear (glide) stress required to move the dislocation in
any of the {110} planes.

4. The angle ψ between the $(\bar{1}01)$ plane and the observed (macroscopic)
plane of effective slip.
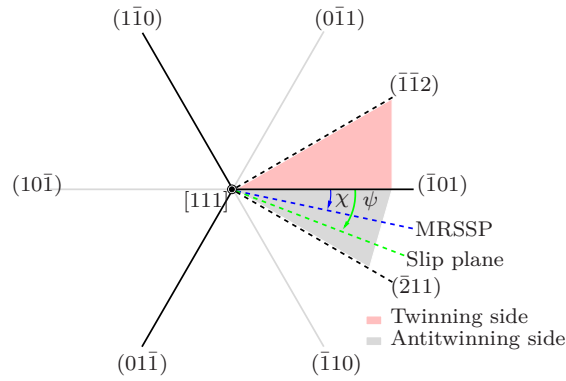
Figure 3.3.: Orientation of planes in [111] zone.

The three {110} planes that contain a given $\langle 111 \rangle$ Burgers vector are called
the zonal planes. The most relevant components of the stress tensor that
affects the magnitude of the *CRSS* to move a screw dislocation on either
of the planes in the zone of a given Burgers vector is given by [9, 10]

$$\mathbf{\Sigma}^{\chi} = \begin{bmatrix} -\sigma & 0 & 0 \\ 0 & \sigma & \tau \\ 0 & \tau & 0 \end{bmatrix} \tag{3.14}$$

This tensor is obtained by transforming the stress tensor into a right-
handed system defined in the MRSSP with the z-axis parallel to the Burg-
ers vector, the y-axis normal to the MRSSP and the x-axis in the MRSSP.

σ and τ denote the shear stress perpendicular and parallel to the slip direction. The perpendicular component is obtained by rotating this stress tensor counter-clockwise around the z-axis by 45° [10], which is the maximum value of the normal stress on the MRSSP. Gröger [10] also found that the CRSS-τ relationship is unique for a given χ and is independent of the loading history.

α	$(n^\alpha)[m^\alpha]$	α	$(n^\alpha)[m^\alpha]$
1	$(01\bar{1})\,[111]$	13	$(01\bar{1})\,[\bar{1}1\bar{1}]$
2	$(\bar{1}01)\,[111]$	14	$(\bar{1}01)\,[\bar{1}1\bar{1}]$
3	$(1\bar{1}0)\,[111]$	15	$(1\bar{1}0)\,[\bar{1}1\bar{1}]$
4	$(\bar{1}0\bar{1})\,[\bar{1}11]$	16	$(\bar{1}0\bar{1})\,[11\bar{1}]$
5	$(0\bar{1}1)\,[\bar{1}11]$	17	$(0\bar{1}1)\,[11\bar{1}]$
6	$(110)\,[\bar{1}11]$	18	$(110)\,[11\bar{1}]$
7	$(0\bar{1}\bar{1})\,[\bar{1}\bar{1}1]$	19	$(0\bar{1}\bar{1})\,[11\bar{1}]$
8	$(101)\,[\bar{1}\bar{1}1]$	20	$(101)\,[11\bar{1}]$
9	$(\bar{1}10)\,[\bar{1}\bar{1}1]$	21	$(\bar{1}10)\,[11\bar{1}]$
10	$(10\bar{1})\,[1\bar{1}1]$	22	$(10\bar{1})\,[\bar{1}1\bar{1}]$
11	$(011)\,[1\bar{1}1]$	23	$(011)\,[\bar{1}1\bar{1}]$
12	$(\bar{1}\bar{1}0)\,[1\bar{1}1]$	24	$(\bar{1}\bar{1}0)\,[\bar{1}1\bar{1}]$

Table 3.1.: Table of reference slip systems in *bcc* metals.

The number of crystallographically equivalent $\{110\}\langle111\rangle$ slip systems is 12. Slip on higher index planes is assumed to be composed of steps on the elementary $\{110\}$ planes. In order to differentiate between the twinning and antitwinning sense of shearing, positive and negative slip directions are treated as being distinct. This results in 24 distinct $\{110\}\langle111\rangle$ slip systems as shown in table 3.1.

3.2.3. Screw dislocation mobility

Activation enthalpy: Bottom-up approach

Within the framework of kink-pair nucleation theory, the activation enthalpy is a measure of the remaining energy needed from thermal fluctua-

tions to overcome the Peierls barrier after accounting for the mechanical part of the loading due to glide stress. This is also the critical input required in the screw dislocation mobility Eq. (2.5) in a typical DDD simulation of thermally activated screw dislocation motion. The activation enthalpy ΔH of kink-pair nucleation provides the link between the atomistic and mesoscale modeling. Just like the CRSS, the kink-pair activation enthalpy must also be a function of the non-Schmid components σ, the angle of the MRSSP χ and the glide stress τ. Instead of explicitly accounting for σ, it is preferable to consider the ratio $\eta = \sigma/\tau$. Hence the activation enthalpy can be mathematically represented as $\Delta H(\chi, \eta, \tau)$.

An indirect approach used in this work is to obtain the activation enthalpy by coupling the molecular statics studies and analytical models of kink-pair nucleation. This requires at first, an accurate description of the Peierls barrier reflecting its dependence on generalized loading states. This aspect will be discussed later. Secondly, the mathematical framework of Seeger [71, 74] is used to describe the kink-pair nucleation mechanism.

Two different models corresponding to different temperature regimes are necessary to characterize the experimentally observed stress-temperature relationship up to the athermal temperature (T_k). These models differ in the critical equilibrium shape of the kink-pair on an initial screw dislocation at which the transition of the dislocation to the next Peierls valley occurs. It is assumed that in both these models each successful kink-pair nucleation event allows the transition of the screw dislocation to the nearest neighboring Peierls valley only.

1. Low stress/high temperature regime

In the low stress/high temperature regime, the temperature dependence of CRSS is weak. It is assumed that in this regime, the critical bow-out configuration is represented by a continuous dislocation line connected over two neighboring Peierls valleys via fully developed kink-pairs in equilibrium (see Fig. 3.4(a)). The kink-segments which are idealized to be of edge character, interact with each other via their long-range elastic fields. This model is therefore commonly referred to as the elastic-interaction (EI) model. The elastic interaction between kinks is described by the attractive Eshelby potential [74, 142]. This is written as $\mu a_0^2 b^2 / 8\pi \Delta z$, where μ is the shear modulus in the slip plane, a_0 the height of each kink or, equivalently, the distance between two neighboring Peierls valleys, b the magnitude of
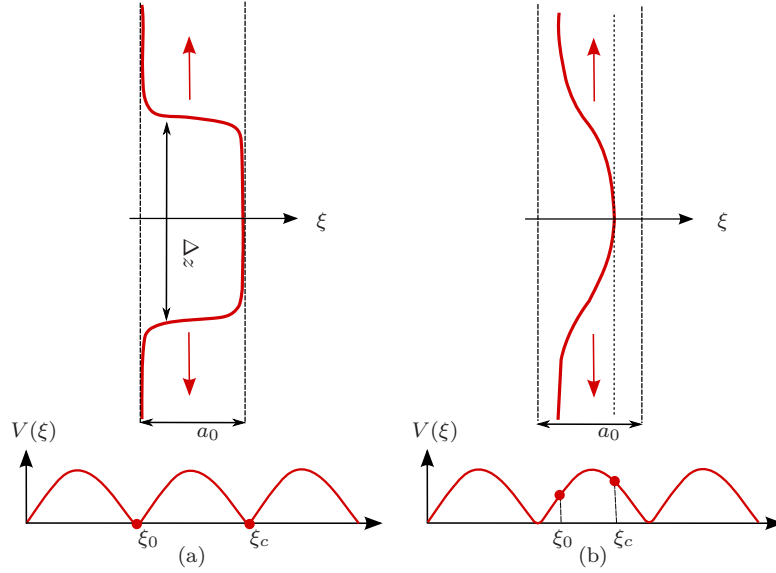
Figure 3.4.: (a) The critical configuration of the kink-pair due to the EI-model consists of fully-developed pairs of interacting kinks connecting the screw dislocation on two Peierls valleys. (b) In the LT-model, the critical configuration is a small bow-out which has not developed into full kinks. Note that in the LT-model, the screw dislocation is already translated a certain distance along the Peierls barrier.

the Burgers vector, and Δz the separation of the two kinks. This attractive interaction is opposed by the applied shear stress τ, which does work $\tau a_0 b \Delta z$ on separating the two kinks. The enthalpy of nucleation of a pair of interacting kinks in the low stress regime, H_{kp}, is then determined by a competition between the attractive elastic interaction and the work done due to the PK-force. The migration of kink along the screw dislocation line results in the glide of the screw dislocation into the neighboring Peierls valley. The activation enthalpy to nucleate the pair of kinks of critical separation Δz at the applied stress τ is then given as

$$H_{kp}(\tau) = 2H_k - (a_0 b)^{3/2} \sqrt{\frac{\mu \tau}{2\pi}} \; , \qquad (3.15)$$

where μ is the shear modulus, and H_k is an energy of an isolated kink. It must be noted that since the bow-out configuration consists of fully developed kinks, the Peierls barrier does not enter the Eq. (3.15). Hence the non-Schmid stresses do not affect the kink-pair nucleation enthalpy in this regime.

2. High stress/low temperature regime
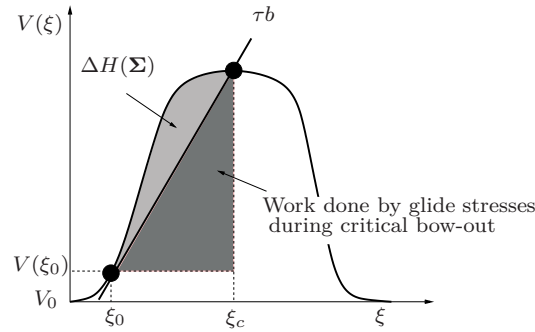
Figure 3.5.: Qualitative representation of stress dependent activation enthalpy.

At finite applied stresses the dislocation is moved away from the bottom of the Peierls valley by the action of the shear stress τ. The path of the dislocation line is curvilinear and the distance of the dislocation along this curve is denoted by ξ. The position along this path at which the force $dV/d\xi$, originating from the Peierls potential equals the total PK-force τb, is denoted by ξ_0 in figures (3.4(b)) and (3.5). Following Dorn and Rajnak [73], the activated state is then represented by a continuous bow-out of a finite segment of the initially straight dislocation from ξ_0 to the position ξ_c which represents the critical state. This activated state corresponds to the maximum of the enthalpy that is obtained by maximizing the difference between the line energy of the dislocation and the work done by the applied stress on overcoming the Peierls barrier. This yields the relation $V(\xi_c) - V(\xi_0) = \tau b(\xi_c - \xi_0)$ which allows to calculate ξ_c if the Peierls barrier $V(\xi)$ is known. Hence, the activation enthalpy takes the form [73]

$$H_b(\tau) = 2 \int_{\xi_0}^{\xi_c} \sqrt{[V(\xi)]^2 - [\tau b(\xi - \xi_0) + V(\xi_0)]^2} \mathrm{d}\xi \qquad (3.16)$$

In the present work, only this LT-model has been used to obtain the activation enthalpies [11] from the atomistic data. The calculation of the activation enthalpy at finite applied stresses from Eq. (3.16) requires explicit knowledge of the Peierls barrier $V(\xi)$ and its intrinsic dependence on τ, σ and χ.

The details of the construction of the Peierls potential for W and the calculation of the stress dependence of the activation enthalpy are provided in references [9–11].

Gröger et al. [11] computed the activation enthalpies for direct transfer to the continuum based on a scaled value of the Peierls stress corresponding to an effective lowering of the experimentally observed CRSS by collective dislocation motion. These scaled activation enthalpies cannot be used in DDD simulations because in the present work the primary assumption is that screw dislocations move at CRSS values obtained from atomistic simulations. Hence, the activation enthalpies were recalculated by Gröger [167] from his raw-atomistic data for tungsten.

Kinetics of Screw dislocations

Fig. 3.6(a) shows schematically, the projection of the $\langle 111 \rangle$ screw dislocation on the (111) plane and the trace of the three $(\bar{1}01)$, $(\bar{1}10)$ and $(0\bar{1}1)$ planes which belong to the zone of this direction. Since the motion of an individual screw dislocation is considered in a 3D discrete dislocation setting, kink-pair nucleation is in principle possible on each of these crystallographic planes corresponding to $\psi = 0°, -60°, +60°$. This clearly goes beyond the established approach [10] which for a given Burgers vector ($|\chi| \leq 30°$), allows for the activation of the primary system only. Here we consider dislocation motion on any of the three possible planes in the zone of the Burgers vector.

The present model is based on the simple idea that the dislocation will have the highest probability of kink-pair nucleation on the plane with
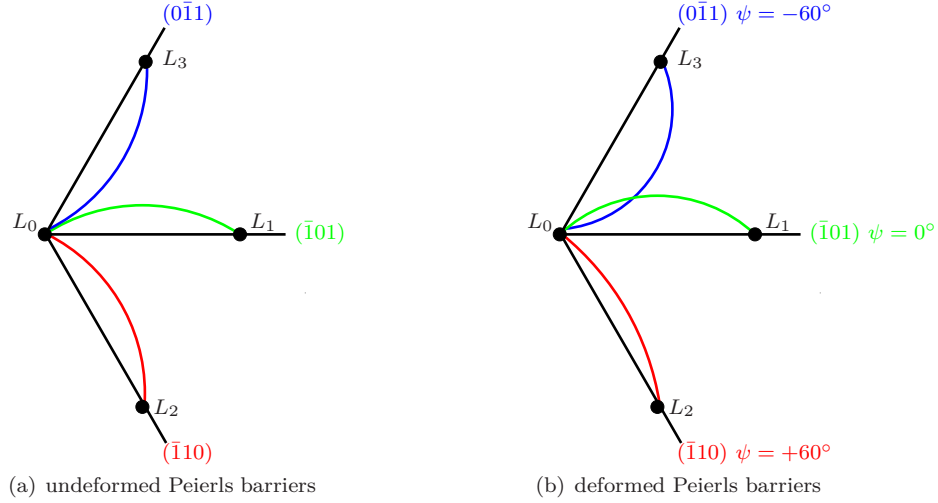
Figure 3.6.: Schematic description of the change in Peierls barriers on {110} zonal planes due to non-zero components of non-Schmid stress σ.

the lowest activation enthalpy for a given loading state. In the absence of applied stress, the Peierls barrier of the dislocation shown schematically in Fig. 3.6(a) between adjacent lattice sites L_0 to L_1, L_2 and L_3 on each of the planes in the zone respectively is the same. For a general loading state however, as can be concluded from the atomistic simulations [9–11], the Peierls barrier on each of the corresponding zonal planes of the screw dislocation is deformed. This changes the activation enthalpy on the corresponding plane. With thermal activation, the Peierls barrier is the determining factor for kink-pair nucleation and Eq. (2.5) gives an average forward magnitude of velocity v_ψ on each of the possible {110} planes

$$v_\psi = \frac{ba_0 L}{l_c^2} \nu_D \ exp(\frac{-\Delta H_\psi}{k_B T}) \qquad (3.17)$$

This results in highest velocity on the plane having the lowest ΔH_ψ. Hence the problem effectively reduces to determine the dependence of the Peierls

potential on χ, η and τ for the corresponding MRSSP and to obtain the kink-pair nucleation enthalpy on each of the three possible planes.

In the DDD model, the activation enthalpy is supplied as a look up table $(\chi, \eta, \tau) \rightarrow \Delta H_\psi$, derived from atomistic calculations for a number of discrete orientations of the MRSSP (χ) and ratios of the two shear stresses (η). A plot for a specific parameter set is shown in figure 3.7. Since the dislocation can move by elementary steps on the three $\{110\}$ planes, three tables are provided that give the activation enthalpies $\Delta H_\psi(\psi = 0°, -60°, +60°)$. To calculate $\Delta H_\psi(\chi, \eta, \tau)$ for a given direction corresponding to any arbitrary stress state, a trilinear interpolation scheme is used.

(a)   (b)
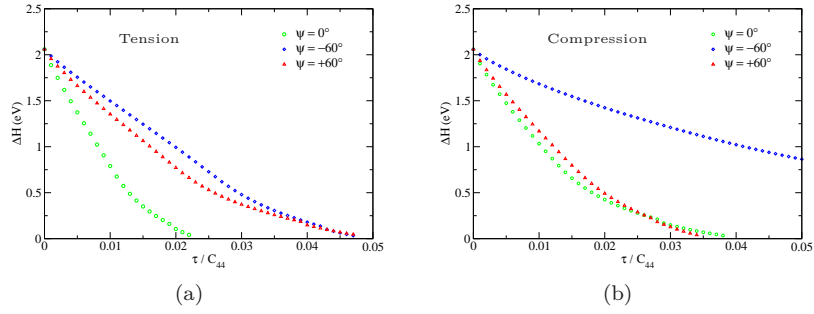
Figure 3.7.: Example of plot of $\Delta H(\chi = 10°, \eta = \pm 0.5)$ vs τ (a) corresponds to $\eta = +0.5$, while (b) is for $\eta = -0.5$.

Once the activation enthalpy ΔH_ψ on each of these three planes is calculated, the total forward velocity of the screw dislocation resulting from motion on elementary slip planes is written as

$$\mathbf{v_{gl}} = \sum v_\psi \mathbf{e}_\psi, \ \text{where } \psi = -60°, 0°, +60° \tag{3.18}$$

Here $\mathbf{e}_\psi$ is the corresponding unit vector in the translation direction and v_ψ is the corresponding magnitude. The angle $\overline{\psi}$ between the effective slip plane and the $(\bar{1}01)$ plane can be computed from the velocity vector using

$$\overline{\psi} = -\sin^{-1} \frac{\mathbf{v_{gl}} . \mathbf{n}}{|\mathbf{v_{gl}}|} \qquad (3.19)$$

where $\mathbf{n}$ is the $(\bar{1}01)$ or $(10\bar{1})$ plane. The effectiveness of this approach will be demonstrated in the examples in section 4.1. Due to the exponential dependence of the velocity on ΔH_ψ, the glide velocity in Eq. (3.18) is dominated by the v_ψ for that {110} plane $\overline{\psi}$ with the lowest ΔH_ψ.

3.2.4. Cross-slip and wavy slip

The geometry of screw dislocations allows it to frequently change its glide plane when favored by local stress. This ability of screw dislocations to cross-slip is an important stress-relaxation mechanism. Devincre et al. [168] have shown that the prediction of cross-slip is essential in understanding the organization of dislocation patterns and dynamic recovery. Post-deformation TEM images of several *bcc* metals show that individual screw dislocation lines lie over several planes connected by kinks (see for example [47]). This indicates a high frequency of cross-slip. Therefore the correct handling of cross-slip in a DDD simulation is crucial for the mechanisms of dislocation multiplication and organization. In the present work, wavy slip (also termed mrss slip) is modeled as a composite of successive cross-slip events on {110} planes.

In the present work, the occurrence of cross-slip and wavy slip is a natural consequence of the relative activation enthalpy ΔH_ψ on the three {110} planes of the zone of a screw dislocation. The activation enthalpy of a screw dislocation on its habit plane **I**, ΔH_{hb} (see Fig. 3.8 is compared with that of the possible cross-slip plane ΔH_{CS} (either **II** or **III**). If ΔH_{hb} is greater than ΔH_{CS}, then it results in a clear cross-slip. Wavy slip occurs when ΔH_{hb} of the habit plane is comparable to the ΔH_{CS} of the cross-slip plane. {112} slip occurs if $\Delta H_{hb} = \Delta H_{CS}$. The numerical aspects of the implementation of cross-slip and wavy-slip in the simulation are discussed in the following sections.
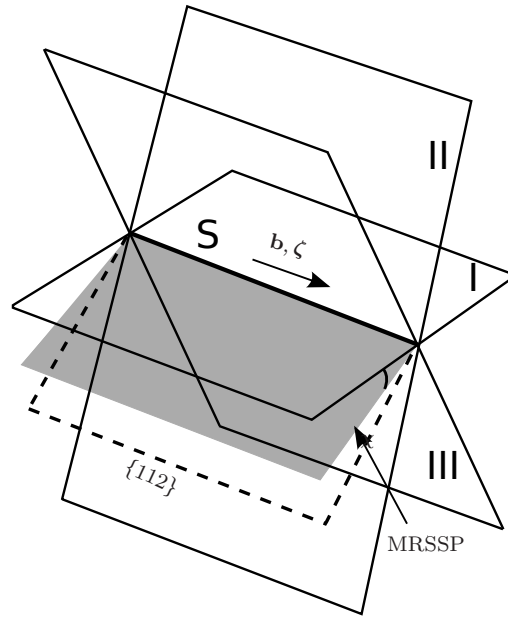
Figure 3.8.: A screw dislocation S with Burgers vector **b** and line direction ζ moving on plane I is shown. The MRSSP plane and the nearest {112} plane are inclined at an angle χ and 30° respectively to the plane I. Planes II and III are possible cross slip planes. Planes I, II and III are of type {110}. The screw dislocation can cross-slip to the plane II or III if the activation enthalpy of the screw dislocation on plane I is greater than any of the other two planes.

3.2.5. Dislocation reactions and junctions in *bcc* metals

In a typical simulation consisting of a large number of dislocations on intersecting glide planes, frequent collisions of dislocations occur. The outcome of these collisions depends on the Burgers vector, the line direction of the segments, the length of dislocations and the total effective stress. Both the long-range and short-range interactions are involved in the intersection process. Atomistic simulations have shown that the energetic contributions of the latter are small and can be neglected [169]. They also provide the intrinsic details of junction formation and destruction [169, 170] and

critical input to their stability. Depending on the nature of the short-range interactions (attractive or repulsive), either a jog or a junction is formed. If the local interaction is repulsive, the dislocations may bypass each other depending on the magnitude of the local driving stress. For the case of attractive interactions, junction formation depends on an energetic and a geometric criterion.
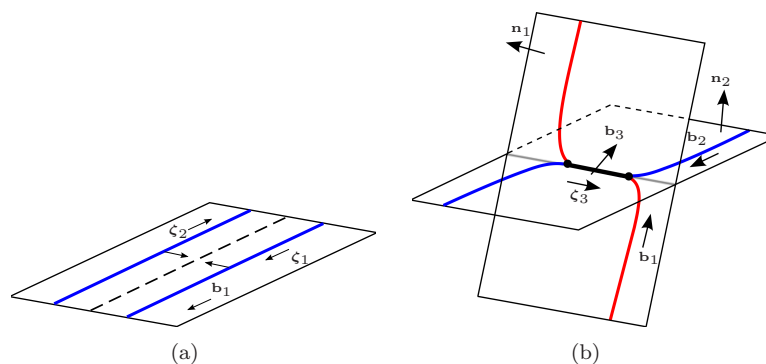
Figure 3.9.: In (a) reaction leading to annihilation of oppositely oriented screw dislocations is shown schematically; (b) shows binary junction formation with Burgers vector $\mathbf{b}_3$ of $\langle 100 \rangle$ type due to reaction of two primary $\langle 111 \rangle$ dislocations $\mathbf{b}_1$ and $\mathbf{b}_2$ gliding on planes with normals $\mathbf{n}_1$ and $\mathbf{n}_2$ respectively. The junction has resultant direction $\boldsymbol{\zeta}_3$ given by Eq. (3.21). The end points of the junctions shown in dark circles may glide along the intersection of the glide planes.

Ideally, rules from atomistic studies are needed to accurately describe such short-range interactions as these interactions cannot be accurately described by the linear elastic theory. In the absence of such atomistic input, we use the same energy based criteria for junction formation (and dissolution) as already described for *fcc* metals in [163]. For two approaching dislocation segments with Burgers vector $\mathbf{b}_1$ and $\mathbf{b}_2$ with line directions $\boldsymbol{\zeta}_1$ and $\boldsymbol{\zeta}_2$ and glide planes $\mathbf{n}_1$ and $\mathbf{n}_2$ respectively, a junction is formed if the line energy of the resulting dislocation with Burgers vector $\mathbf{b}_3 = \mathbf{b}_1 + \mathbf{b}_2$ satisfies the equation

$$E_1(\mathbf{b}_1, \boldsymbol{\zeta}_1) + E_2(\mathbf{b}_2, \boldsymbol{\zeta}_2) > E_3(\mathbf{b}_3, \boldsymbol{\zeta}_3), \tag{3.20}$$

with line direction of the junction

$$\boldsymbol{\zeta}_3 \;=\; \frac{\mathbf{n}_1 \times \mathbf{n}_2}{|\mathbf{n}_1 \times \mathbf{n}_2|} \tag{3.21}$$

and the line energy per unit length E given by the following approximate expression [2]

$$\frac{E(\mathbf{b}, \boldsymbol{\zeta})}{L} = \frac{G}{4\,\pi} \left((\mathbf{b} \,\cdot\, \boldsymbol{\zeta})^2 + \frac{|(\mathbf{b} \times \boldsymbol{\zeta})|^2}{1 - \nu} \right) ln \, \frac{R}{\rho} \tag{3.22}$$

Following [2], the logarithmic term in Eq. (3.22) is neglected. Eq. (3.20) expresses that junction formation is favorable if the product dislocation has lower elastic energy than the reactant dislocations.

Binary junctions are formed when both the reactant dislocations have a/2$\langle 111 \rangle$ Burgers vector. The resulting dislocation can have either null, a $\langle 100 \rangle$ or a/2$\langle 011 \rangle$ Burgers vector. Elastic energy calculations suggest that the a/2$\langle 011 \rangle$ are unstable junctions as they do not lead to a lowering of energy [171]. Depending on the orientation and the glide plane of the $\langle 111 \rangle$ dislocations, the reactions are:

Annihilation: The reaction of two co-planar dislocations with Burgers vector $\mathbf{b}_1$ and $\mathbf{b}_2 = -\mathbf{b}_1$ results in annihilation (see Fig. 3.9(a)).

Collinear reaction: A collinear reaction occurs when both the reactant dislocations are related by $\mathbf{b}_1 = -\mathbf{b}_2$ (see Fig. 3.9(b)), but move on different glide planes. The result is a junction with zero Burgers vector. The end nodes of the collinear reaction are constrained to glide along the direction $\mathbf{n}_1 \times \mathbf{n}_2$ which is the intersection line of the planes $\mathbf{n}_1$ and $\mathbf{n}_2$.

$\langle 100 \rangle$ **junction:** A a $\langle 100 \rangle$ dislocation junction is formed due to the reaction between two unlike a/2[111] dislocations as shown in Fig. 3.9(b). The reaction can be in-plane if both the reactant and product dislocations lie on the same plane or out of plane if either of the dislocations lie on a different plane. Motivated by atomistic studies [172], all a $\langle 100 \rangle$ junctions are assumed to have large Peierls stress and are modeled as immobile. Only the end-points of the junction attached to the reactant $\langle 111 \rangle$ dislocations

are mobile and constrained to move along the intersection of the two glide planes allowing for zipping and un-zipping of junctions.

Multi-junctions: Multi-junctions are formed when a binary junction $\mathbf{b}_3$ in Fig. 3.9(b) reacts with another $\langle 111 \rangle$ dislocation with Burgers vector $\mathbf{b}_4$, where $\mathbf{b}_4$ is not equal to either of $\mathbf{b}_1$ or $\mathbf{b}_2$. The resulting topological network has a Burgers vector of the $\langle 111 \rangle$ type. The end points of such junctions connect four segments. Multi-junctions were first predicted from simulations [173] and their existence was later confirmed in experiments. Several configurations of ternary junctions are possible depending on the elementary glide planes in which the dislocation motion occurs. Multi-junctions are very stable due to their short $a/2\langle 111 \rangle$ Burgers vector and are postulated to contribute significantly to strain hardening [174].

3.3. Numerical modeling

The physical model describing the boundary value problem must be supplemented with appropriate numerical tools to generate a simulation model which can be represented and solved on a computer. These aspects of the numerical model are described in the following sections.

3.3.1. Space discretization and description of dislocations

To numerically represent the finite elastic continuum and the dislocation lines in the simulation, the same methodology described in [162, 163] for *fcc* metals is adopted here. The elastic continuum (see Fig. 3.1) is discretized by twenty-node solid finite elements (with 8-edge nodes and 12 nodes at the mid-point of each edge) are used for this purpose. The accuracy of the stress-resolution depends on the coarseness of the FE-mesh discretization.

For the *bcc* crystallography, the elementary planes on which the dislocations move are assumed to be of $\{110\}$ type. The physical space is discretized into a finite number of glide planes with normal $\mathbf{n}$ separated by

(a)   (b)
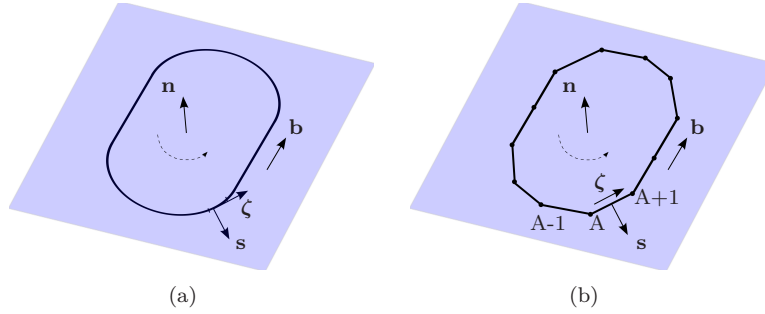
Figure 3.10.: (a) shows a continuous dislocation loop bowing out in its glide plane; (b) shows the equivalent representation of the dislocation in DD with line segments of length l_i interconnected at nodes (circled). The normal and Burgers vector of the loop are **n** and **b** respectively. The instantaneous tangent on an infinitesimal segment is replaced by line direction of the line segment.

an integer multiple of {110} inter-planar distance. An arbitrary dislocation loop on a glide plane is discretized by piecewise straight line segments as shown in the figure 3.10. The line segments are inter-connected at nodes ..., A-1, A, A+1, ... The dislocation line is characterized by its Burgers vector **b** and line direction **t**. For non-intersecting dislocation segments, a node shares two segments only. Such a representation of the dislocation is equivalent to a one-dimensional FEM. The lengths of the line segments are chosen to give an accurate representation of the geometry of the dislocation loop and capture the local curvature. The lengths of the line-segment is limited within a user-defined minimum and maximum range (l_{min} and l_{max}). Further an adaptive scheme is used to adapt the length of segments to local curvature described in [163]. Similar to the approach of Weygand et al. [163], the following types of nodes are distinguished:

1. Material nodes belong to non-intersecting dislocations

2. Sliding nodes belong either to dislocation junctions, surface nodes and additionally those nodes connecting a screw and non-screw segment in case of *bcc* crystallography.

The position and velocity of a node A is denoted by $\mathbf{r}_A$ and velocity $\mathbf{v}_A$ respectively. In a typical DDD simulation, initial dislocation sources are

modeled as randomly distributed Frank-Read (FR) sources with dislocation lines pinned at their ends. This modeling approach due to Kubin et al. [145] is intended to represent the subnet of the Frank net observed in annealed crystals. The sessile arm of the FR source is not modeled.
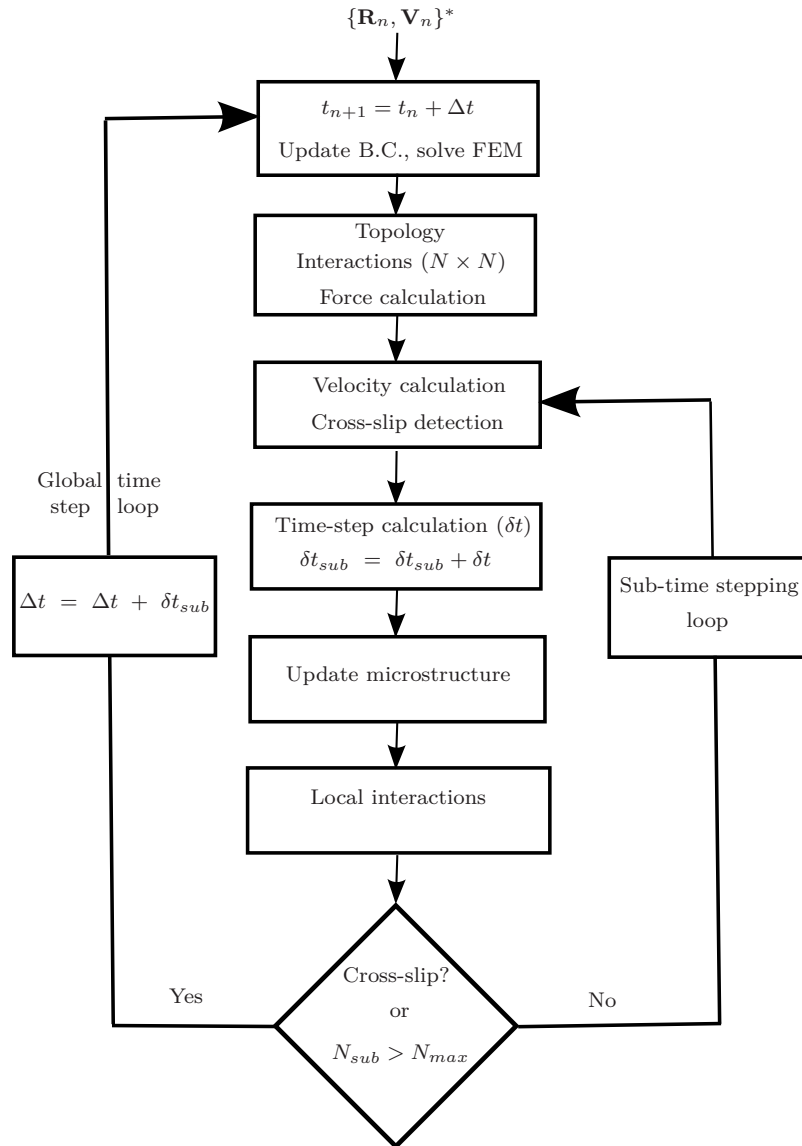
To fully define the problem, the numerical representation of the physical entities of the problem must be supplemented by the specification of the appropriate boundary conditions. An appropriate time discretization scheme to solve the problem numerically for the variables is needed. The general numerical solution of the system is based on an incremental time-stepping scheme.

3.3.2. Solution scheme

Fig. 3.11 shows the flow-chart of the overall scheme of the DDD simulation. The description of the time-evolution of dislocation microstructure is equivalent to determining for each node A the corresponding velocities $\{\mathbf{v}_A\}$ and positions $\{\mathbf{r}_A\}$. The starting point in the simulation is the current known state of the specimen at physical time t at which the positions and the velocities of the dislocations of the entire microstructure are denoted by $\mathbf{R}^t$ and $\mathbf{V}^t$ fields respectively. Due to the different mobility laws needed for screw and non-screw segments, the entire solution scheme is sub-divided to treat the two types of segments separately. This requires an accurate book-keeping of the orientation of the dislocation segments and their classification into screw and non-screw segments which is performed after every update of nodal position. There are several steps involved in obtaining the final solution of the problem which are discussed in subsequent sections.

Boundary conditions and time-stepping scheme

To obtain the time-integrated response of the microstructure for *bcc* crystals, a time-stepping scheme is applied. The incremental update from the current physical time t is performed in a two-stage manner involving global time-stepping and a sub time-stepping scheme. The global time step

$\{\mathbf{R}_n, \mathbf{V}_n\}^*$

$t_{n+1} = t_n + \Delta t$

Update B.C., solve FEM

Topology

Interactions $(N \times N)$

Force calculation

Velocity calculation

Cross-slip detection

Global time
step loop

Time-step calculation (δt)

$\delta t_{sub} = \delta t_{sub} + \delta t$

$\Delta t = \Delta t + \delta t_{sub}$

Sub-time stepping

loop

Update microstructure

Local interactions

Cross-slip?

or

$N_{sub} > N_{max}$

Yes   No

Figure 3.11.: Scheme of the general algorithm used in the DDD simulation.

scheme is the same as that described in Weygand et al. [163] for *fcc* metals. The scheme involves an update of the boundary conditions, the determination of the updated positions of the entire dislocation microstructure and a calculation of interaction of every dislocation segment with all other dislocations in the volume Ω. The time at which the update of boundary condition is performed is obtained by adding to the old physical time the accumulated time-steps in the sub-time stepping scheme discussed below. The linear-elastic modified boundary value problem is now solved to obtain the displacement fields $\hat{\boldsymbol{u}}$ corresponding to the new time step $t + \Delta t$ using the multi-grid method (see for example [175]). From these displacement fields, the corresponding strains and stress fields can be obtained at any point in the volume using the standard finite element method. This is followed by the detection of possible intersections of dislocations and junction formation. The velocity field of all nodes is computed corresponding to the updated boundary conditions.

Within a simulation, the number of segments can increase quickly due to dislocation multiplication which makes the calculation of pairwise-segment interaction and update of boundary condition at every step tedious. A sub-time stepping scheme is used to accelerate the computation. This implies that the accumulated long-range fields of dislocations do not vary strongly in space. This allows for a less frequent update of the boundary conditions and a computation of all dislocation interactions. For *bcc* metals, the existing sub-time stepping scheme is adapted to the large differences in the mobilities of screw and non-screw dislocations and is introduced as follows

1. From the velocity field of non-screw segments, a time-step δt_i is computed based on the rotation and length change of the segment i. A broad distribution of time-steps is obtained for the segments from which an overall minimum δt_{min}^{ns} is computed. For the thermally activated screw segments, a time-step δt_j^s for screw dislocation segments is computed. It is the time required for a screw dislocation with velocity v_i^s to cover a maximum allowed flight distance of 20 b per step. Correspondingly a global minimum time-step δt_{min}^s for screw segments is obtained. Owing to the large difference in mobilities between the non-screw and segments, the time-steps δt_{min}^{ns} and δt_{min}^s are quite large (typically a difference of order of 10^2). The global min-

imum sub-time step is computed as $\delta t = min(\delta t^{ns}_{min}, \delta t^{s}_{min})$ and it is used to update the nodal position and velocities. Additionally, the possible screw dislocation segments which might cross-slip are detected.

2. Corresponding to the time-step δt obtained in step (1), the microstructure is updated and further topological changes like junction formation, re-discretization, detection of segments leaving the volume of the crystal are performed. For dislocation loops which have undergone topological changes, interactions are re-computed for all segments.

3. Steps (1) and (2) are repeated for N_{sub} number of steps subject to several conditions. The value of N_{sub} is an input parameter to the simulation and is chosen such that during the time $N_{sub} \cdot \delta t$, the long-range fields do not significantly affect the boundary conditions. The sub-time stepping scheme is terminated if cross-slip is detected in which case, only the loops not requiring cross-slip are updated for the current time-step only. The algorithm returns to the global time-stepping procedure.

A further modification to the transition between the global and sub-time stepping schemes is necessary. Screw dislocations are prevalent during deformation of a *bcc* crystal and can cross-slip. If cross-slip occurs within a sub-time step, the nodal velocities and updated positions are computed for one sub-time step only. The sub-time step is terminated and the algorithm returns to the global increment step where an update of all the boundary conditions is performed. This is essential because it results in generation of a new loop whose nodal degrees of freedom must be calculated on a newly populated glide plane based on the current global stress-state. Unfortunately, during straining, the screw dislocations cross-slip very frequently which restricts the applicability of the sub-time stepping scheme.

Local stress-tensor and Peach-Koehler force

The local stress field $\boldsymbol{\sigma}$ on a dislocation segment given by the Eq. (3.10), requires the determination of the elastic FEM solution field $\hat{\boldsymbol{\sigma}}$ and the

field $\tilde{\boldsymbol{\sigma}}$ [163]. The long-range stress field denoted by (˜) due to one disloca-
tion at any point on a remote segment of another dislocation varies with
distance r between the segments.

Within the discretized framework of DDD, the local stress field on a re-
mote dislocation segment is computed at its midpoint for a non-screw
segments [145, 149, 163, 176]. A tree data structure is maintained which
contains the information on segment pairs which are within a critical dis-
tance.
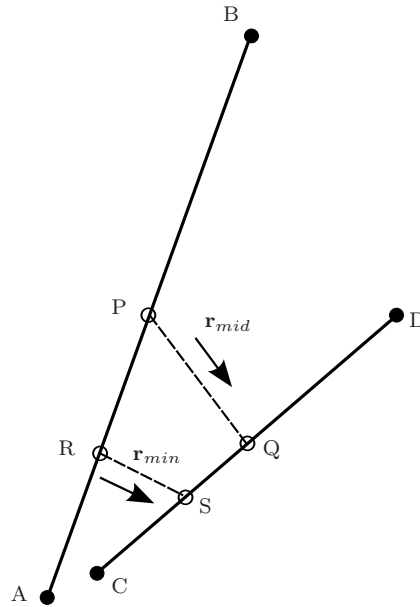
Figure 3.12.: Stress computation for strongly interacting screw dislocations. The
vectors $\mathbf{r}_{mid}$ and $\mathbf{r}_{min}$ are along the midpoints and the nearest approach points of the
two screw segments AB and CD respectively.

For *bcc* crystals, however a modification to the original approach is nec-
essary. For interacting screw dislocations, the interaction stresses due to
other segments may also vary significantly along a segment which affects
the kink-nucleation rate and hence the velocity of screw dislocation. For

segments lying within a radius of $|\mathbf{r}_{min}| = d_{min} < 100\ b$, the stress tensor is therefore evaluated at the point of nearest approach where the resolved shear stress due to interactions is strongest (see Fig. 3.12). From the stress-field, the velocity of each screw segment is calculated using Eq. (3.23). For all other segments, the stress is evaluated at the mid-point of the segments. Once the stress field is determined, the velocities of nodes must be computed. The velocity computation scheme for screw segments is presented in the next section.

Velocity scheme for screw segments

The continuous form of the mobility law for an isolated single screw dislocation is now known. Its numerical implementation into the framework of DDD requires additional considerations. For a screw dislocation of total length L shown in Fig. 3.13, discretized into n_{seg} segments, the averaged forward velocity v_i of each segment i of length l_i is given by

$$v_i = \frac{ba_0 l_i}{l_c^2} \nu_D\ exp(\frac{-\Delta H_i}{k_B T}) \tag{3.23}$$

The parameters χ_i, η_i and ΔH_i are computed for each screw segment from the local stress tensor. These parameters are assumed to be constant for at least N_{ts}^S sub-time steps. In the event of mixed dislocation segments which enter a screw orientation and segments rotating out of the screw orientation for any given loop, the total stress-field on the loop is recalculated and the activation enthalpy parameters for all screw dislocations of that loop are computed. The length l_i of each dislocation segment is so chosen that it is always greater than the critical length l_c required for kink nucleation. Kinks on dislocations are generally of the order of a few lattice spacings which cannot be resolved at the mesoscopic scale of DDD simulations.

It is additionally assumed that the time of migration of a kink t_{mig} along a screw dislocation is short compared to the time between two nucleation events t_{nuc}. This assumption is certainly valid in the low and medium temperature range [86]. Thus every successful kink generation contributes to the forward motion of the dislocation. The velocities of all the individual
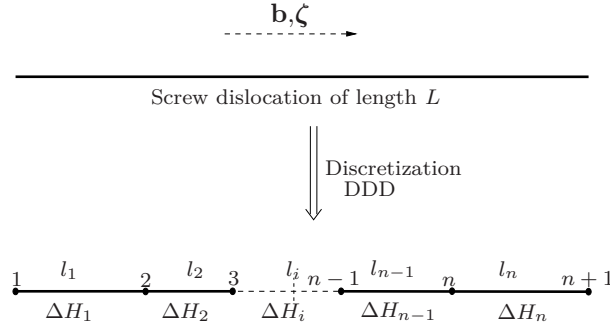
Figure 3.13.: Velocity computation scheme of a screw dislocation in DDD.

segments of a dislocation line are added and the entire dislocation of length L moves forward with the total velocity

$$V_L = \sum_{i=1}^{n} v_i \tag{3.24}$$

A homogeneous stress state along a dislocation of line length L, numerically represented by n_{seg} segments of lengths l_i, results in equal activation energies for all segments $\Delta H_i = \Delta H$

From Eq. (3.24), the average velocity of the screw dislocation results in the expected velocity from Eq. (2.5)

$$V_L = \underbrace{(l_1 + l_2 + \cdots l_n)}_{L} \frac{b a_0}{l_c^2} \nu_D \, exp(\frac{-\Delta H}{k_B T}) \tag{3.25}$$

The direction of motion of the dislocation is given by Eq. (3.18).

Certain additional technical assumptions must be made when modeling dislocations in *bcc* metals. It is assumed through out that a screw dislocation with node on surface always remain straight. Due to this modeling assumption, the mobility of screw dislocations corresponds to those of bulk-crystals. Details are provided in appendix A.1.

In a typical simulation containing a large ensemble of dislocations, significant stress variations across the length of the screw dislocation exist. This may cause a part of the screw dislocation to change its glide plane. To account for these variations the following procedure is adopted.

After the determination of the activation enthalpy per screw segment, the glide plane which corresponds to the lowest-enthalpy plane of its zone is determined (see Fig. 3.14). Each screw segment is then assigned a sector corresponding to its plane of lowest activation enthalpy. Neighboring screw segments which share a common node and glide on the same crystallographic plane are assigned the same sector ID. Once this marking is done, the sectors which do not change glide plane are collectively moved in the same direction. For sectors which might cross-slip, the sector information like the total length, velocity and the plane of slip is stored. The corresponding cross-slip step is performed for those sectors where the accumulated velocity of segments exceeds a critical velocity V_{crit} on the cross-slip plane which is an input parameter. Such an approach is necessary to capture the sudden variations in stresses which occur when an unpinned edge/mixed dislocation traversing the volume of the crystal encounters a screw dislocation. The resulting interaction stress on the screw dislocation can increase rapidly over a short interval of time until the edge/mixed segment bypasses the screw. Additionally, only those segments whose total sector length is greater than 30 a_0 are allowed to cross-slip.

To simulate wavy slip which occurs when two planes of the screw dislocation have nearly the same activation enthalpies, the procedure described in [156] is adopted. From the respective velocities v_i on each of the glide planes of a given Burgers vector, a probability p for slip on the secondary plane is computed from

$$p \;=\; \frac{v_2}{v_1 \;+ v_2 \;+ v_3} \tag{3.26}$$

where v_i are the velocities of screw segments on each of the corresponding planes. The velocities entering the Eq. (3.26) are the cumulative velocities of interconnected segments which belong to the same sector. If p is greater than a random number, then the cross-slip is performed step on the secondary slip plane.
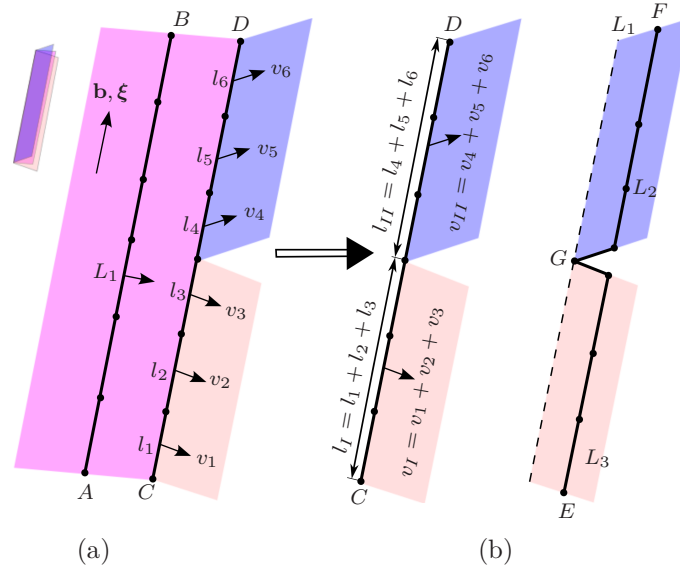
Figure 3.14.: (a) and (b) show the computational procedure for screw dislocations which cross-slip under favorable stress conditions. In (a), an initial screw dislocation L_1 glides from position AB to CD where the local stress state favors segment wise cross-slip. The segment lengths and velocities are also displayed; in (b) beginning with position CD, the sector-wise summing of like segments which are interconnected based on the direction of velocities is shown. After the summation, the two sectors I and II have lengths l_I and l_{II} with cumulative velocities v_I and v_{II} respectively. From CD, the cross-slip of these two sectors on the cross-slip planes results in loop L_2 and L_3 respectively with a common node at G.

From the velocities of the screw segments, a time-step δt is obtained for screw segments. A global minimum of the time-steps due to both the screw and non-screw segments is then used to update the entire microstructure. To avoid arbitrary small-time steps, a minimum time-step is used. In all the simulations performed in this work, this value is taken to be 1×10^{-13} s as the simulation volume always contains some mixed dislocations as well. The position of nodes of screw dislocations are updated using an explicit scheme

$$\mathbf{R}_S^{t+\delta t} \; = \; \mathbf{R}_S^t \; + \; \mathbf{R}_S^t \; \delta t \qquad\qquad (3.27)$$

Junction nodes

Numerically, all the junction nodes connected to a $\langle 111 \rangle$ dislocation segment are treated as sliding nodes to differentiate them from the material nodes. The nodes are constrained to glide along the intersection line of the two intersecting planes in which the $a/2\langle 111 \rangle$ dislocations lie. The velocity of such nodes is given by

$$\mathbf{V}_J \; = \; V_J \; \mathbf{t}_{glide} \qquad\qquad (3.28)$$

with $\mathbf{t}_{glide}$ defined by Eq. (3.21).

3.4. Simulation setup

3.4.1. Pillar geometry and initial configuration

In this work, micrometer sized pillars have been simulated under different loading conditions to understand the deformation mechanisms governing plastic flow. The cross-section of the pillars is either square or rectangular. The square cross-section pillars have an aspect ratio which is defined as the l:h:w where l, h and w stand for the length, height and width respectively as shown in Fig. 3.15. The initial microstructure consists of randomly distributed FR sources with $\langle 111 \rangle$ Burgers vector distributed evenly among the possible $\{110\}$ glide planes. In all the investigated pillars, unless otherwise stated, the length of the pillar is chosen as 0.5 μm. The initial length of the sources is taken to be a constant L=200 nm corresponding roughly to the average distance between dislocations according to the relation $L \approx 1/\sqrt{\rho}$. The initial dislocation density of the pillar was about 2.1×10^{13} m^{-2}. The position and orientation of sources is chosen at random to get a statistical variation. For sources in non-screw orientation, the initial length of the source does not play a role because once the
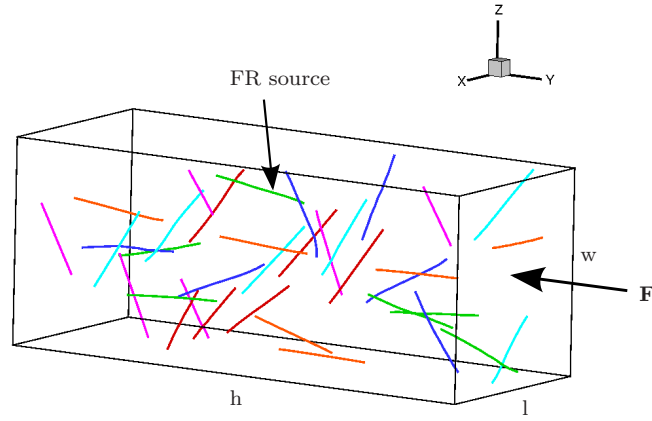
Figure 3.15.: Initial distribution of FR sources inside a pillar with aspect ratio l : w : h. The loading axis is along **F**. Only dislocations with Burgers vectors of type $\langle 111 \rangle$ on corresponding $\{110\}$ planes are present. The color of the dislocation lines are according to their habit planes (see appendix C for the color scheme).

edge and mixed dislocations are driven out of volume, each arm of the FR source acts as a single armed source pinned at one point.

Two different uniaxial loading directions corresponding to the $[\bar{1}\ 5\ 10]$ and $[\bar{1}\ 4\ 9]$ orientations are chosen. The choice of the $[\bar{1}\ 5\ 10]$ loading direction is motivated because of the availability and direct comparison with compression experiments on W micropillars of the Paul-Scherrer group in Switzerland. The aspect ratio of the pillar for the $[\bar{1}\ 5\ 10]$ orientation is $1 : 2.5 : 1$ and the pillar geometry in the simulation is the same as in experiment but the linear dimensions are smaller by a factor 4 owing to large computational cost for larger pillars.

The $[\bar{1}\ 4\ 9]$ orientation is a single-slip orientation which corresponds with that of detailed experimental investigations by Brunner [55]. For this loading direction, simulations are performed in both tension and com-

pression. The aspect ratio of the pillars for this loading orientation is
$1:3:1$. To investigate the role of surface orientation on deformation, sim-
ulations are performed in tension for two different aspect ratios $1:3:2$
and the $1:2:3$.

The Schmid factors for all $\{110\}\langle111\rangle$ slip systems for both the $[\bar{1}\ 5\ 10]$
and $[\bar{1}\ 4\ 9]$ orientations is shown in table 3.2.

Slip system	$[\bar{1}\ 5\ 10]$ (m)	$[\bar{1}\ 4\ 9]$ (m)
$(\bar{1}01)[111]$	0.50	0.50
$(101)[\bar{1}11]$	0.47	0.47
$(0\bar{1}\bar{1})[\bar{1}\bar{1}1]$	0.29	0.32
$(\bar{1}10)[111]$	0.27	0.25
$(0\bar{1}1)[\bar{1}11]$	0.26	0.29
$(0\bar{1}1)[111]$	0.23	0.25
$(011)[1\bar{1}1]$	0.19	0.22
$(110)[\bar{1}11]$	0.21	0.17
$(101)[\bar{1}\bar{1}1]$	0.17	0.20
$(10\bar{1})[1\bar{1}1]$	0.14	0.17
$(\bar{1}10)[\bar{1}\bar{1}1]$	0.12	0.12
$(\bar{1}\bar{1}0)[1\bar{1}1]$	0.05	0.05

Table 3.2.: Table of Schmid factors (m) for the $[\bar{1}\ 5\ 10]$ and $[\bar{1}\ 4\ 9]$ loading directions.

All the simulations involving multi-dislocations are performed at a strain-
rate of 5000 s^{-1}. Other relevant details specific to the simulation is pro-
vided in the corresponding section.

3.4.2. Boundary conditions

All the simulations on pillars are strain rate controlled. Displacements
along the loading direction (y-direction) are prescribed on the top and
bottom surfaces at every time increment. The incremental update scheme
of updating boundary conditions is described in section 3.3.2. Rotational
degrees of freedom (dof) are constrained and the remaining dofs have
traction free boundary conditions.

3.4.3. Material parameters

The following material parameters for tungsten are used in all simulations: lattice constant $a_0 = 3.165$ Å and $b = 2.741$ Å. The elastic moduli for tungsten are $C_{11} = 522.4$ GPa, $C_{12} = 204.4$ GPa and $C_{44} = 160.6$ GPa which gives an anisotropic factor $A = 1.01$. The shear modulus of W is $\mu = 159.5$ GPa. For the non-screw dislocations, the material parameters used in the mobility Eq. (3.12) are the mass per unit length $m_0 = 1.1 \times 10^{-16}$ kg/m and the drag coefficient $B = 1.0 \times 10^{-4}$ Pa s.

4. Results

In this section, the DDD code is used in the simulations of various dislocation configurations. The final aim is to study the evolution of dislocation microstructure in W micropillars and correlate the stress-strain response with the dominant mechanisms. To achieve this objective, the investigations performed in this work are divided into three parts:

First, the finite temperature behavior of isolated single screw dislocation in tension and compression loadings for several orientations are presented. The implemented algorithm is validated against the input atomistic data with respect to the CRSS and slip plane of isolated screw dislocation at 0 K. The mechanism of operation of single FR source in tension and compression based on the underlying atomistic parameters is studied.

Secondly, once the properties of isolated screw dislocations are studied, the role of dislocation interactions is studied in an incremental manner. The repulsive interaction between two non-coplanar screw dislocations with unlike Burgers vectors and interaction between a mixed and screw dislocation is examined.

Finally, further simulations involving FR sources are performed with the aim of understanding the multiplication mechanisms inside micrometer sized-pillars. First a system with only two FR sources in which one slip system has the highest resolved shear stress and the other is inactive but introduces a stress inhomogeneity in the vicinity of the active dislocations. This is followed by investigations of deformation in micropillars with different aspect ratios in which all the glide systems are populated with randomly distributed FR sources. The simulation setup used in this work is described in section 3.4.

4.1. Uniaxial tension and compression loading on an isolated a/2$\langle 111 \rangle$ screw dislocation
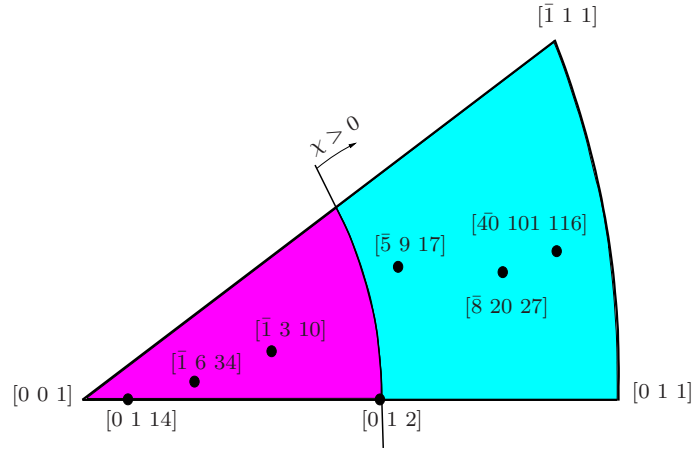
Figure 4.1.: Loading axis in $[001] - [011] - [\bar{1}11]$ stereographic triangle indicating the positive sense of χ for tension. The sense of χ is reversed in compression.

At first, the response of single a/2$\langle 111 \rangle$ screw dislocations in tungsten is examined under uniaxial tension and compression along different crystallographic orientations as shown in Fig. 4.1. For all the orientations considered, the $(\bar{1}01)$ crystallographic plane is the plane with the highest resolved shear stress. The velocity of the screw dislocations is computed from Eq. (2.5).

In order to establish an yield criterion for single dislocations an equivalent critical velocity is derived from the macroscopic strain rate given by the Orowan equation

$$\dot{\gamma} = \rho_m b v \qquad (4.1)$$

where $\dot{\gamma}$ is the shear strain rate, ρ_m is the density of mobile screw dislocations, b is the magnitude of Burgers vector and v is the average velocity of the screw dislocation. For our computation the numerical values chosen are $\rho_m = 10^{12}$ m^{-2}. The yield stress is defined to be the shear

stress on the MRSSP required for the screw dislocation to attain a magnitude of velocity of 1 μm s^{-1} which corresponds to a plastic strain rate $\dot{\gamma} = 2.7 \times 10^{-4}$ s^{-1} similar to the experiments on W in [177]. The calculations were performed up to a temperature of 800 K which is the athermal temperature for W obtained from experiments [106].

Fig. 4.2 shows the CRSS as a function of temperature up to 800 K for three of the orientations shown in Fig. 4.1. The general trend for all orientations is the same. The CRSS strongly decreases with increasing temperature, displaying two different regimes both in tension and compression. The high temperature, low stress regime is almost linear and largely dominated by the work term in Eq. (3.16), while all terms are important in the steeper low-temperature high stress regime. As an illustration, the two regimes are marked in Fig. 4.2(b) with II and I respectively. The CRSS depends on orientation and ranges from below 4 GPa to 6 GPa at 0 K. The orientation dependence of the CRSS is already much weaker at room temperature, where values range from 1.8 to 2.3 GPa. The orientation dependence disappears at 800K.

For the same orientation, the sense of shearing is reversed and the shape of the CRSS-T curve is somewhat different when changing from tension to compression. In terms of model parameters, each orientation corresponds to a different χ and η respectively. At lower temperatures and for orientations shown in Fig. 4.1, the CRSS in uniaxial compression is higher than in uniaxial tension. The different orientations correspond to different non-Schmid stresses σ. In both tension and compression, the CRSS at 0 K obtained by extrapolation converge to different values and this value is additionally orientation dependent.

In tension, the glide plane is always the ($\bar{1}01$) plane ($\overline{\psi} = 0°$) for all orientations.

In compression the atomistic data at 0 K [9,10] show that the dislocation always moves on the ($\bar{1}01$) plane for orientations in the cyan region in figure 4.1, while the dislocation moves on the low-Schmid factor ($\bar{1}10$) plane for orientations in the magenta region in figure 4.1. Hence the asymmetry in orientation dependence manifests itself not only in terms of the CRSS but also in terms of the preferred glide plane on which screw dislocations move. This atomistic aspect is recovered by our model and will be analyzed in more detail in section 4.1.1.

(a)

(b)

(c)
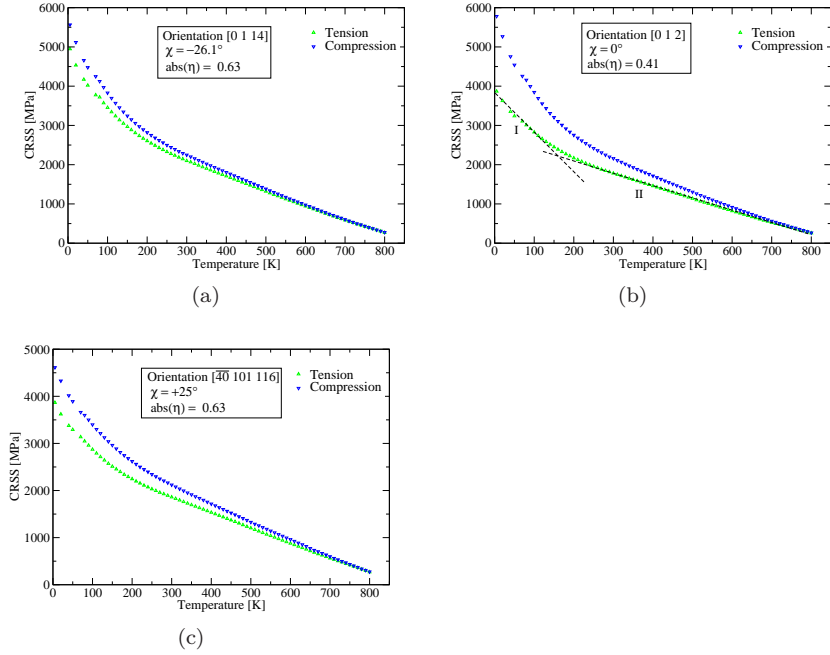
Figure 4.2.: CRSS vs temperature curves for different orientations of applied loading shown in the insets.

4.1.1. Slip planes in uniaxial tension and compression

Fig. 4.3 shows the variation of the macroscopic slip angle $\overline{\psi}$ with temperature T for different orientations in tension and compression obtained using Eq. (3.19).

In tensile loading and for temperatures up to 300 K, $|\overline{\psi}|$ stays at 0° which means that $|v_{gl}|$ in Eq. (3.18) is determined entirely by the activation enthalpy on the $(\bar{1}01)$ plane irrespective of the orientation of the MRSSP and the magnitude of non-Schmid stresses. With increasing temperature $\overline{\psi}$ tends to deviate increasingly away from the low index $(\bar{1}01)$ plane and
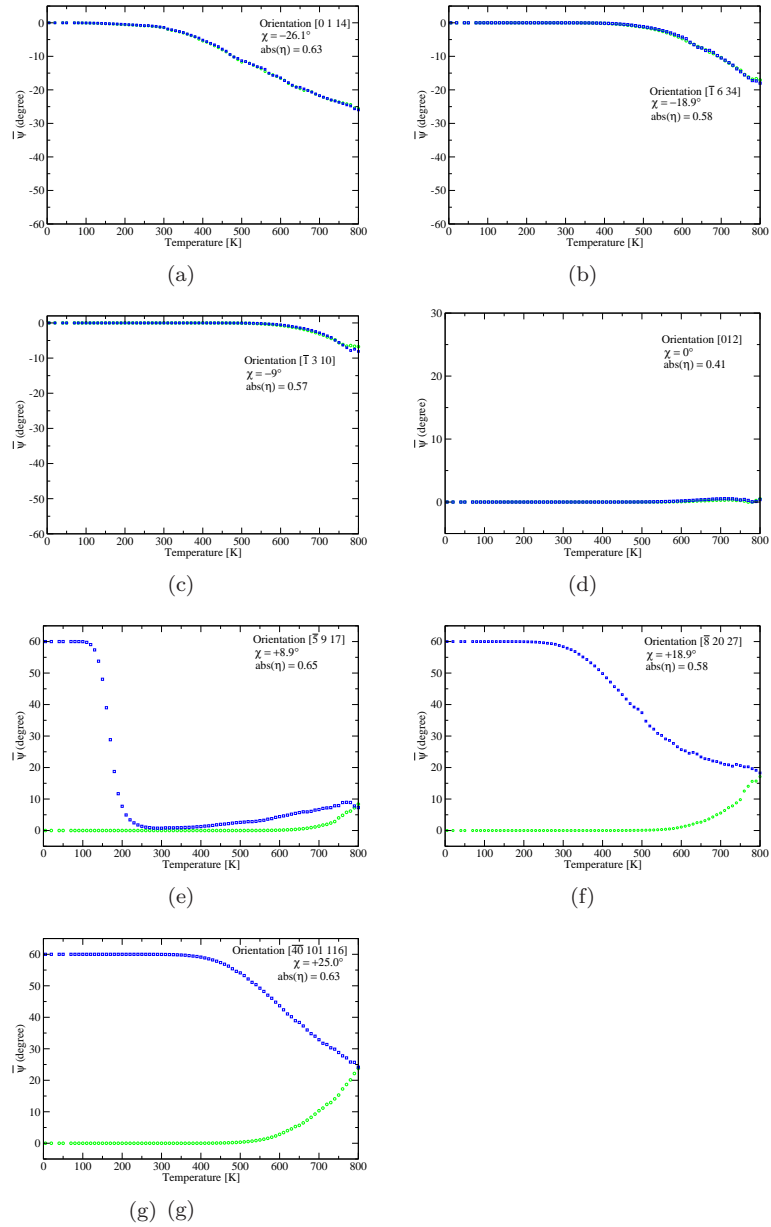
Figure 4.3.: Temperature dependence of $\overline{\psi}$ for different orientations : (○) for tension and (□) for compression.

contributions from other {110} planes become significant. The average slip direction $\overline{\psi}$ moves towards the MRSSP. In tension, the slip angle $\overline{\psi}$ always stays within $\pm 30°$ for all orientations in the entire temperature range. It is however interesting to note that the deviation of $\overline{\psi}$ from $0°$ towards χ occurs at lower temperatures for $\chi < 0$ as compared to $\chi > 0$. This suggests that it is easier to operate a secondary plane in the twinning sense (magenta region) than in the antitwinning sense (cyan).

In compression, the general behavior and all trends are identical to tensile loading for orientations with $\chi < 0°$ (magenta region in figure 4.1). For orientations with $\chi > 0°$ (cyan region) the slip trace in compression is more complex. At low temperature the glide plane at $\psi = +60°$ is chosen compared to the $\psi = 0°$ plane in tension. The slip trace at low temperature is well defined. Deviations from this plane which may be viewed as an indication of wavy slip only occur at higher temperatures. With increasing temperature, slip on the $\psi = 0°$ plane becomes increasingly more significant and the average deformation direction also moves towards the MRSSP.

4.2. Validation of the implemented algorithm

The above mentioned examples also serve as a test of the consistency of the implemented algorithm against the underlying atomistic data. This is because

(a) The tension-compression asymmetry and orientation dependent behavior of individual dislocations is reproduced from 0 K atomistic simulations

(b) The same slip geometry in DDD and atomistics in both tension and compression is reproduced

(c) A similar order of the CRSS extrapolated to 0 K, between different slip planes is observed for isolated screw dislocations in DDD and atomistic studies.

4.3. Operation of FR sources in tension and compression
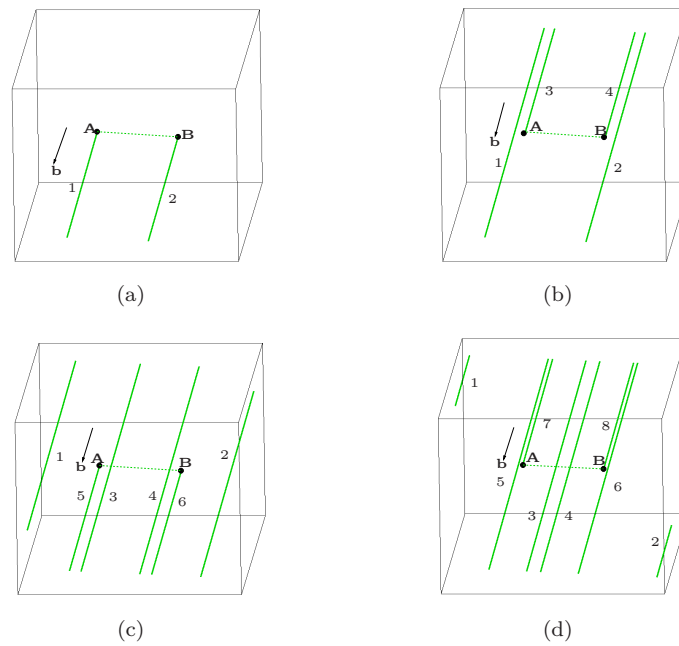
Figure 4.4.: The figures show successive steps of operation of the FR source with pinning points **A** and **B**, loaded in tension. The dislocation lines are colored according to their habit plane. Green color of dislocation means it lies on the $(\bar{1}01)$ plane (refer text for description).

Here, the operation of a single FR source shown in Fig. 4.4 in tension and compression loading is presented. The source between the pinning points marked by **A** and **B** respectively is in edge orientation and placed on the $(\bar{1}01)$ plane as shown. The length of the source is 380 nm. Such a source is subjected to both tension and compression loading at a temperature of 200 K. The applied strain rate is 5000 s^{-1}. The source is placed

in the middle of a pillar with edge length 1 μm and aspect ratio $1:2:1$. The first activation of the source in tension geometrically follows the same steps as described in [143] after the critical stress for bow-out of the source is reached on the $(\bar{1}01)$ plane. The non-screw oriented dislocation segments are highly mobile and escape the volume very quickly at low stresses, leaving two long screw dislocation dipoles. Thereafter each of the arms operates as an individual source. This is different from a FR source in an *fcc* metal where the arms recombine resulting in a configuration involving the original FR source surrounded by a dislocation loop.

The long screw dislocations move at atomistic values of the CRSS as shown in the stress strain curves in figure 4.6. Snapshots of the operation of the source in tension and compression are shown for the orientation $[\bar{8}\ 20\ 27]$ in Fig. 4.4 and 4.5 respectively.

In tension (Fig. 4.4), the dislocation motion is confined to the highest stressed $(\bar{1}01)$ plane. The mechanism of source operation is similar for all orientations and both the edge and screw dislocations move only on this plane. The edge and mixed dislocations quickly move out of the volume leaving behind the screw dipoles labeled 1 and 2 in Fig. 4.4(a); the screw dislocations then get activated at their CRSS which generate small edge dislocations around the pinning points. These edge dislocations quickly leave the volume and generate further screw dislocation dipoles 3 and 4 in Fig. 4.4(b); Upon further loading, they get activated and create the inner screw dipoles 3 and 4 as shown in Fig. 4.4(c); Fig. 4.4(d) shows that dislocations 1 and 2 leave the volume and 3 and 4 annihilate. This leaves the arms 5 and 6 and the entire sequence of steps is repeated with generation of dipoles around the pinning points.

In compression (Fig. 4.5), the source activation also begins with the motion of the edge dislocations on the highest resolved shear stress plane generating long screw dislocations on the $(\bar{1}01)$ plane. The situation in Fig. 4.5(a) is similar to that in tension but of course slip occurs in the opposite direction due to the reversed loading; the screw dislocations 1 and 2 get activated at their CRSS and move via cross-slip on the $(\bar{1}10)$ plane which has a lower activation enthalpy but not the highest resolved shear stress as shown in Fig. 4.5(b).

(a)

(b)

(c)

(d)

(e)

Figure 4.5.: The figures show the first steps of operation of the FR source in compression with pinning points **A** and **B**. The dislocation lines are colored according to their habit plane. Green color of dislocation means it lies on the $(\bar{1}01)$ plane and cyan indicates the $(\bar{1}10)$ plane (refer text for more details).
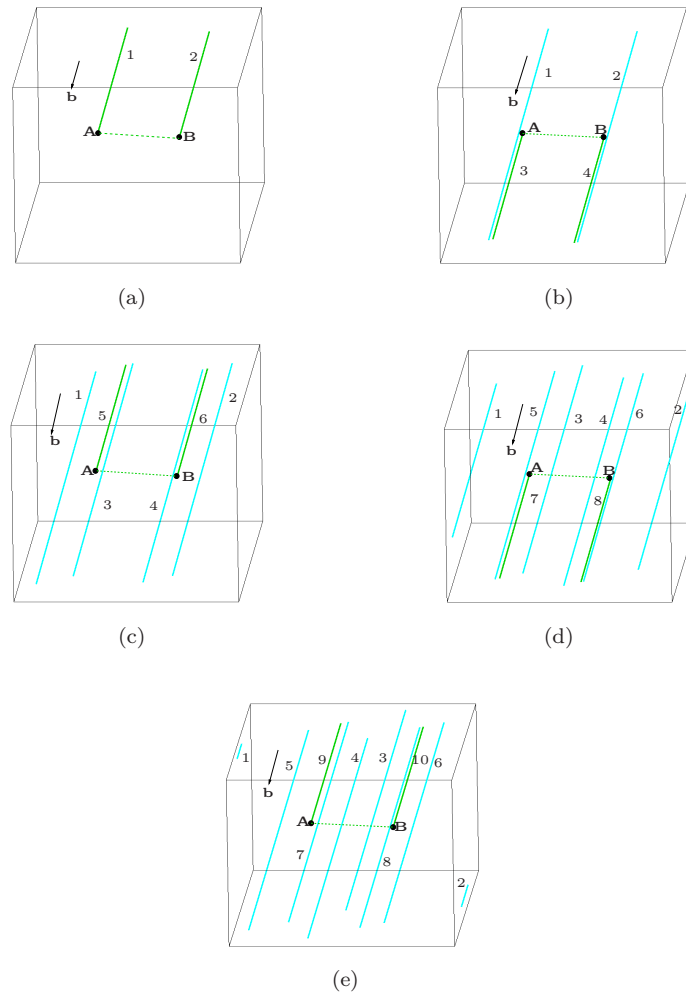
Spiral sources are thereby generated on parallel planes which operate independently and no annihilation is possible. This leads to an increase in dislocation density and a different internal stress state. The motion of the edge dislocations on ($\bar{1}01$) plane generates further screw dislocation dipoles 3 and 4 respectively; In Fig. 4.5(c), these newly generated spiral sources get activated and 3 and 4 move again via cross-slip on parallel ($\bar{1}10$) planes; In Fig. 4.5(d), the dipole pair 3 and 4 move on parallel planes and hence do not annihilate as in tension; Finally, Fig. 4.5(e) shows that the 3 and 4 are still within and volume and move away from each other on parallel planes with the source being in position similar to Fig. 4.5(a).

The stress-strain curve for the single FR source in tension and compression is shown in Fig. 4.6 with subscripts T and C respectively. The corresponding stress is then identified as the flow stress needed to maintain steady state plastic deformation in the pillar. The orientation dependence of flow stress in tension and compression can be identified. The flow stress in compression is always higher than in tension. After yielding in both tension and compression, a constant flow-stress is required for the periodic activation of the single-armed sources.

4.4. Repulsive interaction between a/2$\langle 111 \rangle$ screw dislocations

After having established the basic framework for the motion of single dislocations, we consider here the interaction of two non-parallel screw dislocations as shown in Fig. 4.7 at 200 K. The dislocations 1 and 2 have Burgers vector $\mathbf{b}_1$ and $\mathbf{b}_2$. $\mathbf{b}_1$ is always chosen as a/2[111] and $\mathbf{b}_2$ is varied. The two dislocations are placed inside a pillar of square cross-section with edge length 1 μm. The aspect ratio of the pillar is chosen to be $1:2:1$ and subjected to loading along the long-axis parallel to the [$\bar{1}$ 4 9] direction. Separate loading cases in tension and compression are considered.

The line orientations of the dislocation are chosen such that the PK-force due to the mutual stress fields of the dislocations is repulsive. Attractive
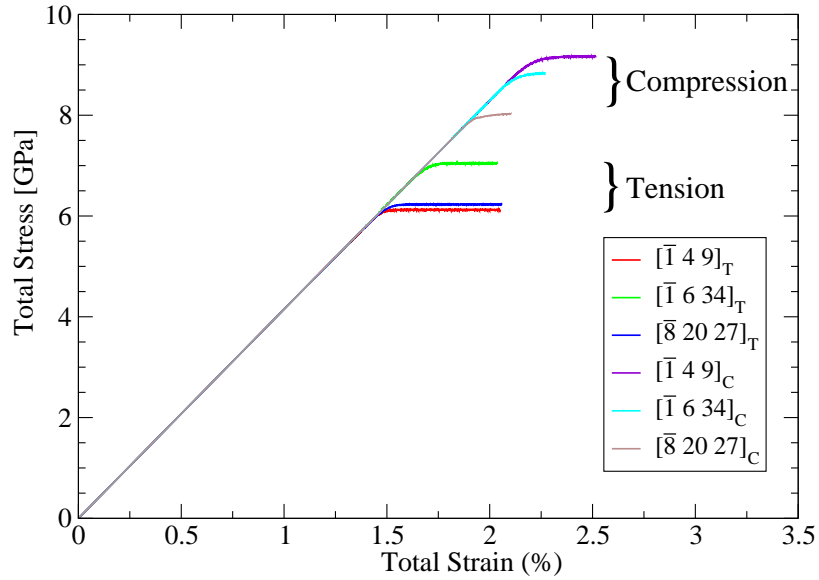
Figure 4.6.: Normal stress vs strain curves for loading in tension and compression for orientations shown in the legend.

interactions are not considered as they are known to form a ⟨100⟩ junctions [178]. The shortest distance of approach between the screw dislocations is denoted by d. This represents the simplest case of interacting screw dislocations and is of interest primarily due to the fact that screw dislocations are expected to be predominant during deformation. Pairwise interaction with all Burgers vectors is considered. The other possible Burgers vectors $\mathbf{b}_2$ are $a/2[\bar{1}11]$, $a/2[1\bar{1}1]$ and $a/2[11\bar{1}]$. Each of these slip directions is stressed differently. The $[1\bar{1}1]$ direction is coplanar with the $(\bar{1}01)$ plane on which dislocation 1 glides. Therefore it is not considered here since it will not lead to any intersection with $a/2[111]$ screw dislocation. Of the remaining two slip directions, the corresponding highest stressed slip systems are the $(101)[\bar{1}11]$ and the $(011)[11\bar{1}]$ with Schmid factors 0.47 and 0.32 respectively.
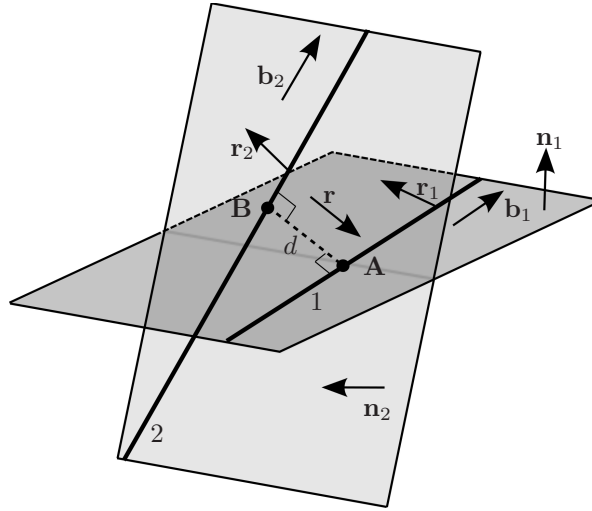
Figure 4.7.: Schematic view of the configuration of repulsively interacting screw dislocations **1** and **2** with Burgers vectors $\mathbf{b}_1$ and $\mathbf{b}_2$ respectively. The directions $\mathbf{r}_1$ and $\mathbf{r}_2$ are the directions of the respective PK-force due to the macroscopic loading state. The vector $\mathbf{r}$ and the distance d denotes the direction of approach and the nearest distance between the two approaching screw dislocations. **A** and **B** are the points of strongest interaction on the dislocations 1 and 2 respectively.

We first consider the interaction between the highest and low stressed non-coplanar unlike slip directions a/2[111] and a/2[11$\bar{1}$] dislocations denoted as 1 and 2 in Fig. 4.7. Upon tensile loading the CRSS of screw dislocation 1 is reached first and it begins to glide on the ($\bar{1}$01) plane. The dislocations 1 glides along the [$\bar{1}$2$\bar{1}$] direction. It approaches dislocation 2 which is still immobile. The resolved stress component due to interaction acts on dislocation 1 against the direction of the applied stress and acts on the dislocation 2 in the direction of applied stress.

Fig. 4.8(a) and Fig. 4.8(b) show the variation of the resolved shear stress on the strongest interacting segments of screw dislocations 1 and 2 due to their mutual interactions and total stress respectively. As the dislocation 1 approaches 2, the interaction stresses play an increasingly greater role which is shown in Fig. 4.8.

When d ≈ 100 *b*, the maximum interaction stress between the dislocations is about 170 MPa and is much lower than the corresponding CRSS of the screw dislocation. At a distance of d ≈ 35 *b*, the total resolved stress on the nearest approach segment of dislocation 1 and dislocation 2 measured on the ($\bar{1}$01) and (011) planes are equal, even though macroscopically the slip system on which dislocation 1 glides has a higher Schmid factor.
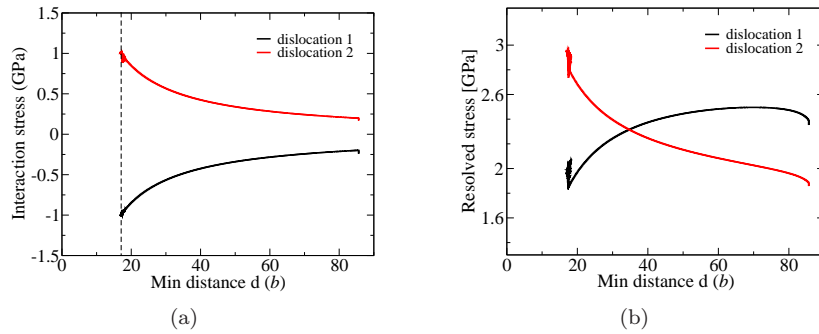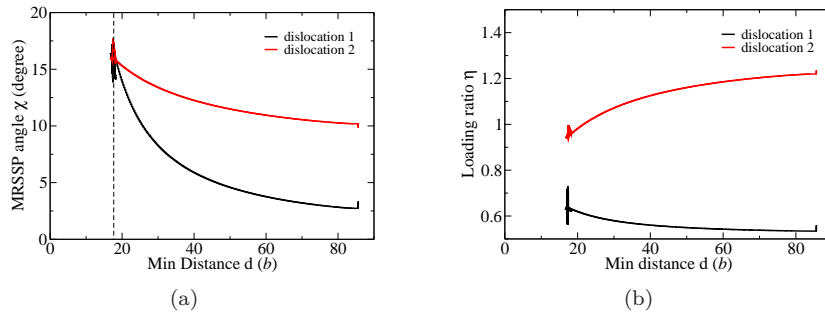

Figure 4.8.: For the case of repulsively interaction screw dislocations 1 and 2 with Burgers vectors a/2[111] and a/2[11$\bar{1}$] respectively, (a) shows the variation of the interaction stress and (b) variation of the total stress, both resolved on the (011) and ($\bar{1}$01) planes for dislocation 1 and 2 respectively, plotted against the minimum distance of approach *d* between the two dislocations. The stress variation of the strongest interacting dislocation segment of each dislocation is shown. *d* is displayed in the unit of magnitude of Burgers vector respectively, **b**.

At a distance of 18 *b*, dislocation 2 gets activated and glides on the (011) plane. The velocity of dislocation 2 increases sharply at this distance. A dynamic equilibrium is established at this distance and both dislocations glide then collectively maintaining a constant distance. Both the screw dislocations remain rigid at this distance. Furthermore, the total resolved stress contributed by interactions at this distance is about 950 MPa.

As the two dislocations approach each other, the loading parameters on the two screw dislocations constantly changes with the distance of approach. Figs. 4.9(a) and 4.9(b) show the variation of the loading parameters χ and η, on the nearest approach segments of the dislocations 1 and 2. The corresponding loading parameters due to the uniaxial macro-

scopic loading alone (without interactions) along the $[\bar{1}\ 4\ 9]$ orientation are $\chi \approx 0°$, $\eta \approx 0.51$ and $\chi \approx 9°$, $\eta \approx 1.2$ for dislocations 1 and 2 respectively. During the entire course of motion of the two dislocations, the MRSSP angle χ of both systems remains within 30° of the corresponding primary planes $(\bar{1}01)$ and (011) respectively. Cross-slip is therefore not observed (see section 3.2.4).

Figure 4.9.: For the case of repulsively interacting screw dislocations with Burgers vectors a/2[111] and a/2[11$\bar{1}$] respectively, (a) shows the variation of the MRSSP angle χ and (b) variation of the loading ratio η, with the minimum distance of approach for the strongest interacting dislocation segments of dislocation 1 and 2. d is displayed in the unit of magnitude of Burgers vector **b**.

The repulsive interaction between screw dislocations with a/2[111] and a/2[$\bar{1}$11] Burgers vector shows the same trend as the $a/2[111]-a/2[11\bar{1}]$ system i.e. dislocation 1 approaches 2 and at an approach distance of $d \approx$ 20 b, the two begin to glide collectively on their respective planes. Dislocations 1 and 2 glide on the $(\bar{1}01)$ and (101) planes respectively. The total interaction stress at this distance is 850 MPa. The activation of dislocation 2 also occurs at different local parameters compared to that imposed by the macroscopic loading state.

Each of the above systems of interacting dislocations is now subjected to compression loading along the $[\bar{1}\ 4\ 9]$ direction. The line directions of the screw dislocation are reversed so that the direction of motion of dislocations remains the same as in tension.

The repulsive interaction between a/2[111] and a/2[11$\bar{1}$] screw dislocations in compression shows the same trend of collective motion of as in tension. While, dislocation 1 glides on the ($\bar{1}$01) plane similar to the scenario in tension, dislocation 2 glides on the (101) plane compared to the (011) plane in tension. Fig. 4.10 shows the relative orientations of the planes and the dislocations. As the mobile dislocation 1 approaches, dislocation 2 cross-slips from the higher stressed (011) onto the low-stressed (101) plane. The nearest distance of approach at which the collective motion occurs is about 14 b.
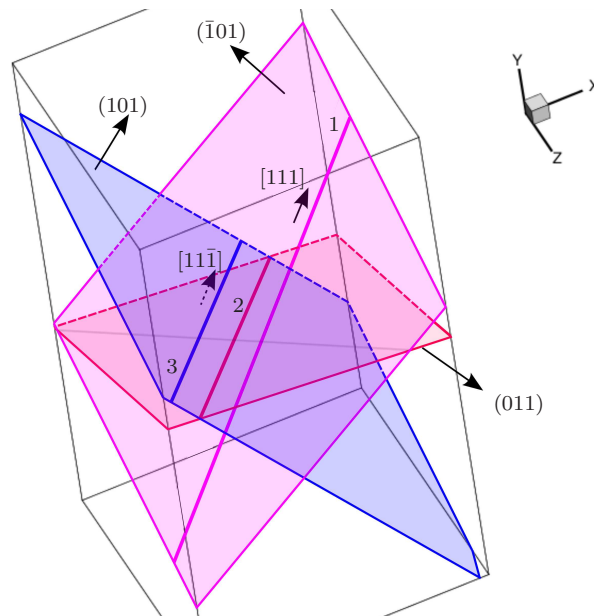
Figure 4.10.: The interaction between screw dislocation 1 and 2 with Burgers vectors a/2[111] a/2[11$\bar{1}$] respectively in compression causes a cross-slip of dislocation 2 from the (011) habit plane to the (101) plane.

The repulsive interaction between a/2[111] and a/2[$\bar{1}$11] screw dislocations in compression is similar in tension with respect to the glide plane on which the dislocation motion occurs, with the only difference being

that the dislocation 2 activates at a distance of 75 b, compared to 20 b in tension. The local parameters in compression for each of the pair of interactions change in a similar manner as in tension.

4.5. Repulsive interaction between mixed and screw dislocation

(a)   (b)
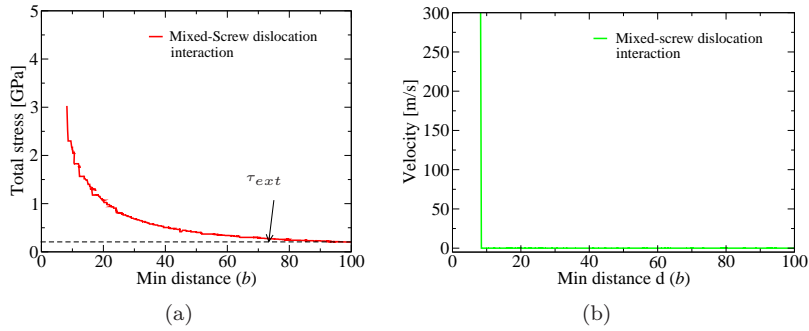
Figure 4.11.: (a) shows the variation of the total resolved stress resolved on the $(\bar{1}01)$ plane on the screw dislocation due to the interaction with $a/2[\bar{1}11]$ mixed dislocation, with the minimum distance of approach d. The screw dislocation gets activated as the local stress on the screw dislocation due to interaction exceeds its CRSS and ; (b) Velocity of the screw dislocation due to approaching mixed dislocation shows a rapid increase from zero to 300 m s^{-1}. The external applied stress is still

Here, the interaction between a mixed dislocation with $a/2[\bar{1}11]$ Burgers vector moving on (101) with $a/2[111]$ screw dislocation is examined. At an applied stress of $\tau_{ext} = 60\ MPa$, the mixed dislocation moves athermally on the (101) plane. As the mixed dislocation approaches the immobile screw dislocation, it feels a little repulsive stress. Fig. 4.11(a) shows the stress variation on the strongest interacting screw segment due to the approaching mixed dislocation. At a distance of separation of about 8 b, the screw dislocation is activated. The velocity v of the $a/2[111]$ screw dislocation shows a sharp increase and reaches the limiting velocity of 300 ms^{-1} used in the simulation. The mixed dislocation eventually cuts through the

screw dislocation and continues to glide further on the (101) plane and exits the volume.

The exact distance to which the screw dislocation can glide collectively depends on the duration of interaction between the mixed and the screw dislocation and depends on the strain rate since it determines the velocity of the mixed dislocation (Eq. (4.1)).

4.6. Uniaxial tensile loading on pillar with two FR sources

In order to gain insights into the dislocation multiplication mechanisms and their contribution towards flow-stress, several simulations with simple arrangements of two dislocation FR sources inside pillars were performed. The configuration of sources are chosen such that both attractive and repulsive interactions are possible. Here, we show the evolution of one configuration shown in Fig. 4.12 with Burgers vectors a/2[111] and a/2[1$\bar{1}$1] . The two dislocation sources are initially in non-screw orientation on ($\bar{1}$01) and (110) planes respectively. The aspect ratio of the pillar is 1:2:1. The length of the pillar is taken as 1 μm. The system is subjected to tension loading along the [$\bar{1}$ 4 9] direction at a temperature of 200 K.

Four different simulations were performed to determine the sensitivity of the response of the pillar to critical input parameters. These parameters are the mobility of a $\langle 100 \rangle$ junction dislocations and the critical velocity of cross-slip V_{crit} (see section 3.3.2) at which a cross-slip step is allowed in the simulations. Due to lack of atomistic information on the mobility of in plane a $\langle 100 \rangle$ junctions (glissile), different mobilities of a $\langle 100 \rangle$ dislocations were tested to investigate its influence on the microstructure evolution. These configurations are summarized below:

1. sim1: $V_{crit} = 0.1 m/s$ and the mobility of co-planar $\langle 100 \rangle$ same as mixed dislocation.

2. sim2: $V_{crit} = 0.1 m/s$ and the mobility of co-planar $\langle 100 \rangle$ hundred times slower than mixed dislocation.

3. sim3: $V_{crit} = 0.1 m/s$ and $\langle 100 \rangle$ immobile.

(a)   (b)
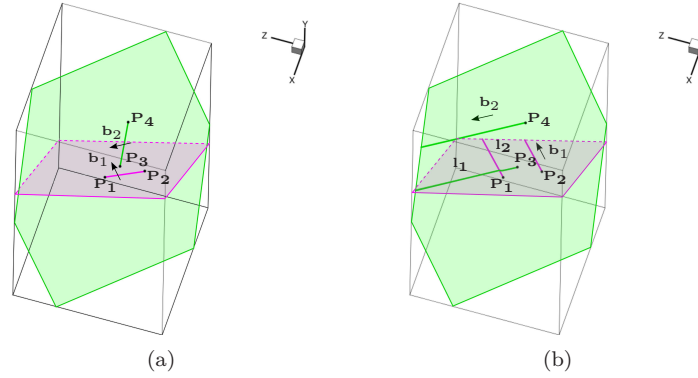
Figure 4.12.: The initial arrangement of the two sources is shown in (a). $\mathbf{P}_1\mathbf{P}_2$ and $\mathbf{P}_3\mathbf{P}_4$ are dislocation sources with Burgers vectors a/2[111] ($\mathbf{b}_1$) and a/2[11$\bar{1}$] ($\mathbf{b}_2$) respectively; (b) shows the arrangement when the mixed segments move out of the volume leaving behind the screw dipoles.

4. sim4: $V_{crit} = 0.01 m/s$ and $\langle 100 \rangle$ immobile. parameters.

The critical velocity of cross-slip is based on the studies on single FR sources and the values are chosen such that the screw dislocation become active on the cross-slip plane.

The stress-strain response of all four simulations shown in Fig. 4.13(a) displays the same trend i.e. initial elastic response followed by a drop in the total effective stress. The initial stage of activation corresponds to the motion of edge/mixed dislocations out of the volume accompanied by the generation of less mobile screw dislocations which remain inside the volume (see Fig. 4.12(b)). The screw arms l_1 and l_2 are mutually repulsive. Upon further straining, the screw dislocations with a/2[111] Burgers vector get activated at stresses close to the CRSS of screw dislocation. The peak stress corresponds to the stress required for the activation of the FR source on the ($\bar{1}$01)[111] glide system and its value is close to that of operation of a single FR source (see Fig. 4.6). The large drop in the stress is associated with a large increase in dislocation density (see Fig. 4.13(b)).
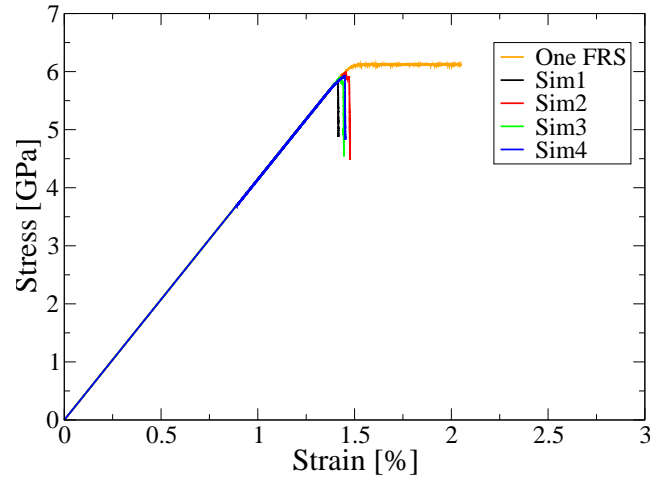
(a)
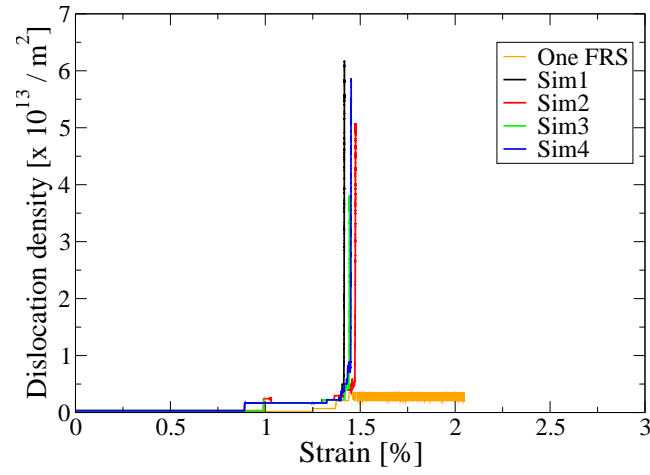
(b)

Figure 4.13.: (a) shows the stress vs strain curve for the two source system in Fig. 4.12(a) for loading in tension. In sim1, sim2 and sim3, the coplanar ⟨100⟩ disloca-tions are equally mobile as the edge, 100 times slower than edge and immobile respec-tively. Sim4 has $V_{crit} = 0.01 m/s$ and the co-planar ⟨100⟩ dislocations are immobile; (b) shows the variation of dislocation density during loading for the four simulations.

Even though the overall response is similar in all the cases, microscopically, the effect of making $\langle 100 \rangle$ junctions mobile leads to the activation of $\{110\}\langle 100 \rangle$ slip. Loops with a [010] Burgers vector are activated on the $(\bar{1}01)$ plane. In other cases, $\langle 100 \rangle$ dislocations act as pinning points for $\langle 111 \rangle$ dislocations. Since no slip in the $\langle 100 \rangle$ direction has ever been reported in *bcc* metals [4], we focus on sim4 to where the $\langle 100 \rangle$ junctions are immobile. In this case, the junctions act as pinning points.

The dislocation microstructure of sim4 after a total plastic strain of 0.27 % is shown in Fig. 4.14. The effective stress decreases to 4.8 GPa after which the simulation is stopped, since the primary interest of this investigation was to understand the mechanism of dislocation multiplications. The drop in flow-stress corresponds to a reduction of 1.4 GPa compared to the flow-stress of a single FR source as shown in the Fig. 4.13(a). The main feature of the microstructure is the presence of long and convoluted dislocation lines of screw and mixed dislocations of the a/2[111] Burgers vector which cannot be attributed to one single $\{110\}$ plane. The orientation of the dislocation lines varies quite sharply and many cusp like features can also be observed. The sharp change in orientation is due to a change in the glide plane of a segment on a dislocation line. The entire dislocation density after total plastic strain of 0.27 % shown in Fig. 4.14 is confined within a thickness of approximately 80 a_0 where a_0 is the lattice constant.

The most important feature of plastic flow is that most of the dislocation multiplication occurs due to interaction among dislocations with the same Burgers vector. The dislocations with a/2[111] Burgers vector are the most active ones and self-multiply due to interaction with dislocations gliding on parallel planes. During straining, typically, cross-slip on a region of a screw dislocation is frequently observed. Such local cross-slip events generate kinks on new planes and also change the orientation of the loop sharply. The kinks may accumulate at pinning points which lead to the formation of kink-complex consisting of several edge dislocation segments over several planes. The kink-complex have effectively a mixed character and their glide results in slip over multiple $\{110\}$ planes. Many such complexes can be identified in Fig. 4.14 and a few of the complexes reach the surface of the pillar. The change in color of a dislocation line indicates a different glide plane. The kink-complex typically get activated after reaching a critical configuration. Often such complexes intersect with other complexes of the same Burgers vector moving in opposite di-

(a)

(b)
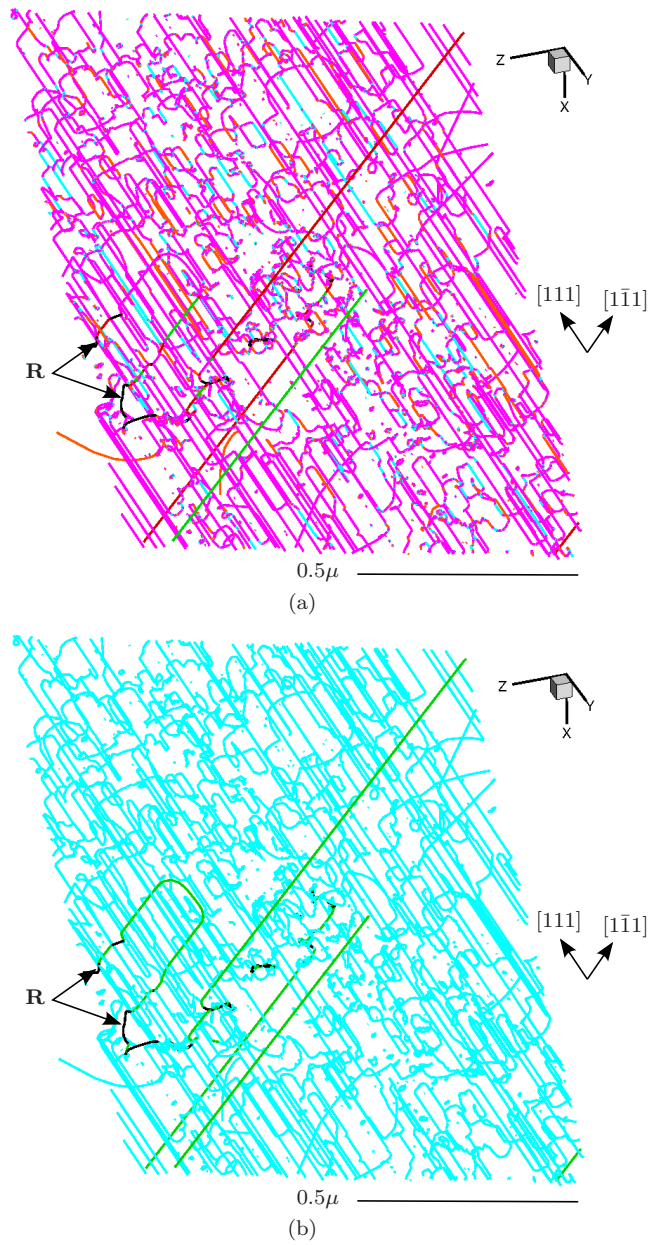
Figure 4.14.: Snap-shot of the microstructure after a total plastic strain of about 0.27%. In (a) and (b), the dislocation segments are colored according to their habit planes and Burgers vector respectively (see appendix C for the color scheme).

rections and this leads to dislocation multiplication and long connected loops are formed. The dislocation activity is dominated by dislocations with a/2[111] Burgers vector. The dislocations with a/2[1$\bar{1}$1] Burgers vector move due to interaction with a/2[111] dislocations. Plastic flow is dominated by the glide of mixed dislocations.
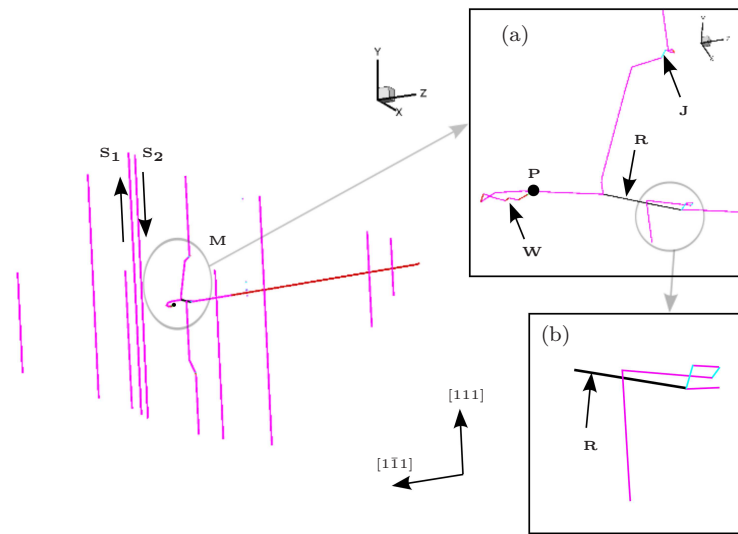
Figure 4.15.: In the figure on the left, a dislocation junction **R** with Burgers vector a [010] can be seen. The reaction is in plane and lies on the ($\bar{1}$01) plane. Screw segments S_1 and S_2 lie on parallel planes and form a dipole configuration. The circled part M is zoomed and shown in inset (a). The dislocation structure around pinning point P is highly kinked (marked by w) and is composed of several smaller segments. The direction of motion of this complex is towards the screw dipoles S_1 and S_2 which move on parallel planes. Inset (b) shows the zoomed region around the reaction clearly showing that around the junction the segments with primary Burgers vector a/2[111] are also kinked.

Fig. 4.15 shows a dislocation junction marked as **R** with a[010] Burgers vector which occurs due to the attractive reaction between dislocations with a/2[111] and a/2[1$\bar{1}$1] Burgers vector. The dislocation junctions act as pinning centers for other dislocations. A snap-shot of the simulation in Fig. 4.15 shows the geometry of dislocation network with ⟨100⟩ junctions. The junction shown in Fig. 4.15 (a) shows a close-up view of the

same configuration denoted by M. Screw dislocation segments are typically connected by jogs/kinks such as **J** over different planes . Fig. 4.15 (b) shows immobile junctions with [010] Burgers vectors. Both jogs and junctions act as pinning points where the kinks on screw dislocation get accumulated. The network around a junction is typically non-planar.

In the regime where stress-drop occurs after yielding, motion of a screw dislocation occurs due to their interaction with mixed dislocations of the same Burgers vector gliding on parallel planes. The interaction of mixed dislocations with screw dislocations results in either cross-slip of the part of screw dislocation or collective glide of the entire screw dislocation with the mixed dislocation. New screw dislocations are produced by dragging of end points of kinks in opposite directions. The newly generated screw dislocations act as new sources of dislocations due to their interaction with other mixed dislocations.

4.7. Uniaxial tension and compression loading on micrometer sized pillars

4.7.1. $[\bar{1}\ 5\ 10]$ loading orientation

The pillar with initial configuration and geometry described in section 3.4 is subjected to uniaxial compression loading at 300 K along the $[\bar{1}\ 5\ 10]$ direction. The activation enthalpy for the screw dislocations for this loading orientation is shown in Fig. 4.16 for the slip systems displayed in the legend.

The initial deformation is characterized by the motion of edge and mixed segments quickly out of the volume at stresses of the order of the critical stress needed to operate the FR sources. Edge and mixed dislocations on all slip systems get activated. The activity of the slip systems follows the Schmid law with the highest stressed slip system $(\bar{1}01)[111]$ activated first. The movement of mixed dislocations is accompanied by the generation of screw dislocation dipoles which become mobile once their corresponding CRSS is reached. A large density of immobile forest screw dislocations on the secondary slip planes is produced at the yield stress. It

must also be mentioned that even when the screw dislocations on the highly stressed slip systems are activated, some systems with very low Schmid factors are still populated with mixed dislocations in the bow-out configuration.

Fig. 4.17(a) shows the stress-strain curve for a representative sample. The yield point corresponds to the large scale motion of screw dislocations and their interaction with forest screw dislocations. Cross-slip occurs due to interactions and kinks/jogs on screw dislocations are generated. Further motion of screw dislocations results in generation of mixed dislocations and kink-complex. Past the yield point, a large stress drop is observed. The dislocation density shows a rapid increase (see Fig. 4.17(b)). Repulsive cutting due to glide of a mixed dislocation past screw dislocation forests is a characteristic feature of deformation.
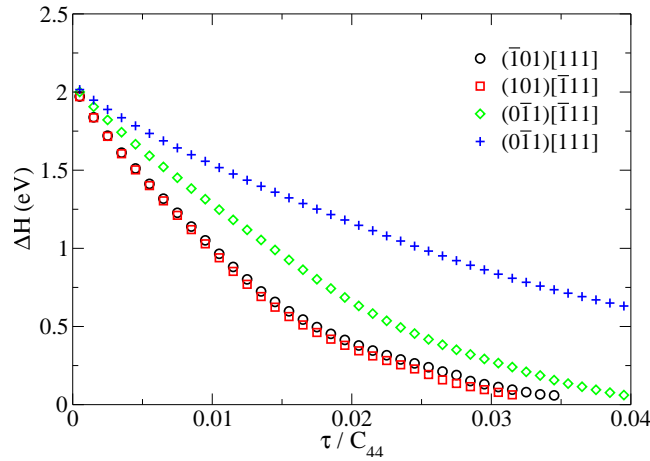
Figure 4.16.: Input activation enthalpy curves for the slip systems displayed in legend for the loading axis along the $[\bar{1}\,5\,10]$ direction.

The primary $(\bar{1}01)[111]$ and the conjugate $(101)[\bar{1}11]$ slip systems are the most active ones. The microstructure consists mostly of screw dislocation lines of these two slip systems. A snap-shot of the microstructure during deformation is shown in Fig. 4.18.
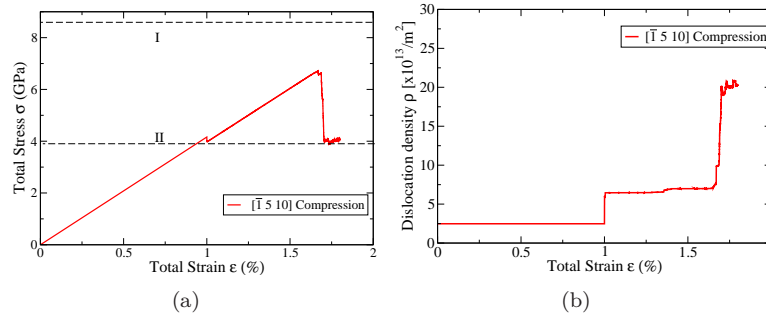
Figure 4.17.: (a) Normal stress vs strain curves for loading in compression for the $[\bar{1}\,5\,10]$ orientation; (b) Evolution of the dislocation density with strain for one sample for the $[\bar{1}\,5\,10]$ orientation whose stress-strain response is as shown in (a).

Several dislocation junctions with a $\langle 100 \rangle$ Burgers vector (marked as **J** in Fig. 4.18(a) are formed as a result of attractive interactions between $\langle 111 \rangle$ dislocations.

A key feature of the microstructure is that the screw dislocations do not lie on one single plane, but contain many kinks on several $\{110\}$ planes of its zone as shown in Fig. 4.19. The kinks can glide conservatively on the plane containing the dislocation line along the axis of the screw direction. A conflict arises when kinks nucleated on different glide planes collide when they glide towards each other. This leads to the formation of cross-kinks marked as CK in Fig. 4.19. Another peculiarity of the microstructure is that the dislocation lines meander and often change their character quite sharply. For example, in Fig. 4.19, following the loop marked $\mathbf{L}_1$ shows that the screw elements are connected over separate planes via mixed dislocation where the arms with tangents of the screw dislocation along $\mathbf{t}_1$ and $\mathbf{t}_2$ are oppositely directed. The dislocation along $\mathbf{t}_2$ is obtained by dragging of kinks by the connected mixed dislocations which can be driven at low-stresses. Kink-complex (marked $\mathbf{M}$) which have a three-dimensional character are also observed.

The most unusual dislocation motion is the motion of a dislocation segment against the direction in which it would want to move if it were

(a)

(b)
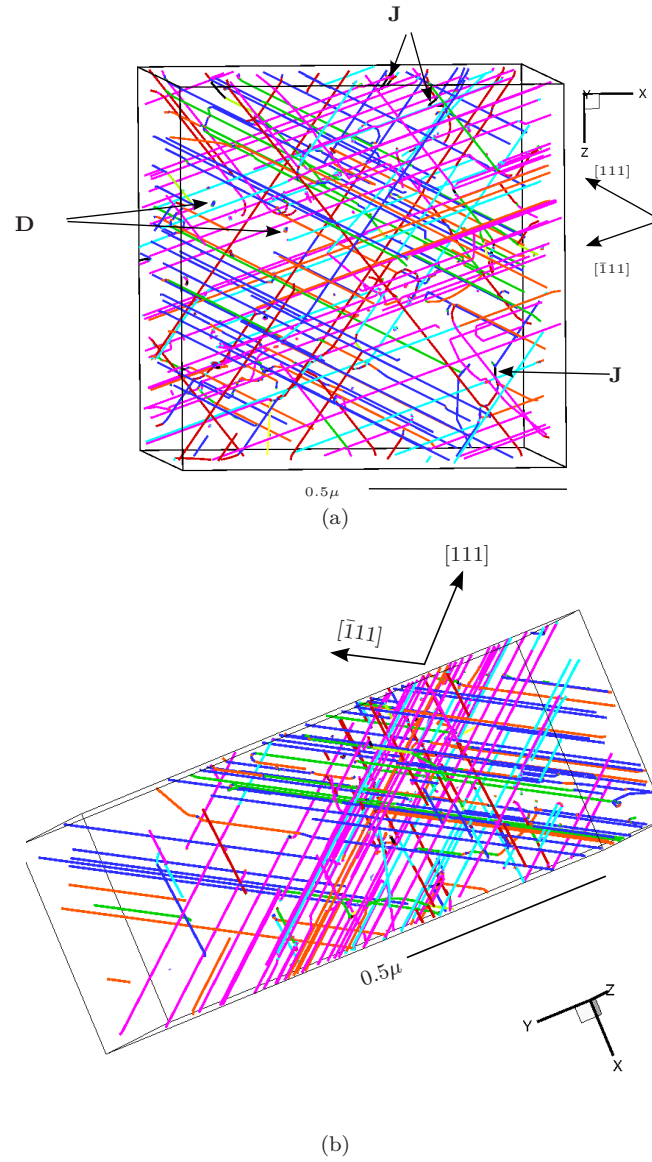
Figure 4.18.: (a) shows top view of the microstructure inside the volume during straining. Several dislocation junctions (**J**) can also be seen along with debris loops (**D**); (b) shows the same arrangement viewed parallel to the $(0\bar{1}1)$ plane. This also shows the spatial distribution of dislocation arrangement across the height of the specimen. The longest dislocation segments are those belonging to the conjugate Burgers vector. The dislocation lines are assigned colors according to their habit planes (see appendix C).

isolated. This occurs due to the presence of complex configurations such as **M** in Fig. 4.19 at the end nodes of such segments which exert an effective force in the direction opposite to that in which they would prefer to move.

The motion of screw dislocations is intermittent and it is locally pinned at internal obstacles like junctions or kinks/jogs. Another characteristic feature of deformation is that the primary $(\bar{1}01)[111]$ and the conjugate $(101)[\bar{1}11]$ slip systems are coupled. i.e. any slip activity on the primary system due to screw or mixed dislocation motion is accompanied by some activity on conjugate slip system.
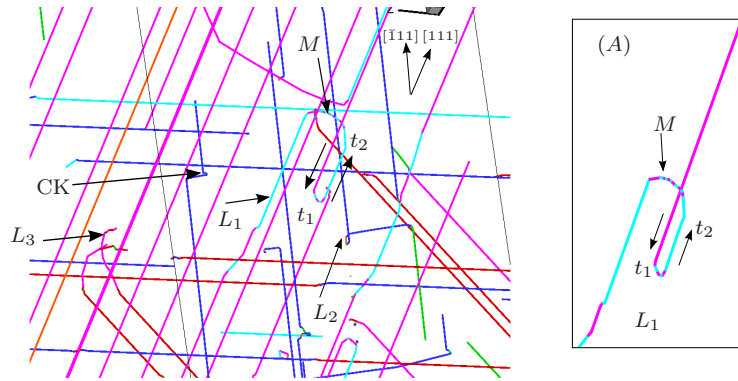
Figure 4.19.: Snap-shot from the simulation on a pillar loaded in compression along the $[\bar{1}\ 5\ 10]$ orientation. Loops L_1 and L_2 show a typical long loop observed in the simulations. The dislocation lines sharply change their orientation as shown by tangents t_1 and t_2 for L_1. Part of the loop L_1 is redrawn in the inset (A) for clarity. The loops have segments connected over parallel planes such as the mixed part marked M. Loop L_3 has a kink-complex connected with the screw part. Only the most active Burgers vector directions are shown for clarity.

Activities of slip systems

Fig. 4.20 shows the total plastic slip activity in compression direction. The lines in Fig. 4.20(a) indicate the orientations of the slip planes at the pillar surface. The primary $(\bar{1}01)[111]$ and the conjugate $(101)[\bar{1}11]$ slip systems
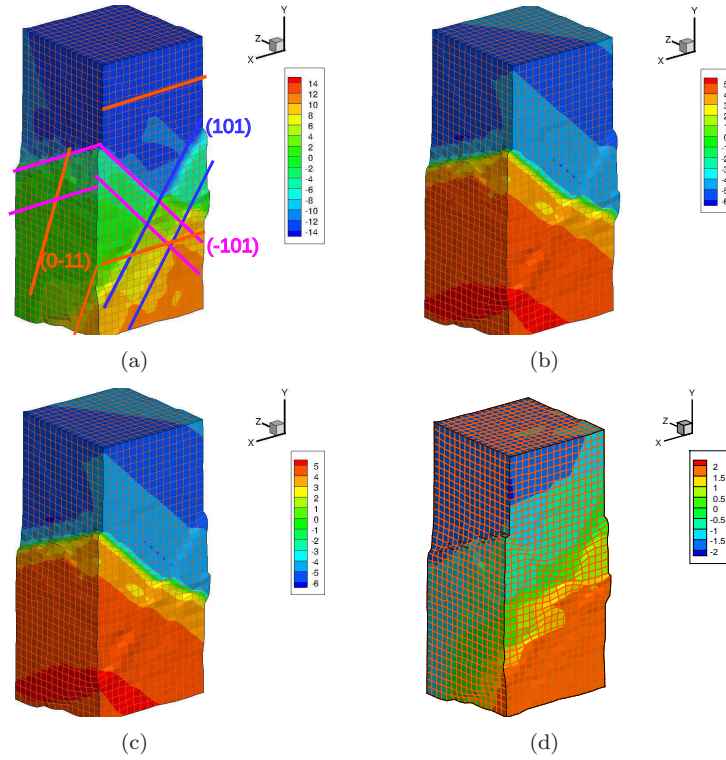
Figure 4.20.: Figures show the contributions of individual slip systems towards total deformation on a pillar loaded in compression along the $[\bar{1}\ 5\ 10]$ direction; (a) shows in color the y-component of the total plastic displacement superimposed onto the deformed pillar after a total plastic strain of 0.8% in units of lattice constant. The deformations are scaled by a factor of 15 and added to the undeformed geometry. From the history of the deformation, the contributions of individual slip systems are calculated; (b) and (c) show the contribution of the primary and the conjugate slip systems i.e. $(\bar{1}01)[111]$ and $(101)[\bar{1}11]$ respectively; (d) shows the contribution of the total plastic slip on the anomalous plane $(0\bar{1}1)$ due to glide of dislocations with both $a/2[111]$ and $a/2[\bar{1}11]$ Burgers vectors.

contribute 42% and 31% to the total plastic deformation (Fig. 4.20(b) and 4.20(c) respectively). The anomalous slip plane $(0\bar{1}1)$ contributes about

10% to the total deformation (Fig. 4.20(d)). To compute the deformation on this plane, the deformation due to both the [111] and [$\bar{1}$11] slip directions, which are co-planar on the (0$\bar{1}$1) plane, have been added. The remaining plastic strain is contributed by the remaining systems and does not lead to visible slip traces in Fig. 4.20(a). Another simulation was performed in this orientation for a different initial dislocation distribution, which showed a similar trend in plastic slip contributions.

4.7.2. [$\bar{1}$ 4 9] loading orientation

For further investigations, the [$\bar{1}$ 4 9] orientation is chosen which lies exactly on $\chi = 0°$ in Fig. 4.1. For this orientation, simulations are performed in both tension and compression. The input activation enthalpy curves for this orientation under both tension and compression are shown in Figs. 4.21(a) and 4.21(b) respectively.

(a)   (b)
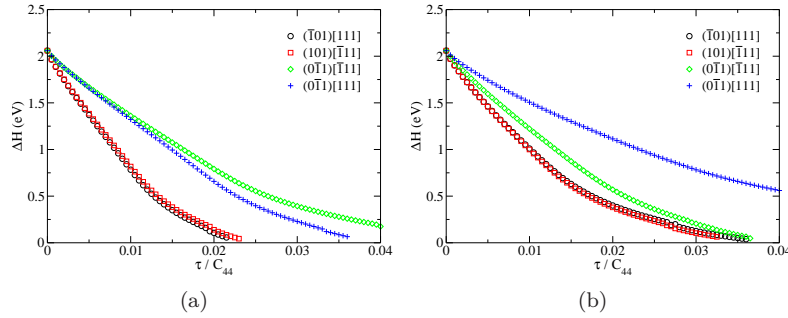
Figure 4.21.: Input activation enthalpy curves for the [$\bar{1}$ 4 9] orientation in (a) tension and (b) compression for the slip systems displayed in the legend.

The initial deformation behavior of the pillars in uniaxial tension and compression loading along the [$\bar{1}$ 4 9] orientation is similar to the [$\bar{1}$ 5 10] oriented pillars. It is again characterized by the motion of edge and mixed segments out of the volume at stresses of the order of critical stress needed to operate FR sources and the generation of screw dislocation dipoles. The screw dislocations begin to move when their corresponding CRSS are

reached. The stress-strain curves for tension and compression along with the corresponding dislocation density evolution inside the pillar is shown in Figs. 4.22(a) and 4.22(b) respectively. Past the yield point which corresponds to the CRSS of screw dislocations, a large stress drop is observed.

(a)   (b)
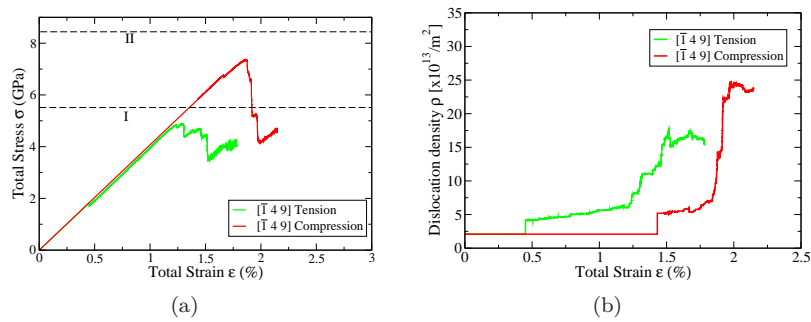
Figure 4.22.: (a) Representative normal stress vs strain curves for loading in tension and compression for the $[\bar{1}\ 4\ 9]$ orientation; (b) Evolution of the dislocation density with strain for one sample for the $[\bar{1}\ 4\ 9]$ orientation whose stress-strain response is as shown in fig (a).

The microstructure evolution inside the pillar is similar to that of the $[\bar{1}\ 5\ 10]$ loading orientation. As shown in Fig. 4.23, the screw dislocation lines of the $(\bar{1}01)[111]$ and $(101)[\bar{1}11]$ form a cross-grid and both these systems have almost equal dislocation densities. Repulsive interactions are also frequent. Several mixed dislocations move easily through the forest dislocations which are mostly screw oriented. Debris loops are generated which can glide along the $\langle 111 \rangle$ direction. Just like in the $[\bar{1}\ 5\ 10]$ orientation, screw dislocations lying over several planes connected by edge/mixed dislocations also observed in both tension and compression

Activities of slip systems

The plastic strain contributions of the individual systems are calculated for the $[\bar{1}\ 4\ 9]$ loading direction in tension and shown in Fig. 4.24. The
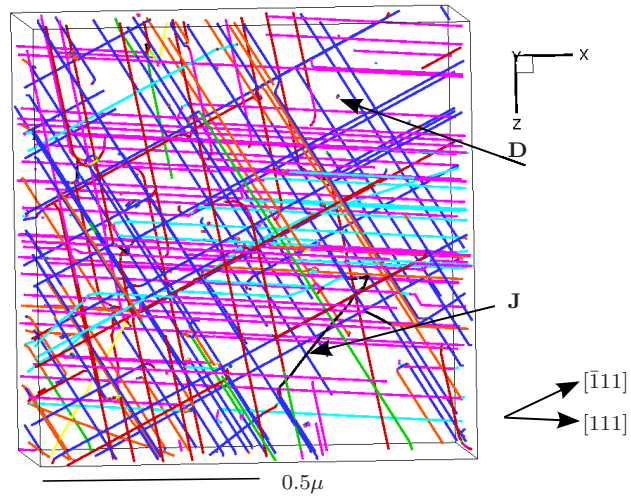
(a)
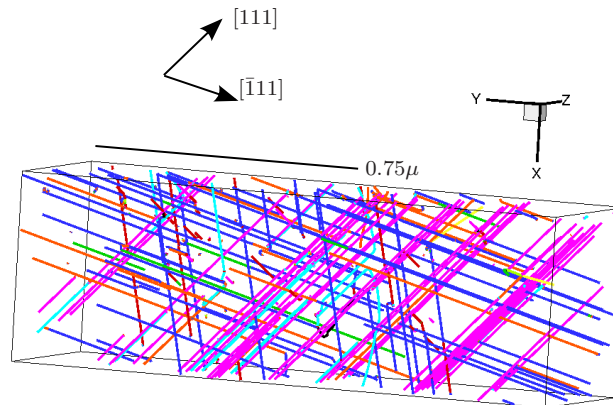
(b)

Figure 4.23.: (a) shows top view of the microstructure inside the volume during straining in compression along the $[\bar{1}\,4\,9]$ orientation. Several dislocation junctions and debris loops are marked with **J** and **D** respectively; (b) shows the same arrangement viewed parallel to the $(0\bar{1}1)$ plane which gives a sense of dislocation arrangement across the height of the specimen. The dislocation lines are assigned colors according to their habit planes.

primary and the conjugate slip systems contribute 42% and 35% to the total plastic deformation (Fig. 4.24(b) and Fig. 4.24(c) respectively)). The anomalous slip plane $(0\bar{1}1)$ contributes about 9% to the total deformation (Fig. 4.24(d)) from the a/2[111] and a/2[$\bar{1}$11] Burgers vectors. The remaining plastic strain is contributed by the nine remaining systems and does not lead to visible slip traces in Fig. 4.24(a). Several simulations were performed for this orientation with different initial distributions of FR sources and a similar trend in the stress-strain response and the overall deformation was observed.

For compression, the plastic strain contributions of the individual systems are shown in Fig. 4.25. The primary $(\bar{1}01)[111]$ and the conjugate $(101)[\bar{1}11]$ slip systems contribute 32% and 39% to the total deformation (Fig. 4.25(b) and Fig. 4.25(c) respectively). The anomalous slip plane $(0\bar{1}1)$ in compression contributes about 15% to the total deformation (Fig. 4.25(d)). The $(\bar{1}10)[111]$ also contributes about 8% towards total plastic strain. The remaining plastic strain is contributed by the eight remaining systems and does not lead to visible slip traces in Fig. 4.25(a).

In general, the total contribution of the anomalous slip in compression is greater than that in tension.

4.8. Tensile loading on pillars with different surface orientations

In this section, the deformation characteristics of W pillars with different surface orientations shown in Fig. 4.26, loaded in tension along the $[\bar{1}\ 4\ 9]$ direction are presented. Pillars referred to as A and B henceforth, are oriented such that the projection of the a/2[111] directions on the top surface of the pillar is aligned along the longest and the shortest edges of the pillars respectively. The [111] direction marked with **b** makes an angle of about 78° with the normal **n**.

The stress-strain response and the dislocation evolution in both pillars A and B shown in Fig. 4.27 is similar to the 1 : 3 : 1 aspect ratio pillars. The stress-strain curve shows a large drop post the yield point corresponding to large scale motion of screw dislocations.
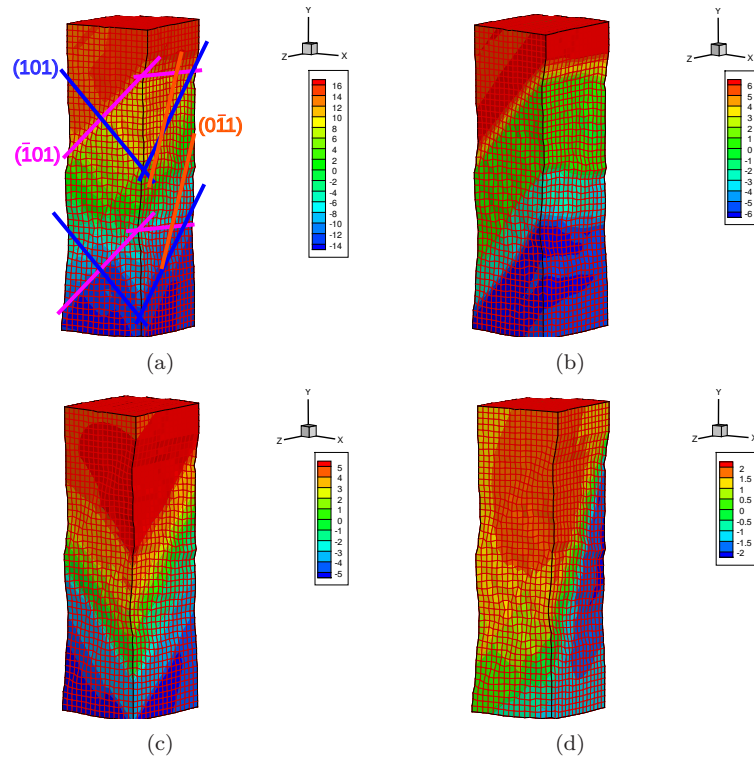
Figure 4.24.: Figures shown the contributions of individual slip systems towards total deformation on a pillar loaded in tension along the [$\bar{1}\,4\,9$] direction.(a) shows in color the y-component of the total plastic displacement superimposed onto the deformed pillar after a total plastic strain of 0.6% in units of lattice constant. The deformations are scaled by a factor of 15 and added to the undeformed geometry. From the history of the deformation, the contributions of individual slip systems are calculated; (b) and (c) show the contribution of the primary and the conjugate slip systems i.e. ($\bar{1}01$)[111] and (101)[$\bar{1}11$] respectively; (d) shows the contribution of the total plastic slip on the anomalous plane (0$\bar{1}$1) due to glide of dislocations with both a/2[111] and a/2[$\bar{1}$11] Burgers vectors.
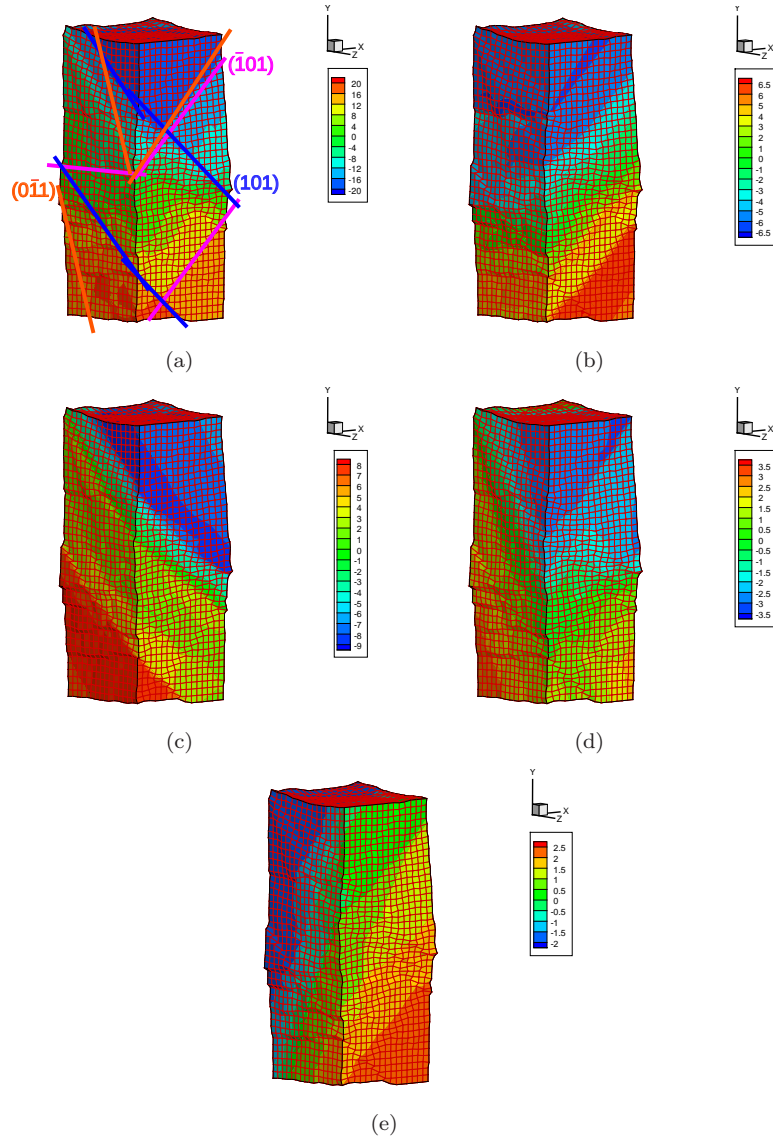
Figure 4.25.: Figures show the contributions of individual slip systems towards to-
tal deformation on a pillar loaded in compression along the $[\bar{1}\,4\,9]$ direction. (a) shows
in color in units of lattice constant the y-component of the total plastic displacement
superimposed onto the deformed pillar after a total plastic strain of 0.72% . The de-
formations are scaled by a factor of 15 and added to the undeformed geometry. From
the history of the deformation, the contributions of individual slip systems are calcu-
lated; (b) and (c) show the contribution of the primary $(\bar{1}01)[111]$ and the conjugate
$(101)[\bar{1}11]$ slip systems; (d) shows the contribution of the total plastic slip on the
anomalous plane $(0\bar{1}1)$ due to glide of dislocations with a/2[111] and a/2[$\bar{1}$11] Burgers
vectors; (e) shows the contribution of the $(\bar{1}10)[111]$ slip plane.
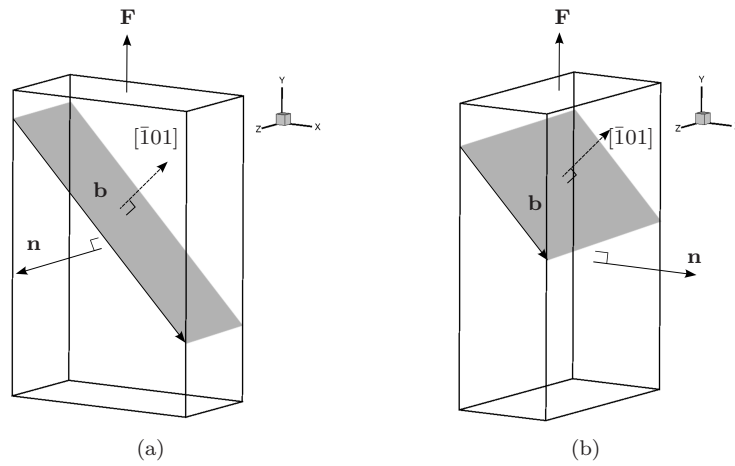
Figure 4.26.: (a) and (b) show the geometry of pillars with different surface orientations and referred to as A and B respectively. The crystal orientations with respect to the $[\bar{1}\ 4\ 9]$ direction are changed so that the pillar in orientation A and B, the screw direction projected on the xy-plane is parallel to longest and the shortest edges respectively. A The orientation of the $(\bar{1}01)$ plane is also shown. In pillar A, the screw dislocation travels a shorter distance before it reaches the surface compared to B where it must traverse a longer distance before it exits the surface.
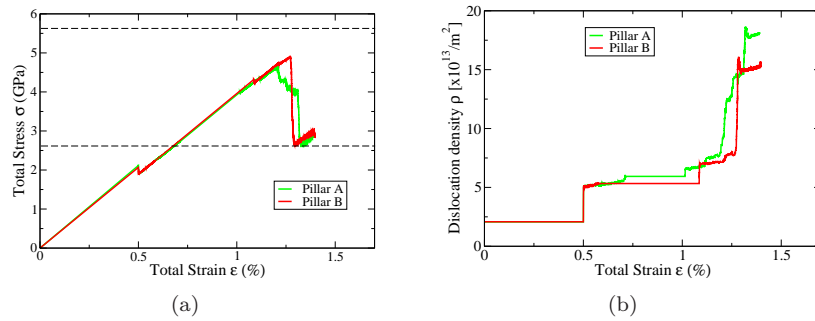
Figure 4.27.: For pillars A and B (a) shows representative normal stress vs strain curves for loading in tension for both pillars A and B; (b) shows the evolution of the dislocation density with strain.

Activities of slip systems

Fig. 4.28 shows the total plastic slip activity in tensile direction for pillar A. The lines in Fig. 4.28(a) indicate the orientations of the slip planes at the pillar surface. The primary and conjugate slip systems contribute 44% and 28% to the total deformation (Fig. 4.28(b) and Fig. 4.28(c) respectively). The anomalous slip plane $(0\bar{1}1)$ contributes about 8% to the total deformation (Fig. 4.28(d)). The contribution of the anomalous system is computed in the same manner as done for the $[\bar{1}\ 5\ 10]$ orientation.

Fig. 4.29 shows the total plastic slip activity in tensile direction for pillar B. The conjugate $(101)[\bar{1}11]$ slip system contribute 39% to the total deformation whereas the primary slip system contributes about 37%. The anomalous slip plane $(0\bar{1}1)$ contributes about 10% to the total deformation.

In summary, the relative contribution of conjugate slip system for pillar B towards total plastic slip increases compared to pillar A and it is about the same as that of the primary slip system.
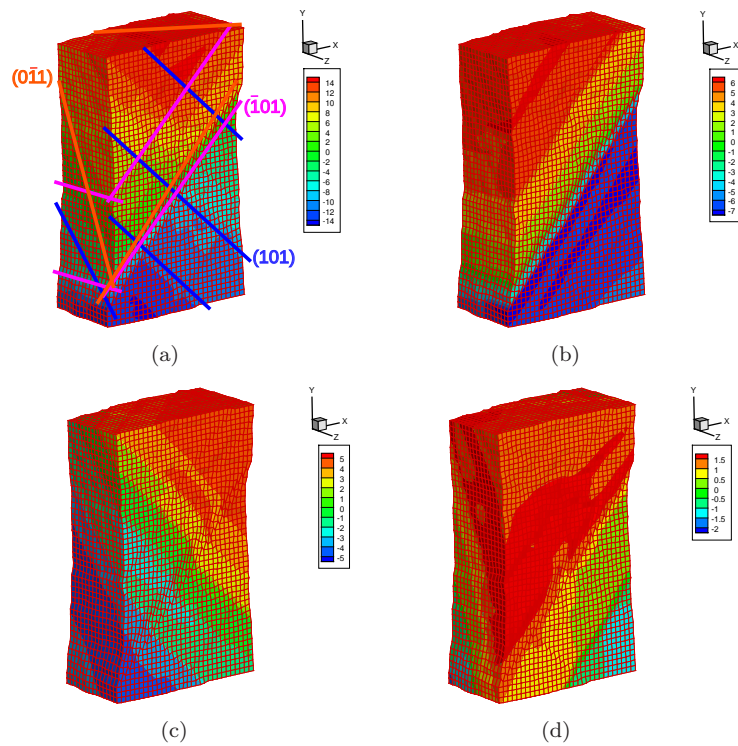
Figure 4.28.: (a) shows for pillar geometry A the y-component of the total plastic displacement superimposed onto the deformed pillar after a total plastic strain of 0.5% in units of lattice constant. The deformations are scaled by a factor of 15 and added to the undeformed geometry. From the history of the deformation, the contributions of individual slip systems are calculated. (b) and (c) show the contribution of the primary and conjugate slip systems i.e. $(\bar{1}01)[111]$ and $(101)[\bar{1}11]$ respectively. Fig. (d) shows the contribution of the total plastic slip on the anomalous plane $(0\bar{1}1)$ due to glide of dislocations with both $a/2[111]$ and $a/2[\bar{1}11]$ Burgers vectors.
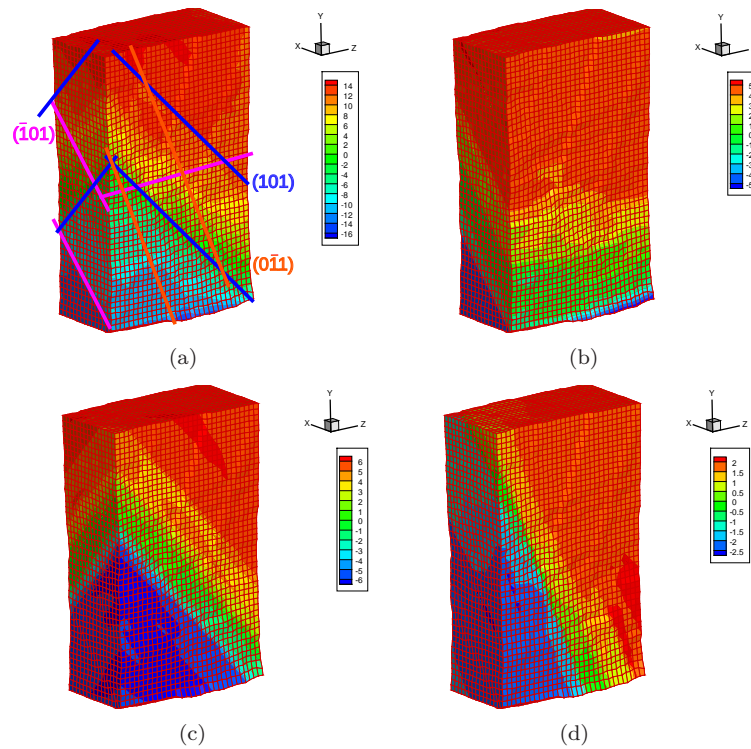
Figure 4.29.: (a) shows for pillar with geometry B the y-component of the total plastic displacement superimposed onto the deformed pillar after a total plastic strain of 0.5% in units of lattice constant. The deformations are scaled by a factor of 15 and added to the undeformed geometry. From the history of the deformation, the contributions of individual slip systems are calculated. (b) and (c) show the contribution of the primary and conjugate slip systems i.e. $(\bar{1}01)[111]$ and $(101)[\bar{1}11]$ respectively. (d) shows the contribution of the total plastic slip on the anomalous plane $(0\bar{1}1)$ due to glide of dislocations with both $a/2[111]$ and $a/2[\bar{1}11]$ Burgers vectors.

5. Discussion

In this chapter, the consequences of the mobility rules developed in chapter 3 on a single screw dislocation and its relation with experiments is discussed. This is followed by a discussion of the mechanism of interaction between repulsively oriented screw dislocations presented in chapter 4. The relevance of these interactions within the context of determining dynamic properties of screw dislocations from *in situ* experiments is discussed. Further, the mechanisms of dislocation multiplication inside micropillars of varying diameters and aspect ratios is discussed. The peculiarities of slip traces on micropillars subjected to uniaxial tension and compression loadings and its relation with experiments is also discussed. The mechanisms which lead to anomalous slip in the simulations on pillars are discussed and compared with other existing models in literature. Finally, the concept of Peierls stress of a screw dislocation is revisited and its relation within the context of both non-Schmid effects and dislocation-dislocation interactions is discussed.

5.1. Finite temperature behavior of an isolated $a/2\langle 111 \rangle$ screw dislocation

5.1.1. Tension-compression asymmetry

Experiments on *bcc* metals like W [42,52], Mo [4,66], Fe [27] and Ta [42,95] have revealed that the yield stress in tension and compression are not the same. This is referred to as the tension-compression asymmetry. It is a clear indication of the violation of Schmid law in *bcc* metals. The tension-compression asymmetry generally increases with decreasing temperature [4].

Initially, tension-compression asymmetry was thought to be a consequence of the twinning-antitwinning asymmetry [4, 52] and therefore a consequence of the sense of shear consistent with tension and compression loading. This would suggest that the tension-compression asymmetry is an effect intrinsic to *bcc* crystals. Seeger [86] assumed that this is because slip occurs on {112} planes which are not mirror planes of the *bcc* structure making the Peierls potential asymmetric on these planes. He also suggested that additional stress-components other than the resolved stress influence the tension-compression asymmetry. Atomistic studies however, reveal that the twinning-antitwinning asymmetry is negligible in W [9, 10]. The tension-compression asymmetry, however, is pronounced as shown in Fig. 4.2. Just as for 0 K [9, 120], at finite temperatures too it can be explained as a direct consequence of the effects of the shear stress perpendicular to the slip direction. In terms of model parameters, tensile loading is characterized by $\eta > 0$ ($\sigma > 0$) and compressive loading by $\eta < 0$ ($\sigma < 0$). In [9, 10] it was shown that the effect of $\sigma > 0$ is to extend the dislocation core on the primary plane and $\sigma < 0$ to constrict it on this plane and extend it on the other two {110} planes of the same zone. This asymmetry induced by the non-glide component of the stress tensor leads to a lower CRSS in tension than in compression. The asymmetry decreases with increasing temperature [4,66]. Hence, the tension-compression asymmetry is not intrinsic to the lattice but an extrinsically induced effect of the applied loading.

5.1.2. Orientation dependence of CRSS

The dependence of the yield stress on the orientation of the applied loading is another characteristic feature of *bcc* metals like W [42,46,49,51,52], Mo [46, 48, 66], Ta [42, 43], Nb [179] and Fe [24, 76, 180]. The CRSS in the mesoscopic model extrapolated to 0 K is consistent with the atomistic simulations [9, 10]. Note that the CRSS obtained from extrapolation is not exactly equal to the atomistic value because the Peierls barrier is obtained from a fitting function to the atomistic values described in [9] which leads to some deviation from the exact values. However, the order of stresses and the trend in CRSS-dependence on orientation is the same as in the atomistic data. Similar to the tension-compression asymmetry, the orientation dependence also has its origin in the dependence of the Peierls

barrier on the non-Schmid components of stress which our model reproduces. This is expected as the model is fitted against the atomistic data at 0 K. As an example, Fig. 4.2(a) and Fig. 4.2(c) show the dependence of CRSS on temperature for different orientations of loading which have the same loading ratio η but different MRSSP angles χ and, consequently, different CRSS in tension. In compression, the difference in CRSS is reduced a little because yielding occurs by dislocation motion on the secondary ($\bar{1}10$) plane for $\chi > 0$ which requires a somewhat lower CRSS.

The orientation dependence of the CRSS reduces considerably with increasing temperature in both tension and compression. At low temperatures, high stresses are applied and the Peierls barrier is strongly deformed. At higher temperatures and lower stresses the Peierls barrier is almost the same for all the glide planes and the energy due to thermal fluctuations plays a greater role. The influence of non-glide stresses therefore vanishes and the dependence of yield stress on orientation disappears.

5.1.3. Temperature dependence of slip plane

With increasing temperatures, experiments in *bcc* metals show coarse crystallographic slip at low temperatures. At higher temperatures, non-planar slip is observed characterized by wavy slip lines on the surface of the sample and therefore it is called as wavy or irrational slip [4]. To account for the experimentally observed wavy slip, the approach here is to show that it is a natural consequence of the competition of at least two {110} slip planes and that it may occur naturally if the non-Schmid stresses are properly taken into consideration.

The average glide plane angle $\overline{\psi}$ displayed in Fig. 4.3 is computed for different orientations at various temperatures in order to determine the slip trace in tension and compression using Eq. (3.19). $\overline{\psi}$ is a measure of the amount of deviation of the actual slip plane from the most highly stressed ($\bar{1}01$) plane. For any orientation in the stereographic triangle shown in Fig. 4.1, σ is always positive on the MRSSP ($\bar{1}01$) in tension and negative in compression. Since in our model, {110} are the elementary slip planes, the contribution of slip from planes other than the highest stressed plane depends on the effect of loading on these planes. A positive σ means a decrease in energy barrier (because of an extension of the core making

it more glissile) on the most highly stressed {110} plane. The effective glide plane then depends on the interplay between σ, χ and η and their effect on the Peierls barrier on all three {110} planes. To understand the effect of these components in detail, the twinning and antitwinning cases must be considered separately for tension and compression.

In tension, the simulation results in Fig. 4.3 clearly show that the slip plane angle $|\overline{\psi}| \leq \chi$ in the entire temperature range displaying $(\bar{1}01)$ slip at low temperatures and slip on the MRSSP at higher temperatures. For loading in tension along any stress axis in the stereographic triangle considered, the $(\bar{1}01)$ plane has the highest resolved shear stress and the lowest activation enthalpy. Therefore this plane contributes the most to the velocity Eq. (3.18). To activate a secondary plane, the combined effect of loading and thermal activation must be sufficient to overcome the barrier on the corresponding plane. For low $|\chi|$, the glide stress component on the secondary plane is not sufficient to overcome the Peierls barrier and hence $\overline{\psi} \approx 0$ for a large range of temperatures. With increasing χ, the resolved shear stress on secondary planes increases, leading to a higher probability of kink-pair nucleation and thus more plastic slip on the secondary plane. Hence in qualitative agreement with experimental observations [4], $\overline{\psi}$ deviates increasingly away from zero towards χ.

For compressive loading corresponding to $\sigma < 0$, the Peierls barrier is always increased on the primary $(\bar{1}01)$ plane compared to the undeformed Peierls barrier. In general, the dislocation has a higher activation enthalpy on the primary plane irrespective of the orientation of the MRSSP. The $\overline{\psi} - T$ dependencies in Fig. 4.3 for loading orientations in the magenta region in Fig. 4.1 are similar to those in tension. Hence, even though the barrier on the primary plane is increased, the activation of the secondary plane is still more difficult in antitwinning orientations.

For loading in the cyan region (Fig. 4.3 (e-g) on page 61), the dislocation motion occurs on the low-stressed $\psi = +60°$ plane at low temperatures as the activation enthalpy is lowest for this plane. From the point of view of an isolated screw dislocation, the slip on the low stressed plane is unusual since no reference is made to other components of the stress tensor. The unusualness does not exist following the proposed kink pair nucleation energy based model in this work for the screw dislocation mobility in *bcc* metals. The curves in Fig. 4.3 (e)-Fig. 4.3(g) show that in the low

temperature high-stress regime, the activation enthalpy for the cyan region in compression is lowest for slip on the $(\bar{1}10)$ plane. Hence at lower temperatures for these orientations, the dislocation moves entirely on the $(\bar{1}10)$ plane despite the fact that it has a lower Schmid factor than the $(\bar{1}01)$ plane because it is energetically more favorable. The velocity of the screw dislocation is therefore almost exclusively governed by the $\psi = 60°$ plane at very low temperatures.

With increasing temperatures, the primary plane ($\psi = 0°$) contributes more towards the velocity but the $\psi = 60°$ plane is still the dominant plane.

The competing activity on the two planes is illustrated by the following example. The activation enthalpy for motion on the three possible planes for compression loading in the $[\bar{5}\ 9\ 17]$ orientation (c.f. Fig. 4.3 (e)) is shown in Fig. 5.1 in the entire stress range up to the Peierls stress.

For $\tau/C_{44} > 0.02$ which corresponds to high stresses and low temperatures, $\Delta H_{\psi=60°}$ on the $\psi = +60°$ plane $(\bar{1}10)$ is smaller than $\Delta H_{\psi=0°}$ of the highest resolved $\psi = 0°$ $(\bar{1}01)$ plane. With decreasing stresses (and increasing temperatures), the activation enthalpy on the $\psi = 0°$ $(\bar{1}01)$ plane becomes comparable to the $\psi = 60°$ $(\bar{1}10)$ plane and this plane contributes increasingly to the plastic slip. The $\bar{\psi} - T$ plot computed from these activation enthalpies is shown in Fig. 4.3(e). The average slip angle changes from $\bar{\psi} = +60°$ at low temperatures and converges towards $\chi = +8.9°$. This change in activation enthalpy which results in the change in slip plane from high stress (low temperature) region to low stress (high temperature) for a given χ is a signature of the role of the perpendicular shear stress σ. This is a manifestation of the tension-compression asymmetry in addition to the CRSS dependence on the sense of loading.

The occurrence of {110} slip at low temperatures and MRSSP slip with increasing temperatures is consistent with experimental observations in W [42, 52] and several other bcc metals [4, 86]. This trend of slip often observed in experiments at higher temperatures [4] can be explained entirely in terms of slip on the {110} planes. Recent experimental findings on $\alpha-$Fe by Caillard [89] also support the view that dislocation motion
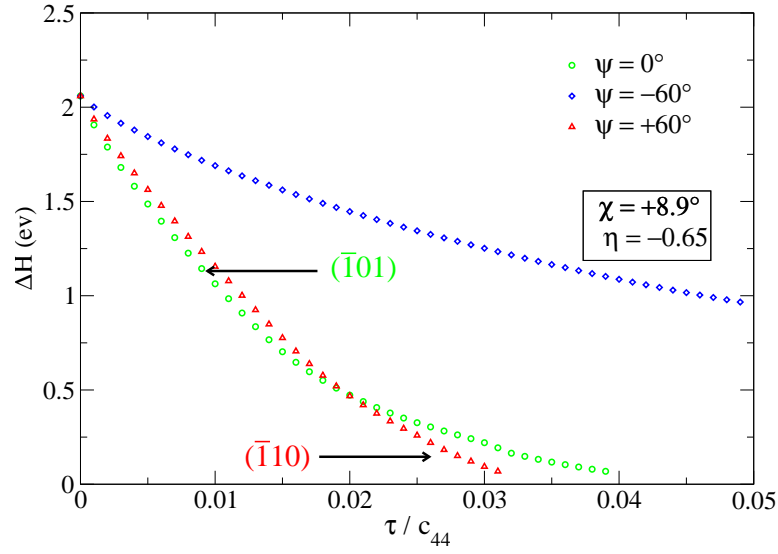
Figure 5.1.: Stress dependence of activation enthalpy for loading in compression along [5̄ 9 17].The loading parameters are given in the insets.

occurs only on {110} planes. It therefore appears not to be necessary to assume that the elementary plane of slip in W and perhaps other *bcc* metals is anything other than the {110} plane.

5.2. Dislocation-Dislocation interactions

5.2.1. Determination of elementary slip planes in *bcc* metals from junction orientations

The settlement of the question of elementary slip planes in *bcc* metals is highly significant for several reasons: 1.) To ensure a sound mechanistic understanding of the fundamental deformation characteristics 2.) For

numerical modeling at the mesoscale and continuum scales where the elementary glide systems must be defined *a priori* and 3.) Mesoscopic screw dislocation parameters like the kink-height can be defined precisely and macroscopic measures like the yield and flow stresses of a metal can be accurately related to the actual microscopic slip planes on which the glide of dislocations occurs. This emphasizes even more the need to settle the long-standing debate of the elementary slip planes.

It must be remarked that the very nature of dislocations is that when they glide on a plane, a clear planar trace on the surface identifiable with a crystallographic plane occurs. Hence, if the screw dislocations glide exclusively on $\{112\}$ plane, the slip traces must be well-defined. However, it is experimentally observed that $\{112\}$ slip traces are always wavy [4, 46, 51, 86], which is inconsistent with the assumption of elementary slip on $\{112\}$ planes. Nevertheless, all methods rely on surface slip traces only and the elementary slip planes in *bcc* metals remains an open question.

Elementary slip plane determination from junction orientations

The ambiguity in determining the elementary slip planes in *bcc* metals has already been discussed in section 2.2.1. In this section, a method is proposed that can be used to unambiguously identify the elementary slip planes from slip activity inside the bulk of the specimen. It is based on dislocation-dislocation interactions and some direct geometric rules imposed by the crystallography of the *bcc* lattice on junction formation. Advantage is taken of the fact that in the high-temperature regime, where there is an ambiguity in the elementary slip plane determination, the edge and mixed dislocations become predominant and the forest intersection occurs. This view is supported by *in situ* experiments which have shown that mixed dislocations play a predominant role in plastic deformation at intermediate temperatures [59, 181–183]. Post-deformation TEM images also show that the microstructure is composed of large densities of mixed dislocations. [47, 53, 184]. For isolated screw dislocations, the simulation results in section 4.1 also show that the non-Schmid effects become less predominant at high temperatures in both temperature and compression. Therefore the most active slip planes can be well described by the Schmid law.

When two $\langle 111 \rangle$ dislocations with distinct Burgers vectors gliding in their corresponding glide planes $\mathbf{n_1}$ and $\mathbf{n_2}$ ($|\mathbf{n}_1 \times \mathbf{n}_2| > 0$) react, locally attractive dislocation segments may form stable junctions with Burgers vector $\langle 100 \rangle$ [185]. The line direction $\boldsymbol{\zeta}_{jn}$ of the junction is given by the Eq. (3.21).

type	$\mathbf{n}_1$	$\mathbf{n}_2$	$\boldsymbol{\zeta}_{jn}$
(a)	$\{110\}$	$\{110\}$	$\langle 111 \rangle$, $\langle 100 \rangle$
(b)	$\{110\}$	$\{112\}$	$\langle 111 \rangle$, $\langle 011 \rangle$, $\langle 113 \rangle$
(c)	$\{110\}$	$\{123\}$	$\langle 111 \rangle$, $\langle 112 \rangle$, $\langle 115 \rangle$, $\langle 133 \rangle$
(d)	$\{112\}$	$\{112\}$	$\langle 111 \rangle$, $\langle 011 \rangle$, $\langle 012 \rangle$, $\langle 135 \rangle$
(e)	$\{112\}$	$\{123\}$	$\langle 111 \rangle$, $\langle 124 \rangle$, $\langle 012 \rangle$, $\langle 135 \rangle$, $\langle 157 \rangle$, $\langle 357 \rangle$, $\langle 5\ 7\ 11 \rangle$
(f)	$\{123\}$	$\{123\}$	$\langle 111 \rangle$, $\langle 012 \rangle$, $\langle 013 \rangle$, $\langle 112 \rangle$, $\langle 133 \rangle$, $\langle 157 \rangle$, $\langle 1\ 5\ 13 \rangle$, $\langle 1\ 7\ 11 \rangle$, $\langle 245 \rangle$, $\langle 359 \rangle$, $\langle 5\ 7\ 11 \rangle$

Table 5.1.: Possible families of directions of junctions $\boldsymbol{\zeta}_{jn}$ in *bcc* metals assuming elementary slip of a/2$\langle 111 \rangle$ dislocations on $\{110\}$,$\{112\}$ and $\{123\}$ planes.

Table 5.1 shows a list of possible families of line directions $\boldsymbol{\zeta}_{jn}$ of $\langle 100 \rangle$ due to dislocation glide on planes with normals $\mathbf{n}_1$ $\mathbf{n}_2$ respectively. The line directions $\boldsymbol{\zeta}_{jn}$ are given in integer vectors with unnormalized lengths. In scenario (a), where the elementary glide planes of both the $\langle 111 \rangle$ dislocations is a $\{110\}$ plane, $\langle 100 \rangle$ junctions can occur only along a $\langle 111 \rangle$ or $\langle 100 \rangle$ direction. In all other scenarios, where either of $\mathbf{n}_1$ or $\mathbf{n}_2$ or both belong to $\{112\}$ or $\{123\}$ families of glide planes, additional line directions of junctions are possible. This is a unique signature of glide on the higher index planes because $\langle 100 \rangle$ junction directions can occur due to glide of reactant dislocations on $\{110\}$ planes alone. Therefore, once the line direction of a junction is known, the Miller indices $\{hkl\}$ of the planes on which the reactant dislocations moved before forming a junction can be retraced and the occurrence of glide on planes other than $\{110\}$ can be established.

It directly follows that it is only necessary to show the existence of $\langle 100 \rangle$ junctions along any direction other than the $\langle 111 \rangle$ and $\langle 100 \rangle$ to demonstrate that elementary slip occurs on planes other than $\{110\}$.

No.	$\mathbf{n}_1$	$\mathbf{n}_2$	$\boldsymbol{\zeta}_{jn}$	f
(1)	[$\bar{1}$01]	[101]	[010]	0.74
(2)	[$\bar{1}$01]	[1$\bar{1}$2]	[131]	0.76
(3)	[$\bar{2}$11]	[101]	[13$\bar{1}$]	0.68
(4)	[$\bar{2}$11]	[1$\bar{1}$2]	[351]	0.70
(5)	[11$\bar{2}$]	[1$\bar{1}$2]	[0$\bar{2}\bar{1}$]	0.8
(6)	[$\bar{2}$11]	[211]	[01$\bar{1}$]	0.67
(7)	[$\bar{1}$01]	[12$\bar{1}$]	[$\bar{1}$0$\bar{1}$]	0.63
(8)	[1$\bar{2}$1]	[1$\bar{1}$2]	[$\bar{3}\bar{1}$1]	0.56

Table 5.2.: Possible line direction of a[100] junction due to interaction of dislocations with a/2[111] and a/2[$\bar{1}$11] Burgers vector assuming elementary slip on {110} and {112} planes only. [$\bar{1}\bar{1}$2] and [101] is equivalent to (2); [$\bar{1}$01] and [211]; [$\bar{2}$11] and [101]; [$\bar{2}$11] and [110] interactions equivalent to (3);[$\bar{1}\bar{1}$2] and [211] equivalent to (4); [1$\bar{2}$1] and [101]; [11$\bar{2}$] and [110] equivalent to (7); [11$\bar{2}$] and [12$\bar{1}$] equivalent to (8). System (6) is glissile and all others are sessile.

Eq. (3.22) gives the condition for the stability of junction [186, 187]. In this equation, the energies per unit length E of a dislocation line for the isotropic elastic case is given by Eq. (3.22). We define a factor f as the ratio $E_3/(E_1 + E_2)$ where E_1/L, E_2/L and E_3/L are the energies (per unit length) of dislocation and Burgers vectors $\mathbf{b}_1$, $\mathbf{b}_2$ and $\mathbf{b}_3$ are $a/2[111]$, $a/2[\bar{1}11]$ and a $\langle 100 \rangle$ respectively given by the Eq. (3.22). Values of fraction $f < 1$ indicates that the formation of junction leads to lowering of energy and indicates a stable junction. All the junctions listed in the table 5.2 are stable and lead to a lowering of energy.

System (1) in table 5.2, results from dislocations lying only on {110} systems alone. Each of the other line directions can only occur if a higher index plane is involved. The system (6) with $\boldsymbol{\zeta}_{jn} = (0\bar{1}1)$ and $\mathbf{b}_{jn} = [100]$ is glissile on the (011) plane whereas none of the reactant dislocations lie on this plane. System (8) results from interaction between [1$\bar{2}$1][111] and [1$\bar{1}$2][$\bar{1}$11] and has the lowest f for junction along the [$\bar{3}\bar{1}$1] direction. It must be emphasized that demonstrating the occurrence of even a single junction directions such as a {311} is sufficient to prove the occurrence of elementary slip on {112} planes.

For other orientations, the corresponding plane with highest Schmid factor is shown in Fig. 5.2. Corner orientations [011] or [001] may be more
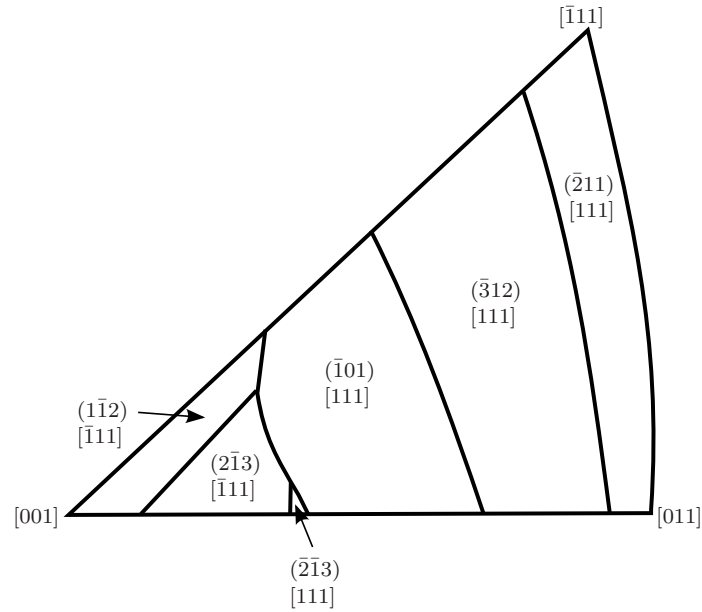
Figure 5.2.: For the stereographic triangle, the planes with highest Schmid factors are shown assuming {110}, {112} and {123} elementary slip planes only (adapted from [188]). This clearly shows that ($\bar{1}$01)[111] system has the highest Schmid factor in only a small region.

suitable for the determination of glide planes. This is because for such orientations, the Schmid factors of the {112} planes are higher than that of {110} planes. Hence if the {112} are indeed elementary planes of slip, the probability of dislocation interactions and junction formation involving these planes is the highest for this loading direction. This also increases the probability of finding junctions with orientations not possible via {110} interactions.

Transmission electron microscopy (TEM) from different angles or TEM tomography are probably best suited to experimentally determine the orientations of junctions. However, they have a limited spatial resolution. To ensure uniqueness of the determination of the junction directions, it is

therefore necessary to ascertain that the junction orientations can be resolved. The angles between all junction orientations resulting from elementary slip on {112} planes with the nearest ⟨111⟩ or ⟨100⟩ directions of the junctions formed by {110} slip turns out to be always larger than 19.5°. This relatively large orientation difference should make it straight forward to identify such junctions if they exist.

In the *bcc* crystallography, there are in total 1716 possible sessile reactions [189] when one considers the {110}, {112} and {123} families of planes as elementary slip planes. Only 96 occur due to reactions between {110} planes only. So far in experiments only the ⟨100⟩ screw orientations have been reported in $\alpha-$Fe [190] and edge, screw and mixed ⟨111⟩ orientation have been reported in Mo [47,191]. The sessile edge orientation can only result from glide on {110} planes only and the occurrence of a large density of such junctions is a strong indication for elementary slip on {110} planes only. So one can conclude at this point that all the evidence from junctions in bcc metals available to date is only compatible with elementary slip on {110} planes.

In summary, a method is proposed that can be used to unambiguously determine whether or not {112} or {123} slip planes are indeed the elementary planes of slip in *bcc* metals based on the formation of {100} junctions. The use of line direction of junctions to identify elementary slip planes has not yet been considered. The proposed method is applicable to all metals in which an open question remains as to which slip systems are active and can be used to settle the fundamental question of elementary glide planes. A thorough characterization of the line direction of the a ⟨100⟩ junctions in *bcc* metals can thus provide an information on the local history of the glide of the reactant dislocations.

5.2.2. FR sources

In the simulations, the different operation of a single FR source in tension and compression shows the importance of including the non-Schmid behavior (see section 4.3). In tension, the approaching dipoles prior to annihilation move faster towards each other. The local stress field and the local MRSSP of the dislocation varies with the distance between the dipoles. For any orientation the local MRSSP is different from the MRSSP due to

the macroscopic loading. The degree of variation in the local parameters with respect to the macroscopic value is a function of temperature and dislocation microstructure. Hence in general, the local stress state governing the screw dislocation activation is different from the macroscopic state. Since this may lead to screw dislocations leaving the primary plane of the initial FR source it means that the initial FR sources are less important as specific characteristics of the dislocation structure in bcc-metals compared to *fcc* and may even be indistinguishable from single-armed sources in many cases.

Recently, Wang et al. [157] used a different approach to incorporate non-Schmid effects in a DD model. Their approach utilizes slip on both the {110} and {112} planes in order to capture the orientation dependence and the tension-compression asymmetry in Ta. Different Peierls stresses for screw and edge dislocations on each of these planes are used along with a modified expression for an "effective Peach-Koehler force" that includes the non-glide components of stresses to capture the non-Schmid effects. The stresses normal to the Burgers vector are used to affect the Peierls stress on the {112} planes only. The Peierls stress values for screw dislocations in their model are taken from experiments. The different response of the FR source in tension and compression as we have shown, cannot be captured with such a description. From a computational point of view, evolution of dislocations on slip planes other than {110} must be taken into account which increases the total computational cost.

5.2.3. Mechanism of repulsive interaction between screw dislocations

In this section, the mechanistic details of the repulsive interaction between non-coplanar a/2⟨111⟩ screw dislocations investigated in section 4.4 and its relation with *in situ* experiments will be discussed.

Matsui et al. [192] investigated analytically the case of repulsively interacting screw dislocations (Fig. 4.7) using isotropic elastic fields of screw dislocations. The authors proposed a mechanism to explain the occurrence of anomalous slip frequently observed in low temperature experiments on *bcc* metals [4, 94, 135, 193, 194]. This mechanism, shown schematically

in Fig. 5.3, envisages that the mutually repulsive screw dislocations exert torque on each other and mutually bend into a non-screw orientation in a common plane. The two dislocations are then hypothesized to glide co-cooperatively on the common plane via the motion of non-screw segments at much lower-stresses than the Peierls stress of screw dislocations. This common plane is always the anomalous plane and hence it is asserted that the anomalous slip in *bcc* metals can be accounted for. Louchet et al. [195] also investigated experimentally the interactions between repulsive screw dislocations at low temperatures and found that 1.) the screw dislocations behave as rigid lines and never cross each other at low temperatures 2.) the postulated bending of screw dislocations proposed by Matsui et al. [192] and the collective motion of the dislocation on the anomalous plane does not occur.

The simulations performed in this work reveal a different mechanistic picture compared to the hypothesized mechanism of Matsui et al. [192] and shed new light on the nature of interactions in the low temperature regime. The main observations are summarized as follows:

(a) The screw dislocations maintain a constant equilibrium distance from each other. The relative angle between the interacting segments remains constant equal to the angle between the corresponding Burgers vectors.

(b) The strongest interacting regions of the screw dislocations remain straight and glide collectively as rigid lines. They do not locally bend.

(c) The equilibrium distance of approach depends on two factors: the sense of loading and the interacting Burgers vectors because the relative angle between the planes on which each screw dislocation glides is different.

(d) The interactions directly influence the activation enthalpy of the kink-pair nucleation for the screw dislocation. Therefore, the activation enthalpy of kink-pair nucleation varies along the length of the screw dislocation.

To understand the observed behavior, first the relevant stress components on screw dislocations as predicted by isotropic elasticity theory are com-

(a)
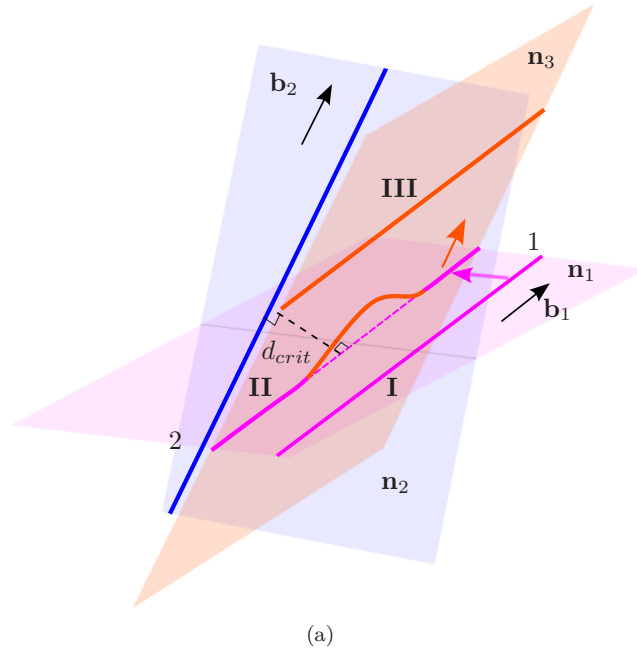
Figure 5.3.: Schematic representation of the mechanism of repulsively interacting screw dislocations hypothesized by Matsui et al. [192]. Planes n_1 and n_2 are the glide planes of dislocations with Burgers vectors b_1 and b_2. n_3 is the plane containing both the Burgers vector directions. Dislocation 1 glides from position **I** to **II** in the direction shown (magenta arrow) where the torque exerted by the mutual stress field is attributed to aid kink-pair generation on the screw dislocation in the common plane with normal n_3. The lateral movement of kinks (shown with half arrows) leads to forward translation of screw dislocation to position **III** on this plane.

pared with those of simulations. For the theoretical part, the formalism of [2, 192] for infinitely long screw dislocations schematically shown in Fig. 5.4 is adopted. The force components F_y and F_z are defined in the local co-ordinate system and are calculated using the equations from reference [192]. Dislocation 1 glides in the xy-plane and 2 glides in a plane at 60° to the xy-plane. The plane common to the two dislocations is the xy-plane. The effect of F_y is to exert a torque on the screw dislocations and

mutually rotate each other out of their glide plane into the xy-plane. The component F_z is repulsive and acts in the glide plane of the two dislocations.
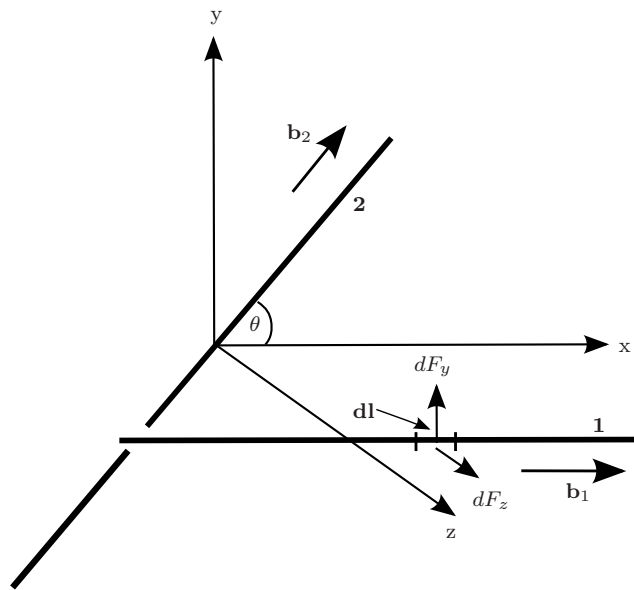
Figure 5.4.: Schematic illustration of two interacting screw dislocations and the force components due to mutual interaction.

Fig. 5.5 shows the variation of the magnitude of resolved shear stress components F_y/b and F_z/b along the screw dislocations for three different values of z. The postulated bending of the screw dislocations in the anomalous plane does not occur because it would first involve a change in glide plane of the dislocations necessitating cross-slip. For cross-slip to occur, the corresponding critical stress for kink-pair nucleation on the cross-slip plane must be exceeded.

The simulation in tension for the $a/2[111]$-$a/2[11\bar{1}]$ interacting system shows that the nearest distance of approach is about 18 b. This distance is far from core-interaction region and governed by the long-range elastic

stress-fields of the dislocations [2]. The maximum value of the repulsive stress at a distance of about 18 b obtained from the simulation is about 1 GPa (Fig. 4.8(a)) which is in good agreement with the value predicted by isotropic elasticity theory (see Fig. 5.5(b)). Correspondingly, the maximum value of the torque component of stress F_y/b at the same distance obtained from the elasticity theory is about 160 MPa (see Fig. 5.5(a)). Therefore, the repulsive stress experienced by both the dislocations is significantly greater than the torque component. Additionally, the torque component of stress combined with the external applied stress on the common plane is also insufficient to cause a local bend on the screw dislocation on the common slip plane as hypothesized by Matsui et al. [192].
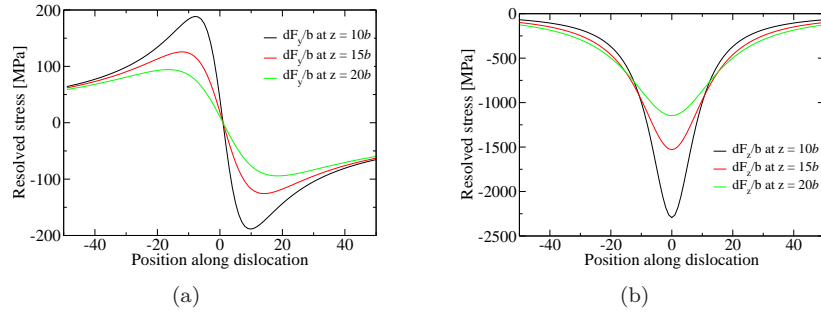
Figure 5.5.: (a) shows the variation of the torque component of the stress along the dislocation line due to interaction between screw dislocations; (b) shows the variation of the repulsive stress force along the length of the screw dislocation. Both the torque and repulsive stress components reach a maximum at the point of nearest approach. Both the stresses are plotted for three different nearest separation distances shown in the insets.

Collective motion of screw dislocations

Next, we consider how the collective motion of the two screw dislocations occurs by analyzing the local parameters controlling the kink-pair nucleation enthalpy for the two dislocation system discussed above. The discussion is equally valid for the a/2[111] and a/2[$\bar{1}$11] screw dislocation system.

To recall, the simulation shows that in tension, the CRSS of screw dislocation 1 is reached first and it approaches the other in-active dislocation 2. At an equilibrium distance of about $18 - 20\ b$, the two move co-cooperatively on their respective planes.

Dislocation 1 is activated when the external stress reaches its CRSS and approaches dislocation 2 at an angle corresponding to the angle between Burgers vector directions $(71°)$. The common plane containing both the Burgers vector directions is the $(\bar{1}10)$ plane. The direction of approach of the two dislocations coincides with the normal of this plane i.e. the $[\bar{1}10]$ direction. The variation of the interaction stress on dislocation along its length suggests (see Fig. 5.5(b)) it has a stress-concentration at a point corresponding to the nearest distance of approach. At this point on the corresponding dislocations 1 and 2, the effect of mutual interaction is to oppose and aid respectively the effect of the applied stress. Barring a small region on dislocation 1 which opposes the externally applied stress, the stress on 1 is homogeneous equal to its CRSS. The further forward glide of dislocation 1 occurs despite the repulsive effect due to dislocation 2 because the part of the screw dislocation 1 outside the interaction zone still sees stress equivalent to its CRSS.

In order to demonstrate that the stress required to activate screw dislocation 1 remains almost the same throughout the entire simulation, the activation enthalpies at the point of nearest approach and the global minimum activation enthalpy controlling the mobility of both screw dislocations are plotted in Fig. 5.6(a). They are denoted as $\Delta H_n{}^i$, $\Delta H_{min}{}^i$ respectively where the superscript i corresponds to the dislocation 1 and 2. The subscript n stands for ΔH measured at the point of nearest approach which is on the strongest interacting segments of the two dislocations and min stands for the minimum value of activation enthalpy of all the screw segments of dislocation i.

The plot in Fig. 5.6(a) shows that for dislocation 1, the activation enthalpy of the strongest interacting segment is much higher than the minimum along the screw dislocation. This is expected because the repulsive stress due to dislocation 2 acts in the opposite direction to the externally applied stress and thereby lowering the effective resolved shear stress. The plot also shows that the activation enthalpy ΔH of the strongest interacting segment is much higher than the minimum activation enthalpy. The

minimum activation enthalpy of dislocation 1 occurs away from the inter-
acting region is activated when the external stress reaches its CRSS. In
this manner dislocation 1 continues to glide further despite the presence
of the dislocation 2. For dislocation 2, the curves of $\Delta H_n{}^2$, $\Delta H_{min}{}^2$ are
coincident (as expected) confirming that the lowest activation enthalpy
and the enthalpy of nearest approach segment are equal. Therefore the
glide of dislocation 2 occurs at the point of nearest approach where the
effect of interaction is strongest. The same trend is also observed for the
$a/2[111]-a/2[11\bar{1}]$ dislocation system shown in Fig. 5.6(b).

Another aspect of the collective motion of the two dislocations is that
the activation enthalpy of dislocation 2 when it becomes mobile is lower
than that of dislocation 1. This is because the interaction stress influences
the parameters χ and the normal stress σ on the strongest interacting
screw dislocation segments. Therefore the CRSS and the corresponding
activation enthalpy of glide of screw dislocation is also influenced by the
interactions. For the driven dislocation 2, the activation enthalpy ΔH of
the strongest interacting segment is minimum at the point of strongest
interaction. These results clearly illustrate a fundamental aspect of screw
dislocation motion, namely, the activation of a screw dislocation can occur
at stress concentration points.
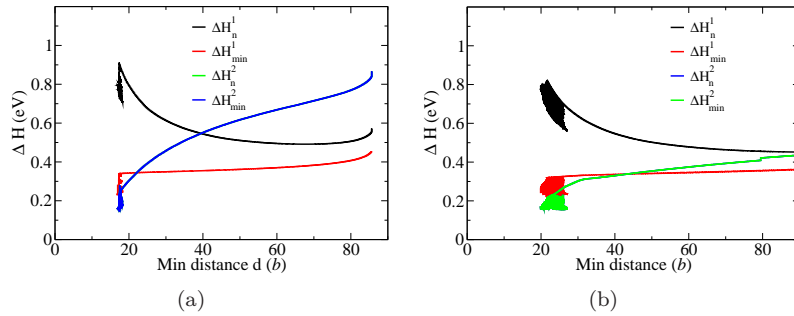
Figure 5.6.: Activation enthalpy minimum vs activation enthalpy at the point of
nearest approach for the (a) $a/2[111]-a/2[11\bar{1}]$ and (b) $a/2[111]-]a/2[\bar{1}11]$ interacting
systems of screw dislocations in tension for loading along the $[\bar{1}\,4\,9]$ direction.

Tension-compression asymmetry in dislocation interactions

The tension-compression asymmetry exhibited by an isolated screw dislocation also affects the mechanism of repulsive interaction between screw dislocations. Firstly, the nearest distance of approach before a secondary screw dislocation 2 may be activated due to interactions in tension and compression depends on the slip systems of the two dislocations. For the $a/2[111] - a/2[11\bar{1}]$ (see section 4.4) interacting dislocation system, the minimum distance of approach at which the screw dislocation 2 is activated is 18 b in tension compared to 14 b in compression. However, for the $a/2[111]-a/2[\bar{1}11]$ dislocation system, the nearest distance of approach is about 75 b compared to 20 b in tension. The larger distance in compression for the $a/2[111]-a/2[\bar{1}11]$ dislocation system can be explained as follows: Due to the macroscopic loading alone, the loading ratio η on the MRSSP of these two slip directions are -0.51 and -0.34 respectively in compression compared to 0.51 and 0.34 in tension. As discussed already for an isolated screw dislocation in section 5.1.1, in compression corresponding to $\sigma < 0$, the CRSS on the corresponding primary planes $(\bar{1}01)$ and (101) of the two screw dislocations is increased compared to the unloaded state. However, due to to larger negative σ on the $(\bar{1}01)[111]$, the CRSS of the higher stressed $(\bar{1}01)$ plane is more than that on the (101) plane. Accordingly, the corresponding activation enthalpy curves for the two slip systems in Fig. 4.21(b) show that in compression the activation enthalpy of the $(101)[\bar{1}11]$ lies below that of the $(\bar{1}01)[111]$. Therefore the activation of a/2$[\bar{1}11]$ screw dislocations due to repulsive interaction with the a/2$[111]$ screw dislocations occurs at lower magnitudes of internal stresses (larger nearest distance of approach) in compression than in tension.

Secondly, the plane on which the screw dislocations move is also influenced by dislocation interactions as shown for the $[11\bar{1}]$ screw dislocation which glides on (011) in tension and (101) in compression even though the MRSSP angle . The change of glide plane of the a/2$[11\bar{1}]$ screw dislocation in compression occurs because the interaction stresses also modify the non-Schmid stress components and lower the CRSS on the (101) plane. The (011) plane is still the highest resolved shear stress plane even after the interactions are taken into account. The change in slip plane is another manifestation of the tension-compression asymmetry. However, the change

in glide plane is a feature sensitive to the potential used to derive the activation enthalpies.

It must be emphasized that the values of the critical distance obtained in the simulation depend obviously on the input values of CRSS of the screw dislocations. However, the general arguments hold for a different magnitude of CRSS of screw dislocation, as long as it is sufficiently large for the screw dislocation to remain rigid. This is because the repulsive force varies much stronger than the component of force that exerts torque on the screw dislocation.

The consequences of interaction between mixed dislocations and screw dislocation will be discussed in section 5.3.5.

Relation with experiments

Recently, *in situ* TEM experiments have been employed to experimentally determine the local CRSS of a screw dislocation and relate it to the macroscopically measured flow-stress [89]. In this respect, the simulation result that a screw dislocation can be activated at stress-concentration point is quite significant. This is because in experimental specimens, such stress-concentrations may also occur at jogs, in the vicinity of point-defects or even at surfaces where the atomistic simulations show that dislocation core structure may be modified [196]. These stress-concentrations may significantly lower the externally applied stress required to move a screw dislocation. Therefore the experimentally measured CRSS may not corresponding to the macroscopic loading state.

Furthermore, the barrier for kink-pair nucleation and hence the CRSS of a screw dislocation depends on its vicinity. Hence the use of TEM to infer the kinetics of individual screw dislocations at low temperatures, where the observed motion of isolated screw dislocations is attributed to a homogeneous stress-state along screw dislocation is questionable [89].

The simulation result that the repulsively interacting screw dislocations never cross each other is significant in interpreting the dislocations which are active during deformation in experiments. This is because typical microstructures observed in specimens after deformation at low temperatures are highly jogged [44, 47, 53, 193, 197, 198]. Takeuchi [26] attributed

the repulsive cutting of two screw dislocations to be fundamental mechanism responsible for the multiplication and work-hardening behavior in Fe. Lawley et al. [44] explain the occurrence of jogs on screw dislocations due to cutting of screw dislocation through other screw dislocation forest in *bcc* metals. These two conclusions are therefore in contradiction with the results of simulation on repulsively interacting screw dislocations. However, in the simulations, mixed dislocations are observed to easily cut through screw dislocations which would create jogs. Therefore, the high density of jogs during deformation in experiments implies that significant deformation in *bcc* metals must also occur due to mixed dislocation motion even at low temperatures. This also indicates that mixed dislocations would also contribute significantly to the overall deformation in *bcc* metals even at low temperatures where the flow-stress is classically related to screw dislocation motion only [199].

Comparison with dislocation interactions in *fcc* metals

A similar case of initially straight interacting dislocations was examined by [150] for *fcc* metals with the aim of understanding the mechanism of their interaction. A map of the outcome of approaching dislocations at arbitrary angles for the *fcc* structure provided in [187, 200, 201] shows that in *fcc* metals a different and more complicated picture emerges. The actual final configuration depends on the relative angle of approach and the habit plane of the two strongly interacting segments of the dislocation. At the point of nearest approach, the effect of torque is dominant and can cause a local realignment of these segments. In fact even if the dislocations are initially repulsive, interaction may lead to a local realignment resulting in mutually attractive configuration leading to junction formation [202] and therefore more hardening. The same arguments hold for screw dislocations in *fcc* metals.

In comparison, the simulations show that in W (and perhaps other *bcc* metals) the screw dislocation remains rigid and can be activated at any point along its line by mixed or other screw dislocations. In the forest-hardening picture therefore, in *bcc* metals, the forest screw dislocations are not strong barriers to deformation. This could possibly explain why *bcc* metals in principle show lower work-hardening rates compared to the *fcc* metals [4].

### 5.2.4. Multiplication mechanisms in pillar with two initial FR sources

The stress strain curve (Fig. 4.13(a)) of the pillar with two initial FR sources with Burgers vectors a/2[111] and a/2[1$\bar{1}$1] (section 4.6) upon loading shows a surprising drop in effective stress by about 1.4 GPa after the yield point is reached. A large increase in dislocation density of mixed dislocations with a/2[111] Burgers vector is generated (see Fig. 4.14) which populates the specimen. The increase in dislocation density occurs due to self-multiplication of dislocations with a/2[111] Burgers vector. Both the drop in flow-stress and generation of a large density of mixed dislocations due to self-multiplication is unexpected because firstly, screw dislocations owing to their larger CRSS are expected to govern the plastic flow and secondly, mixed dislocations have very low CRSS compared to the CRSS of screw dislocations and accordingly expected to leave the volume leaving the pillar with less mobile screw dislocations which would then move at the corresponding CRSS. The mechanisms responsible for the sustained self-multiplication of mixed dislocations and the generation of new screw dislocations and their role in promoting self-multiplication are discussed in the next section.

Multiplication and storage mechanisms of mixed dislocations

The key to the multiplication and storage of mixed dislocations inside the volume is the presence of kinks/jogs and generation of kink-complexes which consist of non-screw dislocations connected over several planes.

The kinks/jogs on screw dislocations act as pinning points to the forward motion of the screw dislocation but they can glide along the screw direction. Fig. 5.7 is a schematic representation of the change in dynamics of screw dislocation due to presence of pinning points such as jogs/kinks on the dislocation line. An initial screw dislocation S in Fig. 5.7(a) upon cross-slip in Fig. 5.7(b) has two segments S$_1$ and S$_2$ over two parallel planes connected by a kink AB which can in principle glide along the Burgers vector direction. However, if the screw arms are activated, then it is accompanied by the generation of mixed dislocations such as AC and BD on parallel planes around the pinning point. If the lengths of the

mixed segments AC and BD is equal, a dipole may result. However, in general, the screw arms S_2 may get activated more than the arm S_1 which effectively increases the length of the mixed part connected to S_2 as shown in Fig. 5.7(c). Further loading results in the evolution of the loops which bypass each other on parallel planes as shown in Fig. 5.7(d). Planar mixed dislocations of the same Burgers vector which glide on a single plane can only intersect other planar dislocations if they line on the same plane.
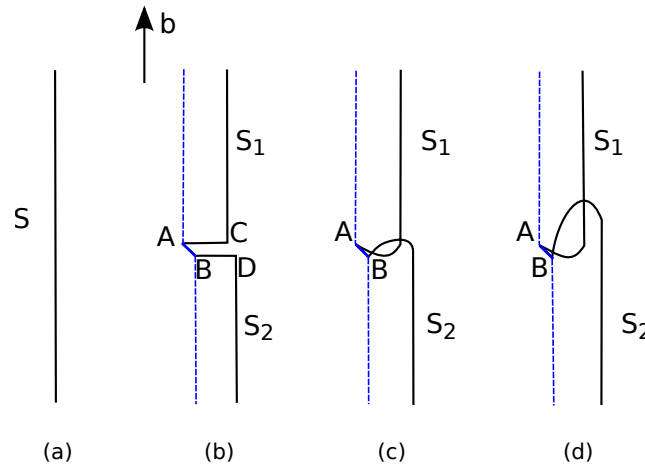
Figure 5.7.: Fig. shows schematically the kinks on screw dislocations generated due to cross-slip alters the dynamics of a screw dislocation. The effective length of (a) an initial screw dislocation changes in (b) due to cross-slip. Further evolution results in the generation and bypassing of the mixed dislocations.

Fig. 5.8 shows a snap-shot from the simulation in which a sequence of events leading to the formation of kink-complex is shown. The fundamental mechanism leading to formation of such complex is cross-slip. The kink-complex M^* in Fig. 5.19(b) is generated due to the interaction between the mobile $a/2[111]$ screw dislocation pinned at P_1 and the immobile arm of the source pinned at P_3 with $a/2[\bar{1}11]$ Burgers vector which introduces a stress-inhomogeneity. Successive cross-slip on the mobile screw dislocation and the accumulation of kinks leads to the generation of kink-

complex which get activated when the effective mixed orientation reaches a critical configuration.

Self-multiplication of dislocations is aided due to the ease of generation of kink-complexes on a screw dislocation around pinning points such as immobile junctions or kinks gliding on other planes. This is because due to the non-planar character of the kink-complex increases their probability of interaction and multiplication with other mixed dislocations of the same Burgers vector increases. Long dislocation loops as observed in the simulation (see Fig. 4.14) are a result of the interaction of loops with kink-complexes. The mechanism of formation of such loops is shown schematically in Fig. 5.9. Two single armed sources S_1 and S_2 get activated and typically the evolution of screw arms S_1 and S_2 is accompanied by generation of kink-complexes such as M_1 and M_2. They move in opposite directions r_1 and r_2 and are therefore attractive. Their intersection results in an exchange of arms and generation of new loops as shown in Fig. 5.9(c). In the simulation, several kink-complexes are generated because as a screw dislocation moves through the volume, it experiences stress variation along its length due to the presence of other dislocations. Therefore, self-multiplication sets in when such configurations generated elsewhere in the volume and moving in opposite directions intersect. Plastic flow occurs by the glide of such mixed loops and which continuously exchange arms as shown in Fig. 5.9(c).

Dragging of kinks and generation of screw dislocations

The main mechanism for generation of new screw dislocations at lower-effective stresses compared to the CRSS of screw dislocations is the dragging of the end nodes of edge-segments which act as pinning points on screw dislocations. The screw dislocations are crucial to the generation of new dislocations because they can cross-slip easily due to interactions with mixed dislocations and produce new kink-complexes. Fig. 5.10 shows a snap-shot from the simulation illustrating the generation of new screw dislocations due to dragging of kinks.

Fig. 5.10 (a) shows the cusps at **C** with a/2[111] Burgers vector (circled and redrawn in the inset). The cusp evolves into mixed dislocation loops which glide in directions $\mathbf{r}_1$, $\mathbf{r}_2$ and $\mathbf{r}_3$ respectively. Insets (A) and (B)
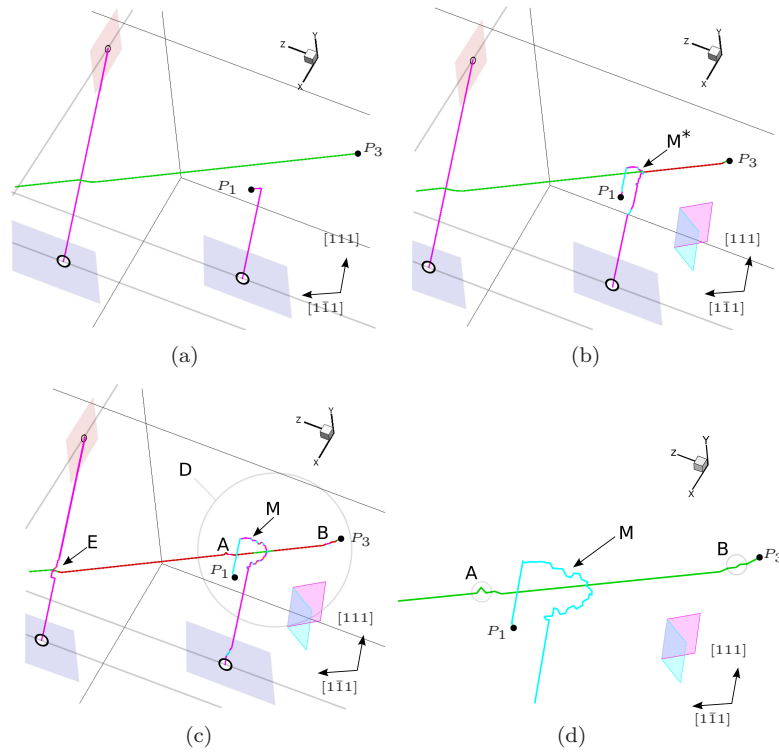
Figure 5.8.: (a) shows the activation of the single armed source with a/2[111] Burgers vector. In (b), the local stress field of a/2[1$\bar{1}$1] causes cross-slip on the screw arm of the a/2[111] dislocations giving rise to a series of kinks on the [111] dislocation (denoted by M^*). (c) further cross-slip events result in new dislocation density on previously unoccupied planes. (d) shows only the dislocation segments in region D in figure (c) zoomed and colored according to their Burgers vector to obtain an experimentalists view of the dislocation configuration. The circles at A and B indicating the irregular appearing segments with sharp corners. These occur as a result of short cross-kinks which mutually pin and oppose each others motion on their respective planes. Note that both dislocations are now spread over multiple planes and connected via kinks. The colored rectangular surfaces with open circles show the local crystal surface. The orientation of the local glide planes is also shown. The color scheme is described in appendix C.
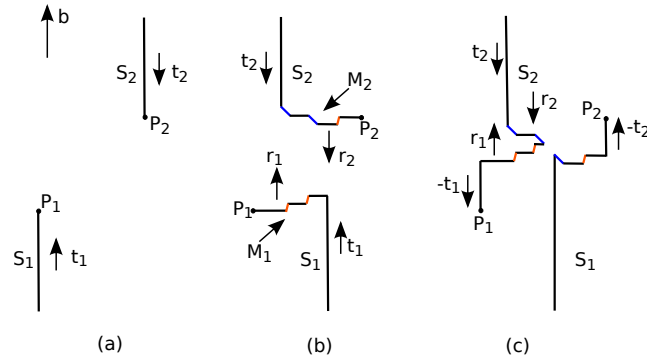
Figure 5.9.: Schematic representation of the effect of kink-complex on the multiplication of dislocations. Two non-coplanar single-armed sources S_1 and S_2 in screw orientation pinned at P_1 and P_2 with opposite line orientations $\mathbf{t}_1$ and $\mathbf{t}_2$.
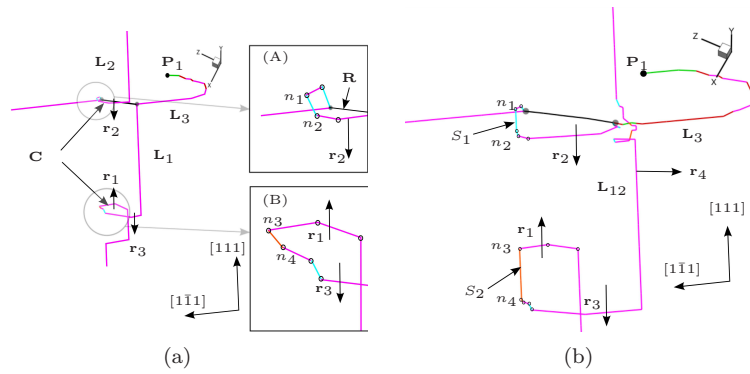
Figure 5.10.: A snap-shot from the simulation showing the mechanism by which new screw dislocations are generated due to dragging of kinks (see text for description). The dislocation lines are colored according to their habit planes and the color scheme is described in appendix C.

show a zoom of the corresponding circled regions. In the inset (A), one end of the mixed part is connected to the in-plane reaction $\mathbf{R}$ and is therefore immobile. The open-circles on the dislocation lines in both the

insets indicate nodes of a dislocation segment. Only nodes n_1 to n_4 which get dragged are shown for clarity. The surrounding complex arrangement of dislocation segments around nodal pairs n_1,n_2 and n_3,n_4 respectively causes them to glide in opposite directions. In Fig. 5.10(b), the nodes at n_1, n_2 and n_3, n_4 respectively are dragged in opposite directions generates screw segments S_1 and S_2. The mixed parts continue to move in the directions $\mathbf{r}_1$ and $\mathbf{r}_2$ respectively and due to their three dimensional nature, their motion is non-planar. Also note that cross-slip results in combination of loops L_1 and L_2 combine to form a longer arm L_{12}. The mixed part of the loop L_2 is pinched off field of the screw part with the two end points at the junction R. Rather than by-passing each other on parallel planes, they intersect each other and act as sources for further dislocation multiplication and dragging. Note that local interactions also cause a change in the glide plane of L_3 with a/2[$1\bar{1}1$] Burgers vector and the accumulation of kinks around the pinning point P_3 which gives it a very non-smooth appearance.

The DDD simulations of Rhee et al. [203] show that an initially jogged single screw dislocation subjected to loading can self-multiply generating a large dislocation density. However, the origin of formation of jogs and the consequence of such large multiplication rate with respect to the overall plastic response in *bcc* metals has not been discussed. Further, in both MD [204] and DDD simulations [112], cusp formation and self-multiplication of screw dislocations has been observed leading to generation of further screw dislocations and is thought to promote strain hardening in *bcc* metals. The cusp formation in their simulations is however attributed to kink-formation by the image forces on different planes at both ends of an initially straight screw dislocation line and their subsequent migration inwards leading to formation of cross-kinks. The simulations performed in this work show that the cross-slip on a screw dislocation due to interactions with other dislocations plays a very important role in the formation of kinks/jogs which act as pinning points on screw dislocation. They promote cusp formation and generation of kink-complex but contrary to the observations of Weinberger et al. [204] no strain hardening is observed. This may be due to the small size of the pillars (48 nm) used in their work where the mixed dislocations escape the sample easily. For the 1 μm pillar used in the present simulation, the mixed loops which

evolve from cusps multiply easily and since they move at lower CRSS compared to CRSS of screw dislocation, softening is observed.

The theories of plastic deformation of *bcc* metals interpret the mechanical properties such as yield and flow-stress in terms of thermally activated glide of single screw dislocations [4, 8]. However, the simulation results show that the presence of jogs aids in the of generation of mixed dislocations which residence longer in the specimen and contribute significantly to the flow-stress. Hence in bulk-specimens where a large density of kinks/jogs on screw dislocations are already present in annealed specimens [99], mixed dislocations are also expected to play a significant role in the overall deformation behavior.

Relation with experiments

Even though the initial configuration is an artificial one, some important features of the simulation can be used to explain experimental observations.

1. Localized wavy slip traces on surface of bulk specimens is a characteristic feature of both low temperatures and high-temperatures deformation in several *bcc* metals (see for example Nb [193], W and Mo [46] and $\alpha-$Fe [89]. Such wavy slip traces can be naturally accounted for in simulations by the glide of the kink-complex such as **M** in Fig. 5.8(d). These are formed due to successive cross-slip on a screw dislocation and accumulation of kinks around a pinning point and then their subsequent activation when the entire configuration reaches a critical radius.

2. The sharp changes in the direction of dislocation segments often observed in experiments [178, 193] which is also a common feature in simulation (see figure 4.14) can be attributed to cross-slip on a screw dislocation and subsequent pinning of the kink at pinning points.

The microstructure in the simulation also shows a striking resemblance to those obtained in experiments and shown in Fig. 5.11. In the experiment, the pinning effect on screw dislocations may be due to the presence

of alloy atoms. Despite the difference in origin of the pinning points between experiments and the simulations, the similarity of dislocation loops indicates a similar mechanistic origin of such structures i.e. presence of obstacles such as jogs on screw dislocations.

5.3. Deformation of pillars in tension and compression

5.3.1. Stress-strain curves and dislocation density evolution in pillars

The stress-strain curves in load-controlled experiments on *bcc* metal pillars [105, 108, 205] are typically characterized by an initial elastic region and a plastic region composed of discrete strain bursts. However, in all the simulations on micropillars with different aspect ratios presented in section 4.7, the stress-strain curves show an elastic region followed by a large softening. For the $[\bar{1}\,4\,9]$ orientation, Fig. 4.22(a) shows that the flow stress drops by about 2 GPa in tension and at least 4 GPa in compression compared to the initial yield stress corresponding to CRSS of screw dislocation. However, the flow stress magnitudes in simulations on pillars in compression post softening of about 4 GPa are in agreement with the flow stresses measured in the experiments at room temperature by Schneider et al. [108] on W micropillars (3-4 GPa) with similar diameters.

The difference in the stress-strain response between experiments and simulation could be because in the experimental specimens, the initial microstructure already consists of a network of dislocations [99]. The initial configuration in the simulation however, is an assumed one consisting of randomly distributed FR sources. Before the yield point is reached, only pure screw dislocations are generated after the mixed dislocations have exited the volume. Once the screw dislocations begin to move, jog formation occurs easily due to cross-slip. The same mechanisms operating in a pillar with two initial FR sources described in section 5.2.4, which aid in the further generation of mixed dislocations and formation of kink-complex such as M in Fig. 4.19 are also active in the pillars with randomly distributed FR sources. Therefore, after yielding, the mixed dislocations which move
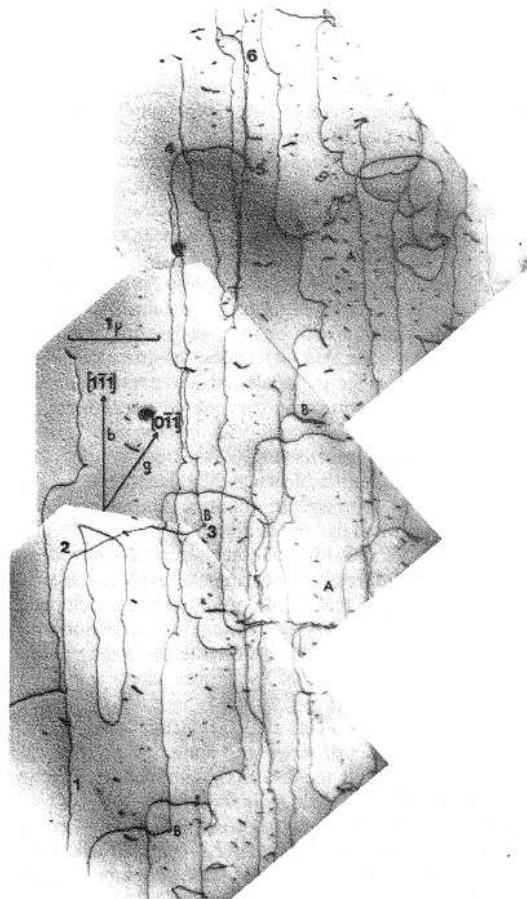
Figure 5.11.: Dislocation loops evolving in crystal of Nb-16 at. pct Mo at 295 K reproduced from reference [4] (with permission). Note the resemblance of the loops to that observed in the simulation shown in Fig. 4.14 showing that similarities in the general nature of dislocation loops.

at much lower stresses than the CRSS of screw dislocations govern the plastic flow in the pillars, which leads to the softening response observed in the simulations.

From the studies on pillars, several other recent experimental observations can be rationalized as described below.

The stress-strain response observed in our simulations is similar to the response of the micropillar experiments on directionally solidified Mo alloy micropillars conducted by Bei et al. [110]. The pillars showed a large elastic region followed by displacement bursts leading to catastrophic and unstable pillar deformation independent of the diameter of the pillar. The experimental samples were almost dislocation free and the softening behavior is attributed to intense dislocation multiplication. The simulation of pillar with two initial sources is possibly similar to the pillars of Bei in terms of initial dislocation density. Therefore, similar mechanisms of deformation described in section 5.2.4 could occur in the experiments leading to the observed softening response.

The large activity of mixed dislocation in simulation can also be used to rationalize the strain bursts observed in recent load-controlled experiments *bcc* micropillars [105, 107, 108]. The experiments show that plastic deformation progresses by strain bursts at certain levels of stress. Zaiser et al. [109] show that size distribution of the strain increments corresponding to the bursts in Mo were similar to those in Ni and are independent of the orientation of applied loading. Strain bursts would not be expected from screw dislocations which glide slowly by the kink-pair mechanism. The similarity of distribution of strain increments in *fcc* and *bcc* metals therefore, strongly suggests that even in *bcc* metals mixed dislocations also play a dominant role in the deformation in the pillars. It must also be noted that the simulations are strain controlled whereas the experiments are stress-controlled. The large stress-drop observed in the simulation due to mixed dislocation activity would correspond to a strain-burst in a load-controlled experiment.

The simulation also raises some important questions which have not been addressed so far in the literature. Firstly, the role of jogs on the dynamics of screw dislocation and the flow-stress of *bcc* metals has not been accounted for. The simulations performed in this work, clearly show that the kinks/jogs significantly influence the the dynamics of screw dislocation motion by changing the effective length of a screw dislocation and therefore, its mobility (see Eq. (2.5)). Secondly, the occurrence of kinks/jogs on screw dislocation could alter the core-structure at that point. At this

point, atomistic simulations can clarify the effect of jogs on screw dislocation mobility.

More importantly, the M111 orientation could play a significant role in the deformation of *bcc* metals as suggested by Kang et al. [139]. This is because a lot of repulsive cutting between mixed and screw dislocations is observed in the simulation which in reality would result in a segment each of the dislocation along a line direction corresponding to the Burgers vectors of the other dislocation. The line direction corresponds to the M111 orientation which is another high-Peierls stress orientation in *bcc* crystals [137, 139]. A large number of instances of cutting implies a high density of segments along the M111 orientation is likely produced in experiments. Therefore, the M111 orientation may then indeed govern the macroscopic response of *bcc* metals.

5.3.2. Activity of slip systems

Recent room temperature experiments on W micropillars [105, 106, 108] and other *bcc* metals [107, 206] have been performed on multislip loading orientations. They are concerned mostly with the investigation of size effect. Any direct comparison of the simulation results presented here for the $[\bar{1}\,4\,9]$ orientation with experiments is therefore not possible. However, the atomistic yield criteria of Groeger et al. [9, 10], which does not take into account the interactions for tension, predicts for the $[\bar{1}\,4\,9]$ orientation.

Experiments in several *bcc* metals like Nb [30, 193], W [46], Mo [44, 46, 47, 207], Fe [23, 180], V [93] and Ta [95, 97] show both the $(\bar{1}01)[111]$ primary and significant conjugate $((101)[\bar{1}11])$ slip system activity from the beginning of deformation for center-triangle oriented specimens where one expects single slip only.

Two loading axes of the pillars have been chosen along the $[\bar{1}\,5\,10]$ and the $[\bar{1}\,4\,9]$ direction for the simulations in compression. For the $[\bar{1}\,4\,9]$ orientation, simulations were also performed in tension. These correspond to single slip orientations where the highest resolved shear stress plane $(\bar{1}01)$ is expected to be largely active both from Schmid law and from

atomistic studies on isolated screw dislocation including non-Schmid effects [9,10]. Similar to experiments in bulk-specimens, single slip has not been observed in any simulation.

The slip activity on the $[\bar{1}\,5\,10]$ oriented pillars are in good agreement with the *in situ* Laue in experiments on pillars with same geometry [208]. For the $[\bar{1}\,4\,9]$ oriented pillars, the deformation picture shows the same trend but the activity of conjugate slip system is always higher in compression compared to tension.
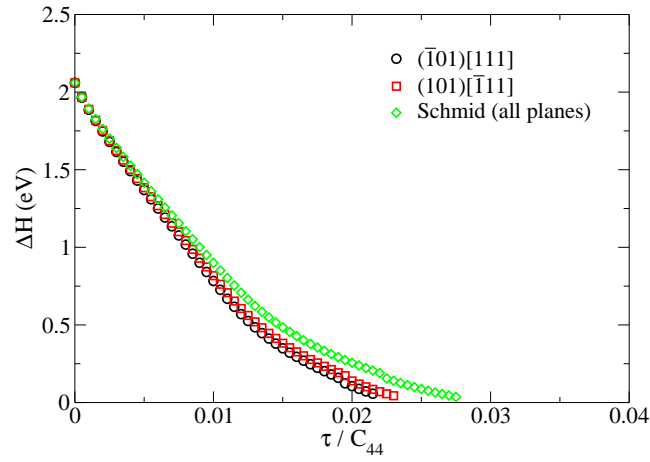
Figure 5.12.: A comparison of the activation enthalpies for the $(\bar{1}01)[111]$ and the $(101)[\bar{1}11]$ incorporating non-Schmid stresses for the $[\bar{1}\,4\,9]$ loading orientation. The plot in green is the activation enthalpy when only Schmid law is considered. In the Schmid law framework, the activation enthalpy of all slip systems is given by one curve.

In tension, the slip activity in pillars with aspect ratio $1:3:1$ shows that at least 30% of plastic slip occurs on the conjugate $(101)[\bar{1}11]$ slip system. This is interesting because the role of non-Schmid stresses in tension is to lower the activation enthalpy of kink-pair nucleation for the $a/2[111]$ screw dislocation on the primary slip system $(\bar{1}01)[111]$ compared to the case when these effects are neglected. This is illustrated in the activation enthalpies of the slip systems shown in Fig. 5.12. Therefore, the

primary slip system $(\bar{1}01)[111]$ is expected to dominate the slip activity even more when the non-Schmid effects are taken into account.

The occurrence of large amount of slip on the lower stressed conjugate slip system $(101)[\bar{1}11]$ in both tension and compression can be rationalized as occurring due to the relative orientation of the $a/2[111]$ and $a/2[\bar{1}11]$ Burgers vectors. This geometric feature determines the longest length of the screw dislocations spanning the volume of the pillar. The effect of high Peierls stress is that the forest screw dislocations remain straight and span the volume. For the different aspect ratio of the pillars chosen in the simulations, the screw dislocation with $a/2[\bar{1}11]$ (conjugate) Burgers vector is the longest. The mobility law for screw dislocation clearly implies that a longer dislocation has more number of kink-nucleation sites along its length ($\frac{L}{l_c}$) and hence a higher probability of activation. Therefore, the screw dislocation with $a/2[\bar{1}11]$ Burgers vector has on an average the largest probability of being activated due to interactions with other active slip systems. The other active dislocations could be either screw dislocations gliding on primary slip plane $(\bar{1}01)$ or even mixed dislocations gliding on low stressed planes. In the simulations, the screw dislocations with $a/2[\bar{1}11]$ Burgers vector move on the (101) plane and are activated primarily due to interactions and contribute to slip, even though the macroscopic stress state favors the $(\bar{1}01)[111]$ slip system.

Additionally, in compression for the $[\bar{1}\ 4\ 9]$ loading orientation, the contribution of the conjugate slip system $(101)[\bar{1}11]$ (39%) to total slip is even higher than that of the primary slip system $(\bar{1}01)[111]$ (32%). This is because in compression the $(101)[\bar{1}11]$ slip system has a lower CRSS than the $(\bar{1}01)[111]$ slip system due to the effect of non-Schmid stresses and can be activated at lower internal stresses than in tension (see section 5.2.3). Therefore, due to the effect of dislocation interactions, the conjugate slip system $(101)[\bar{1}11]$ contributes more to the total slip than the primary slip system $(\bar{1}01)[111]$.

### 5.3.3. Influence of surface orientation on slip geometry

Vesely [100, 101, 209] performed tensile experiments on thin foils of Mo at room temperature with center-triangle orientation to investigate the influence of surface orientation on the slip system activity. The geometry of the

foils used in the experiments of Vesely had similar geometries *A* and *B* (see Fig. 4.26). The main experimental findings of Vesely were that for orientations A and B the most active Burgers vectors were the a/2[111] and the a/2[$\bar{1}$11] (see Fig. 4.26) respectively. Additionally, slip on other low stressed slip systems was also observed for both the orientations. Experimental investigations by Matsui et al. [210] on Mo also showed that the most active Burgers vector depended on the orientation of the foil. More recently Kaufmann et al. [211] also investigated the effects of geometry on the flow- stress of Ta and Fe micropillars at room temperature. They showed that the flow-stress depends on the orientation of the primary Burgers vector with respect to the largest dimension of the specimen. All these observations underline a very important aspect of *bcc* deformation behavior of *bcc* crystals that the slip activity in *bcc* metals is influenced by the specimen geometry.

While no mechanistic interpretation was offered by Vesely, Matsui et al. [210] proposed that the image force due to the presence of free surface aids the mobility of screw dislocations by nucleating kinks on it and thereby promoting slip on a low stressed plane in preference to the highest-stressed plane. Accordingly, the geometry of the sample determines the orientation of the slip direction which interacts most strongly with the free surface and the plane on which image force on screw dislocation is largest. The main result in the simulation presented in section 4.8, similar to the experiments, is that for the pillar A, the primary slip system ($\bar{1}$01)[111] has the largest contribution to plastic flow as expected and for pillar B, the conjugate slip system (101)[$\bar{1}$11] contributes the most. However, in the simulation, the surface effects as proposed by Matsui et al. [210] are not accounted for because a screw segment with node on the surface is constrained to remain straight (refer appendix section A.1) and hence surface effects cannot be responsible for a larger activity of the conjugate slip system in pillar B.

Here, we show that the greater contribution of the (101)[$\bar{1}$11] in pillar B towards total deformation is due to a volume effect than due to image forces. The length effect of the longest screw dislocation discussed in section 5.3.2 plays a decisive role since by changing the geometry of the pillar, the longest possible length of the screw dislocation spanning the volume is altered. Fig. 5.13 shows that in the pillar B, [$\bar{1}$11] conjugate slip direction spans the longest length of the pillar compared to the

[111] primary slip direction in the pillar A. Therefore, on an average, after attaining screw orientation, a screw dislocation with a/2[$\bar{1}$11] Burgers vector is much longer than the a/2[111] screw for pillar B. Hence the latter slip direction here has a larger number of kink-nucleation sites and higher probability of multiplication and activation due to interactions with other dislocations.
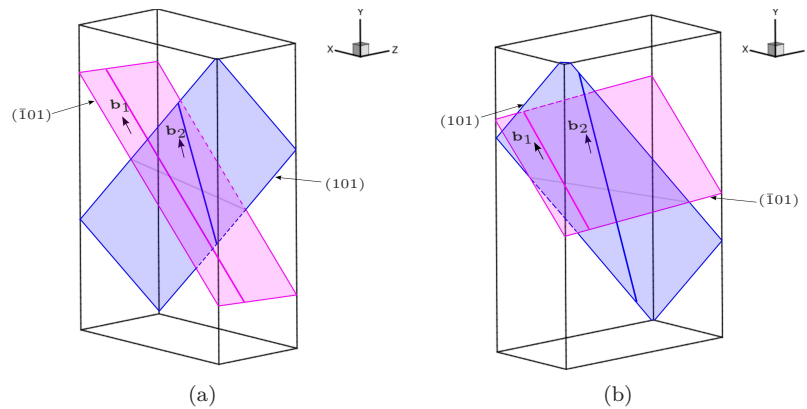
Figure 5.13.: Figure (a) shows the two pillars A and B and the constraint imposed by the geometry of the pillar on the maximum possible length of the Burgers vectors. **b**$_1$ and **b**$_2$ are the Burgers vectors a/2[111] and a/2[$\bar{1}$11] respectively. In (a) and (b), screw dislocations with the a/2[111] and the a/2[$\bar{1}$11] Burgers vector have on an average the longest possible length. Accordingly, screw dislocations with the a/2[111] and a/2[$\bar{1}$11] Burgers vectors have the largest number of intersecting points with other dislocations inside the volume.

Thus, the observed change in the deformation behavior in pillar A and B is therefore due to varied geometry of the pillars which influences the longest $\langle 111 \rangle$ Burgers vectors spanning the volume. The effect of geometry and interactions is to alter the contributions of the slip systems to the plastic flow and therefore for pillar B, a large portion of slip occurs on the macroscopically low stressed (101)[$\bar{1}$11] slip system. This also emphasizes the need to account for interactions in crystal plasticity formulations of plastic flow in *bcc* metals.

Simulations on single-slip oriented *fcc* pillars by Senger et al. [212] with $l = 0.5 \; \mu$m show that a secondary slip system with lower Schmid factor is only activated once the highest Schmid factor system is blocked in its operation due to dislocation reactions leading to lock formation and subsequent blocking of sources on most active planes. Other less favorable slip systems owing to their low Schmid factors are activated only after the suppression of activity on higher-Schmid factor planes. In comparison, the simulations on W presented in this work show that this is not a necessary condition. In general there are always sufficient sources of dislocation present on the primary plane and no blocking is observed. In all the simulations, the conjugate slip system $(101)[\bar{1}11]$ plays contributes almost equally as the primary slip system $(\bar{1}01)[111]$ towards total strain. The primary reason for this behavior is also because for this orientation, the conjugate Burgers vector spans a longer length inside the specimen which increases the number of kink-pair nucleation sites by local stresses due to its interaction with dislocations on other planes. Any activity on primary system due to motion of screw or mixed dislocations is accompanied by subsequent activity on conjugate slip directions.

5.3.4. Mechanisms of anomalous slip

Among the characteristic features of anomalous slip described in section 2.2.1, the most important aspect is the occurrence of well-defined slip trace on the $(0\bar{1}1)$ plane over a large specimen area. In the simulations performed in this work, anomalous slip is observed in pillars loaded along the $[\bar{1} \; 5 \; 10]$ direction and is in good agreement with the experiments on pillars with the same geometry [208]. For the $[\bar{1} \; 4 \; 9]$ oriented pillars too, anomalous slip is observed in both uniaxial tension and compression. The occurrence of anomalous slip in simulations is surprising because the screw dislocations glide primarily on their lowest activation enthalpy planes. Accordingly, the screw dislocations with Burgers vector a/2[111] and a/2[$\bar{1}$11] are expected to move on the $(\bar{1}01)$ and (101) planes respectively (see for example Fig. 4.16). In the following sections, the classical mechanisms of anomalous slip are reviewed and then two new mechanisms are proposed which lead to anomalous slip in the simulations.

Surface-effect mechanism

The surface-effect (SE) mechanism proposed by Matsui et al. [213] advocates that image stresses perpetually create an edge component on a screw dislocation on the anomalous plane by rotating the screw dislocation locally out of its screw character. With increasing applied stress, the edge/mixed component gets activated and moves at stresses lower than CRSS of screw dislocation on the anomalous plane. The motion of the edge/mixed dislocations is attributed to the straight crystallographic slip traces typical of the anomalous slip [98,193,213]. A necessary requirement of this model is that the slip direction and the crystal surface make a small angle with each other and slip plane must be nearly normal to the local crystal surface.

However, Taylor [214] remarked that for certain loading axes within the stereographic triangle, on cylindrical specimens, the plane most nearly normal to the surface was the $(\bar{1}10)$ plane and not always the $(0\bar{1}1)$ plane. Also for cylindrical specimens, the plane perpendicular to the surface containing a given Burgers vector varies with local crystal orientation in that all planes in the zone of a given slip direction are equally favored yet not observed in experiments.

The SE mechanism however, cannot account for the disappearance of anomalous slip with increasing temperatures. This is because the strength of image force is temperature independent. If the SE mechanism were to be active, screw dislocations at any temperatures should contain edge segments lying on the anomalous plane. This mechanism should therefore be active in the low and medium temperature range in which the critical stress needed to move edge dislocations is much smaller than the CRSS of screw dislocations. Therefore, contrary to the experimental observations [4, 55], at low and medium temperatures, the SE mechanism would predict plastic slip in *bcc* metals to occur on the anomalous plane. In the simulations, the modeling constraint that a screw dislocation on surface remains straight (see section A.1) ensures that this mechanism is not active in the simulations and is not responsible for the observed anomalous slip.

Co-planar double slip mechanism

To overcome the drawbacks of the SE-mechanism, Matsui et al. [192] proposed the co-planar double slip (C-D-S) mechanism of anomalous slip. It was motivated by TEM observations of dislocation structures which revealed a network of primary and conjugate $\langle 111 \rangle$ screw dislocations bound together by the $\langle 100 \rangle$ junctions on the anomalous plane. An example of such a network formation observed in Mo is shown in Fig. 5.14. The mechanism envisages that the $a/2[111]$ and $a/2[\bar{1}11]$ screw dislocations, which are co-planar on the $(0\bar{1}1)$ plane, glide co-cooperatively on the anomalous plane. Kink-nucleation is proposed to occur at the junction node on the anomalous plane and is subsequently transmitted conservatively around the network [192] generating slip the anomalous plane. *In situ* observations [194] of motion of dislocation networks involving the primary and conjugate Burgers vectors on the anomalous plane seemed to support this view. Bulatov et al. [215] investigated the atomistic aspects of migration of such a network and found that in principle, conservative motion of network is possible due to enhanced mobility of screw dislocations at the junction nodes. Louchet et al. [178, 195] also proposed a similar model in which anomalous slip occurs when the dislocations with $a/2[111]$ and $a/2[\bar{1}11]$ Burgers vector first cross-slip onto the anomalous plane and form a $a[100]$ junction. Then the entire network is proposed to glide collectively on the anomalous plane in a manner similar to the C-D-S mechanism. Moreover, Garrat-Reed [193] reported anomalous slip in Nb specimens, where such a network structure was absent, which suggests that the network formation is not a pre-requisite for anomalous slip.

For the C-D-S mechanism to operate and the network to move conservatively on the anomalous plane, the transmission of kink nucleated at the junction across the network would require that the network itself be planar. The DDD simulations however, show that the network structure is typically non-planar and the screw dislocations on a given plane around the junction are kinked/jogged. To illustrate this point, a snap-shot from a simulation in compression on the pillar along the $[\bar{1}\,4\,9]$ orientation is shown in Fig. 5.15 which reveals a non-planar network similar to experiments (Fig. 5.14). Kink-transmission across such a non-planar network leading to anomalous slip would be require non-conservative motion which is not possible at low temperatures [12].

Figure 5.14.: Typical network structure of irregular shaped screw dislocations formed in Mo reproduced from [98]. R denote the junctions with Burgers vector of ⟨100⟩ type. D and L denote the dipole trails and dipole loops respectively.

In the simulations, however, an alternate mechanism of conservative motion of dislocation network is observed which contributes to slip on other low-stressed planes. The glide of the network occurs locally over a limited region and it always occurs when one of the reactant ⟨111⟩ dislocations has edge/mixed orientation which drives the entire configuration, similar to the manner described in section 5.3.5 (see also appendix B).
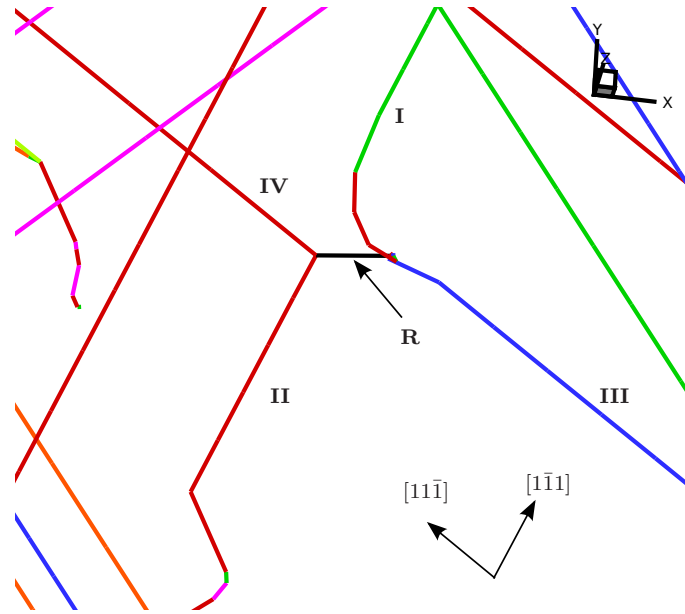
Figure 5.15.: Figure shows a non-planar network of ⟨111⟩ dislocations joined together by the reaction product **R** Burgers vector [100]. The reactant dislocations have Burgers vector a/2[1$\bar{1}$1] and a/2[11$\bar{1}$] respectively. The reaction product lies on the (011) plane. The dislocation arms I,II, III and IV which form the network do not all lie on the same plane.

Other mechanisms

More recently, Hsiung [99, 216] attributed the occurrence of anomalous slip to the collective effects of dislocation multiplication, interaction and subsequent propagation on the anomalous plane. This mechanism however cannot account for the coarse crystallographic slip trace over a large specimen area which is a characteristic feature of anomalous slip. This is because cross-slip on anomalous plane due to local stress-variation occurs only over a short-distance and only as long as the local stress-variation is favorable. As soon as the stress-variation is absent, the screw dislocation cross-slips back onto its low enthalpy plane.

The mechanisms described previously also cannot account for the occurrence of coarse slip traces over large specimen area as observed in the pillar experiments [208]. In the next sections, the mechanisms of anomalous slip observed in the simulations are described which demonstrate that anomalous slip is a result of dislocation interactions.

Stress-induced cross-slip

The first mechanism contributing to anomalous slip is stress-induced cross-slip. A snap-shot of a [111] screw dislocation cross-slipping on the anomalous plane $(0\bar{1}1)$ is shown in Fig. 5.16. Dislocation interactions can cause stress-variation along the screw dislocations on both the primary and conjugate slip systems and impose a stress-state which favors cross-slip via nucleation of kink pairs on the anomalous plane. The kink generated is now confined to move on the anomalous plane which glides along the screw dislocation and thereby generates plastic slip. This local activation is short-lived and the screw part on the anomalous plane cross-slips back to a plane parallel to the initial plane, once the local stress is no longer favorable. This mechanism occurs mostly inside the pillar volume and does not create large slip traces on the surface of the specimen.

Cross-kink mechanism

A second mechanism that generates slip on the anomalous plane is identified here. Kink-pair nucleation can in principle occur on any of the three distinct $\{110\}$ planes of the $\langle 111 \rangle$ Burgers vector. If opposing kinks are nucleated on the same plane, they migrate towards each other under stress and annihilate each other. If however, opposing kinks are generated on different $\{110\}$ planes, they can migrate towards each other along the screw dislocation and collide to share a common node, which is called a cross-kink. Fig. 5.17 shows a sequence of snapshots extracted from the 3D simulations which leads to anomalous slip. The cross-kink is formed by the kinks **AB** and **BC** which were generated by prior dislocation interactions and move towards each other. They collide at the common node **B** forming a sharp angle. In general, the two kinks are of different lengths and experience different driving forces but they are geometrically
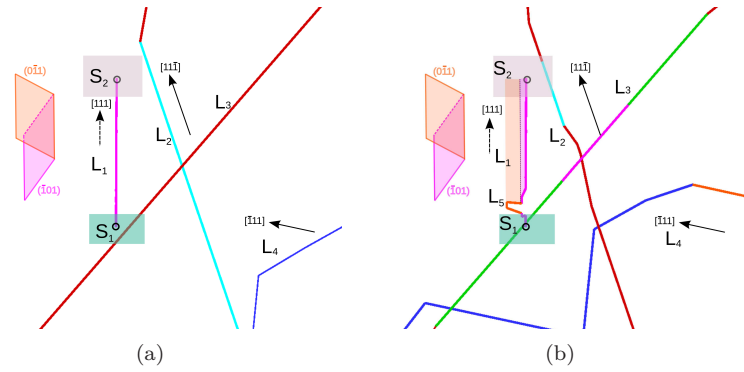
Figure 5.16.: The mechanism of stress-induced cross-slip on dislocation L_1 with [111] Burgers vector in screw orientation. Due to interaction of L_1 in (a) with the neighbor dislocations (L_2, L_3 and L_4) locally cross-slip occurs over a small area on the anomalous plane (L_5). The corresponding areas traced by the segments is also shown in color in (b). S_1 and S_2 are the local surfaces which are only displayed for clarity. The intersection of the dislocation line with the surface is marked with open circles. Broken lines on arrows indicate the direction (projected) is going into the plane of paper and solid lines indicate in the plane of the paper. The dislocation lines are colored according to their habit planes (see appendix C for color code).

constrained to glide together. Their effective direction of motion depends on the resultant force which can drive the kink segment on the anomalous plane (AB in figure 5.17(a)) against the direction in which it would want to move alone.

Fig. 5.17(a) displays such a scenario where the segments **AB** and **BC** form a cross-kink. The free surface of the pillar is indicated in grey color and marked with **FS**, the glide planes are indicated in orange $(0\bar{1}1)$ and blue (1-01). The colors of the lines are according to their habit planes. The end **A** is attached to a screw dislocation while the end **B** is connected to a section of several small segments of mixed character on several planes. Since both nodes **A** and **B** are kinematically constrained to move along the Burgers vector direction, they cannot separate.

The direction of motion of the entire complex is indicated with the arrow **M**. In Fig. 5.17(b), node **A** reaches the surface and is released from
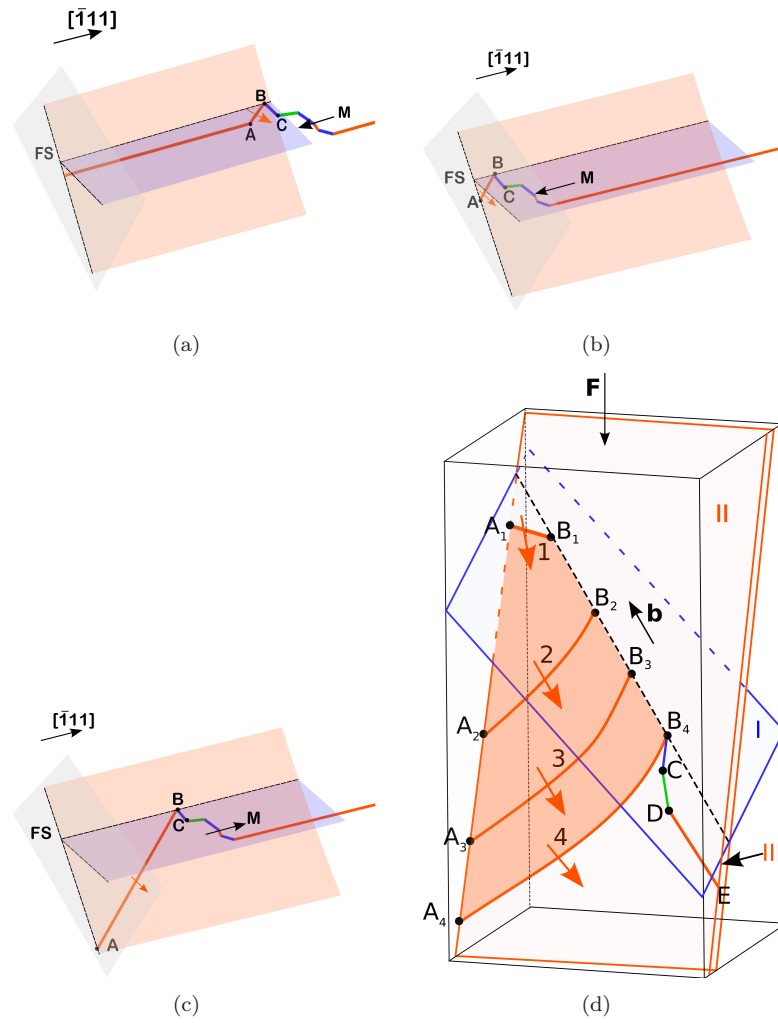
Figure 5.17.: Mechanism of anomalous slip. Snapshots ((a)-(d)) of small sections of the sample show the occurrence of anomalous slip due to [1̄11] dislocations on the anomalous (01̄1) plane. See text for description.

the screw dislocation. The dislocation section **AB** which experiences a driving force into the specimen, can then rapidly increase in length and thereby generate slip on the anomalous plane as shown in Fig. 5.17(c). In Fig. 5.17(d), an overlay of the dislocation structure at four time steps after the release of node **A** is shown. The mixed segment **AB** glides back in the direction of the orange arrow. Node **A** moves along the intersection line of the anomalous plane II with the surface and the node B moves along the screw dislocation along the intersection of planes I and II. The segment **DE** is screw oriented and lies on plane III parallel to II. Segment **BC** moves on plane I and **CD** represents schematically the kink-complex attached to **BC**. The motion of segment **AB** resembles a single armed source sweeping a large area on the anomalous plane, before it can again attain screw orientation. Since this mechanism produces slip by the motion of mixed dislocations on the anomalous plane, it generates coarse slip traces over a large region of the surface.

The cross-kink mechanism is also observed to operate in the simulation on pillars for loading in the $[\bar{1}\ 4\ 9]$ orientation which shows that it is independent of the loading sense. This is consistent with the fundamental feature of anomalous slip that the anomalous slip plane is same in tension and compression [4, 30].

It remains to account for how the cross-kink based model mechanism can explain the disappearance of anomalous slip at higher temperatures. It may be possible that at higher temperatures, many thermal kinks may be present on a screw dislocation due to thermal activation. They may mutually block each other and the motion of cross-kinks towards surface may be limited thus suppressing the operation of this mechanism.

The orientation dependence of the anomalous slip as observed in the experiments on Nb [193] at low temperatures can also be well-accounted for with this mechanism. It has been observed that for loading orientations towards the [001] corner of the stereographic triangle, probability of anomalous slip increases and towards the [011] corner, it decreases. For loading orientations towards the [001] corner of the stereographic triangle, the Schmid factors of both the $(0\bar{1}1)[111]$ and $(0\bar{1}1)[\bar{1}11]$ systems increases reaching a maximum at the [001] corner. Therefore, there is a higher probability of cross-kink formation on the anomalous system due to stress-induced cross-slip. The edge segments of the cross-kinks experience

higher driving force towards the surface and thus increased contribution of anomalous slip to total deformation.

For orientations towards the [011] corner, the Schmid factors of both the $(0\bar{1}1)[111]$ and $(0\bar{1}1)[\bar{1}11]$ systems decreases reaching zero at the [011] orientation which means that both the probability of cross-slip of a screw segment leading to generation of cross-kinks as well as the lower applied stresses experienced by the CK would result in a lower occurrence of this mechanism. Hence the contribution of anomalous slip towards total deformation is expected to decrease.

5.3.5. Mechanisms of dislocation motion

The simulations show that the total deformation occurs by a complex aggregate of several individual mechanisms. In this section, some new mechanisms of screw dislocation motion are presented which may account for several experimental observations. These mechanisms occur in all simulations both in tension and compression and affect the dynamics of screw dislocations.

Motion of dislocation network

In the classical picture of motion of dislocation network together at $\langle 100 \rangle$ junctions, it is assumed that the $\langle 111 \rangle$ dislocations forming the network have screw orientations only [194, 215]. In the simulations performed in this work, a network in which both the $\langle 111 \rangle$ dislocations have screw orientation are not observed to move because $\langle 100 \rangle$ junctions are assumed to be immobile. However, conservative motion of dislocation network of $\langle 111 \rangle$ screw dislocations has still been observed. Here we present an alternate mechanism of the glide of a dislocation network due to a mixed dislocation segment which is attached to the junction node. It must however be remarked that such events are rare.

Fig. 5.18 shows a snap-shot from a larger simulation in compression along the $[\bar{1}\ 4\ 9]]$ direction, where the motion of screw dislocation at junction node is aided by edge/mixed dislocations. Loop L_2 and L_3 with Burgers

vectors [111] and [1$\bar{1}$1] respectively are locally attractive at **J**. A macro-kink E on the screw part of the loop L_3 is generated remotely and it glides in the a/2[1$\bar{1}$1] direction. As it encounters the reaction J along its path, the mixed segment E of loop L_3 and the screw part of the loop L_2 then share a common node at **J**. Since they are locally attractive, the common node is driven by the mixed dislocation E which can glide at low stresses. E also exerts a force on the screw part of loop L_2 and activates it. The entire network glides forward in this manner due to the motion of mixed dislocation E. This example also illustrates how a single activation event such as generation of macro kink such as E on a screw dislocation and its subsequent migration along the screw dislocation line leads to a succession of further events generating plastic slip.

In order to demonstrate that the activity of the screw part of loop L_2 is due to mixed segment E, the macro-kinks generated on L_2 are ana-lyzed. The formation of macro-kinks indicates that different parts of the screw segments presence of loop L_1 in its vicinity, experience different stresses and the common node at the reaction **J** glides much faster than the rest of the screw dislocation. The macro kinks accumulate inside the specimen at pinning point P_2. Thus a locally non-screw segment of the ⟨111⟩ segment attached to an immobile ⟨100⟩ junction can also activate an entire dislocation network where the screw dislocation glide occurs by mutual interaction.

Similar mechanism has also been observed on other low stressed planes where the edge or mixed dislocation segment gliding on a high-stressed plane initiates glide of network on a low stressed plane generating anoma-lous slip. Since such a slip is generated by locally activated events, it leads to slip over a small area. Another example of the motion of network in tension is shown in appendix Fig. B.2.

Mixed dislocation driven screw motion and Jerky motion

Recent low temperature *in situ* experiments have reported jerky-motion of screw dislocations [217]. The main characteristics of jerky motion are sudden jumps of screw dislocation over distances larger than the nearest Peierls valley and large instantaneous changes in velocity of a screw dis-location. The jump-lengths were not constant and the screw dislocation
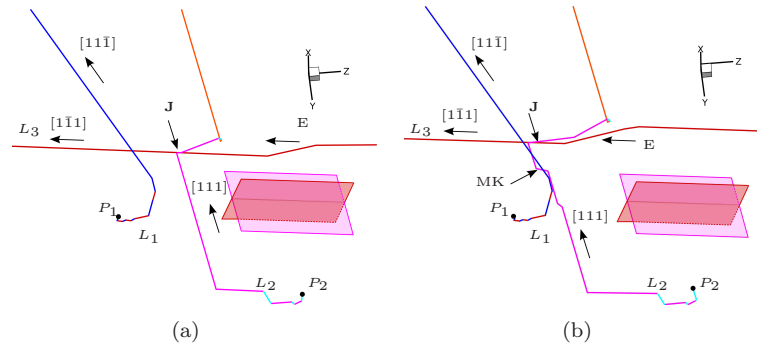
Figure 5.18.: Figure shows how a sequence of events can trigger other events during deformation and how macro-kinks may be generated on a screw dislocation. Loops L_1, L_2 and L_3 have Burgers vectors a/2[11$\bar{1}$] , a/2[111] and a/2[1$\bar{1}$1] respectively.

velocity showed an increase by a factor of about 10^3. It is thought that both these features are incompatible with the classical kink-pair mechanism. This is because the classical kink-pair theory necessitates that each successive kink-pair nucleation leads to forward motion of screw dislocation to the next Peierls valley only. The occurrence of jerky-motion due to large spatial variation of the internal stress was also rejected on grounds that such large changes in velocities require a large change in dislocation density (a factor of 2.5 in $\alpha-$Fe) which was also not observed in the experiments.

A locking-unlocking mechanism involving the glide of a screw dislocation over several Peierls valleys was proposed by Caillard [217]. According to this mechanism, a screw dislocation may remain locked in a Peierls valley until it is unlocked by a critical bulge configuration, which is a variant of the kink-pair configuration. The critical bulge configuration represents a metastable configuration of the dislocation core that does not experience the effect of intermediate Peierls valleys and can thus glide over several Peierls valleys. Once the glide occurs, the screw gets locked before being unlocked again by the same mechanism.

However, the occurrence of apparent glide of screw dislocations on low Schmid factor planes, in preference to higher stressed plane observed by

Caillard [90], cannot be explained by the locking-unlocking of screw dislocation under the influence of macroscopic stresses alone. This is because the screw dislocations would move on lowest activation enthalpy planes. An alternate mechanism for jerky motion is proposed here based on the interaction between mixed and screw dislocations.

It is shown here that this elementary interaction exhibits the same characteristics necessitated by the jerky-motion and is still consistent with the classical kink-pair mechanism. Firstly, the studies of mixed and screw dislocation interaction presented in section 4.5 show that the local stress acting on a screw dislocation can increase by more than 2 GPa due to its interaction with mixed dislocation on a lower-stressed plane. This change can be quite rapid and occur over a very small interval of about 10 b. The velocity reached by the screw dislocation is also the maximum flight velocity allowed in the simulation (300 m s^{-1}) showing an increase by about a factor 10^3 similar to that observed in experiments [217].

Fig. 5.19 shows a snap-shot from the simulation on pillar in compression along the $[\bar{1}\,4\,9]$ direction showing an instance of mixed dislocation driven screw dislocation. The mixed dislocation loop L_2 with Burgers vector $a/2[\bar{1}11]$ gets activated after attaining a critical configuration glides in the vicinity of $a/2[111]$ screw dislocation. As a result, the screw arm of the loop L_1 cross-slips from the the $(\bar{1}01)$ plane onto the low-stressed $(\bar{1}10)$ plane. The Schmid factor of the $(\bar{1}10)[111]$ slip system is half that of the $(\bar{1}01)[111]$ slip system. The activation of low-stressed slip system in preference to high stressed slip system confirms that the interaction between mixed and screw dislocation changes the local stress state significantly in a short interval of time. This points towards the possibility that the jerky motion of screw dislocations is rather due to interaction between mixed and screw dislocations and not an intrinsic mechanism of screw dislocation.

Bulk stress-strain curves

The activation of screw dislocations by mixed dislocations at low-applied stresses could significantly influence the shape of the stress-strain curves
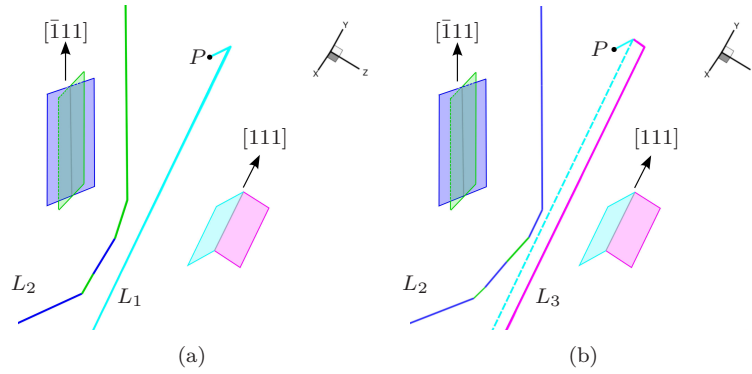
Figure 5.19.: (a) shows the local activation of [111] dislocation (loop L_1) pinned at P due to interaction with incoming loop L_2 moving in its vicinity. The screw part of L_2 is activated remotely causing it to change its glide plane from (110) plane to ($\bar{1}$01). In (b), the local stress field change due to motion of L_2 in its vicinity causes cross-slip of screw part of L_1 from ($\bar{1}$10) plane to ($\bar{1}$01) plane.

in bulk specimens. Typical bulk stress-strain curves of several *bcc* metals like W [50, 52, 55, 61, 177], Mo [44, 45, 47, 94, 184, 218] show a characteristic parabolic stress-strain response at low temperatures for center-triangle (single slip) oriented specimens. Classically, the parabolic regime is referred to as the microplastic regime and attributed to strong initial work hardening [47, 184, 197, 207]. The mechanistic picture behind the parabolic response is however not understood. Brunner [55] suggests that exhaustion of mixed dislocations on secondary slip systems alone cannot account for the parabolic shape of the stress-strain curves.

It is argued here that the parabolic form of the stress-strain curve observed in experiments is not due to work hardening but rather due to energy dissipation caused by plastic flow associated with : 1.) Exhaustion of mixed dislocation sources on secondary slip systems before the CRSS of screw dislocation on primary slip system is achieved 2.) Interaction between mixed dislocations and the forest screw dislocations.

The simulations on pillars for the [$\bar{1}$ 4 9] orientation show that in the early stage of deformation before before the CRSS of screw dislocations

of the highest stressed slip system is reached, mixed dislocations on the secondary slip systems are activated generating forest screw dislocations. Both attractive and repulsive trees are generated in equal density. The order of operation of the slip systems follows the Schmid law. The same order of slip activity in the early stages of deformation is also expected in bulk specimens. The density of forest dislocations in the early stage of deformation depends on the CRSS of screw dislocation of the primary slip system. Every newly activated secondary slip system interacts with an increasing density of forest screw dislocations. The simulation results in section 4.5 show that the repulsive interaction between mixed and screw dislocations can activate the screw dislocations even if macroscopically the CRSS of screw dislocations is not reached, thereby generating plastic slip. This local plastic slip event manifests itself as a non-linearity in the stress-strain curve. The total slip contribution due to the interaction between mixed and forest trees therefore depends on the density of forest dislocations available. At low-temperatures where the CRSS of screw dislocation is high, larger contribution of plastic slip in the early stages of deformation is expected from the larger activity of secondary slip systems and greater interaction between mixed dislocations moving on secondary slip systems and forest screw dislocations. Accordingly, the stress-strain curve is expected to deviate increasingly from the linear elastic response and show greater non-linear response in the early stages of deformation with decreasing temperature, consistent with the experimental results.

5.4. Peierls stress and comparison with experiments

Due to the dependence of the Peierls barrier on the applied loading, it is essential to recall the notion of Peierls stress as deduced from experiments and its comparison with the theoretical value derived from atomistic simulation. The Peierls stress is defined as the critical Schmid stress needed to displace an isolated screw dislocation at 0 K. In contrast, what is referred to as the Peierls stress in experiments is obtained from uni axial tension and compression tests over a range of temperatures by extrapolating the effective resolved shear stress to 0 K.

Atomistics results show that the activation enthalpy, and therefore the Peierls barrier and the Peierls stress depend on the stress tensor $\overline{\boldsymbol{\Sigma}}^\chi$, one has to compare the experimental Peierls stress with that obtained from the corresponding loading. We execute this here for the example of the $[\bar{1}\ 4\ 9]$ orientation ($\chi = 0°$ and $\eta = 0.51$) for which experimental data is available [55, 177]. Extrapolation of our data for tensile loading to 0 K gives a value of about 3.6 GPa (0.022 C_{44}). The value obtained from the atomistic simulations corresponding to $\sigma = 0$ (pure shear parallel to the slip direction) and $\chi = 0°$ is about 4.7 GPa (0.029 C_{44}) from Gröger et al. [9]. This means that due to the effect of the shear stress perpendicular to the slip direction a reduction of the Peierls stress by about 25 % can be accounted for. As discussed above, the effect of the non-Schmid stresses decreases at higher temperatures. Even at 300 K the reduction of the calculated yield stress in tension as compared to pure shear is of the order of 10 %.

It must of course be noted that the obtained value for the Peierls stress from atomistic simulation is still much larger (by about a factor of about 3) than the experimentally deduced Peierls stress even if this correction is made. Interestingly, the discrepancy between the calculated yield stress and the experimental yield stresses remains at this difference of a factor of 3-4 up to room temperature. This discrepancy has been known for some time and several models are discussed to explain the discrepancy. A lowering of the atomistically determined stress could for example come from the collective glide of dislocations in array [140] or the stress variations in complex dislocation networks. Quantum-mechanical tunneling has also been proposed as a mechanism which aids screw dislocations in overcoming the Peierls barrier without the need for thermal activation [219–222] and thereby questioning the applicability of the classical Arrhenius law in the low temperature regime. Even the influence of zero point vibrations in aiding dislocation motion [223, 224] and applied specifically to screw dislocation motion in *bcc* metals by Proville et al. [225] has been proposed as a major source of this discrepancy. Similarly, the role of interfaces or surfaces for kink-nucleation [213] or even the inertia of the dislocation could contribute to motion of dislocation over several Peierls valleys after an activation event [226]. It must be mentioned, that recent micropillar compression experiments from W single crystals [108] at room temperature yielded resolved shear stresses of the order of 0.8-1.0 GPa

for pillars with diameters above 2 μm and significantly larger resolved shear stresses of the order of 1.5-2.0 GPa for pillars with diameters below 500 nm. Surface kink nucleation and similar effects should actually soften the smaller pillars and can therefore be responsible for the differences in Peierls stress. More complex dislocation structures in larger pillars and even more so in macroscopic specimens might also be responsible for further reduction of the Peierls barrier.

Full DDD simulations on pillars in section 4.7 show that the initial yield stress at which is defined by large scale motion of screw dislocations can be lowered by at least 10% in tension compared to the flow stress needed for periodic activation of single FR source due to internal stresses. In compression, as much as 17% of the total stress is contributed by internal stresses owing to the prior activity of screw dislocations on conjugate slip system. A larger lowering occurs in compression than in tension because the studies on dislocation interactions between repulsively interaction screw dislocations show that the difference in the CRSS of the screw dislocations on primary and conjugate screw dislocations in compression is lower than in tension (see Fig. 4.21(a) and (4.21(b)). Thus the CRSS of a conjugate screw dislocation is reached much early in compression due to repulsive interactions than in tension which is responsible for a larger decrease in the effective stress in simulations.

From the above considerations it can be concluded that, in addition to the non-Schmid stresses, internal stresses also lead to reduction of the effective flow-stress. Anomalous slip causes a further reduction of the effective flow-stresses. Stress-concentration points around a screw dislocation also can contribute to the effective lowering of CRSS of screw dislocations. These effects are also certainly present in experiments. Hence it is argued that the true magnitude of the Peierls stress discrepancy between the experimental value of CRSS (which is related to highest Schmid factor plane only [55, 61]) and those obtained from atomistic simulations certainly cannot be interpreted in terms of single dislocation picture alone. The role of mixed dislocations in accommodating the applied strain rate can certainly not be neglected.

6. Conclusions

The main aim of this work was to develop a multi-scale model for transferring the key atomistic information of screw dislocations to a mesoscale DDD model to enable the simulation of the plastic flow of *bcc* metals. The model takes into account the effect of applied loading and incorporates non-glide components of the stress tensor which strongly influence the critical resolved shear stress. The local stress state modifies the Peierls barrier on the three possible glide planes of the screw dislocation and thereby changes the energy barrier for kink-pair nucleation on these planes. The plane with the lowest activation enthalpy then controls the slip of the dislocation.

The model which describes the activation of screw dislocation based on the minimum activation enthalpy of kink-pair nucleation, can account qualitatively very well for the experimentally observed slip on the MRSSP at higher temperatures, the tension-compression asymmetry and the orientation dependence of slip activity. This non-Schmid framework, based on atomistic input, naturally provides a physically based description for the activation of low-Schmid factor planes under compressive loading.

Classically, the {112} and {123} planes have also been considered as elementary slip planes to account for orientation effects. It is shown here that the experimentally observed $\overline{\psi} \rightarrow \chi$ relationship can very well be described by considering {110} as the elementary slip planes only. A new method is proposed to identify the elementary glide planes in the bulk of a *bcc* metal at high-temperatures. The method exploits the fact that from the line direction of a binary sessile junction, the glide planes of the reactant dislocations can be unambiguously identified. The occurrence of elementary slip on every $\{hkl\}$ plane results in a unique possibility of line direction of the binary junction. The occurrence of such directions in experiments can be exploited as a unique signature of slip on high index planes.

The repulsive interactions of screw dislocations reveal a fundamentally different mechanism which is contrary to the prevailing knowledge. Two interacting repulsive screw dislocations always behave as rigid lines and maintain a critical distance before they glide collectively in their respective planes. The equilibrium distance depends on the Burgers vectors involved and the sense of loading. The activation of the driven dislocation occurs at the point of strongest interaction with the driving dislocation. This also shows that the nature of interactions in W and possibly other *bcc* metals is fundamentally different from that of *fcc* metals. More importantly it emphasizes the role of accounting for non-Schmid stresses in modeling the effect of interactions can lead to change in the local activation barrier for screw dislocation. Due to the non-Schmid stresses, the experimentally determined screw dislocation parameters like activation enthalpy and activation volume determined from experiments must be treated with caution as the quantitative effects of non-glide stresses cannot be accounted for.

The interaction of fast moving edge/mixed dislocation with screw dislocations show that locally the Peierls stress can be exceeded even though the macroscopic applied stress is well-below the CRSS of screw dislocation. As the stress-change is quite rapid varying strongly with the distance, the screw dislocation has a very large kink-pair nucleation rate and a rapid rise in its velocity. This offers an alternative explanation to the jerky motion observed in the recent in-situ experiments on iron [217].

A fundamental assumption in this work was the assumption that isolated screw dislocations glide at atomistic values of CRSS which is typically a factor of $2 - 3$ higher than the corresponding Peierls stress obtained from experiments and the mobility is described by the classical Arrhenius law. This was based on the credibility of the DFT and 0 K atomistic simulations using different interatomic potentials, which have consistently predicted a much higher value of CRSS of screw dislocations compared to experiments. Comparing the Peierls stress and the temperature dependence of the flow stress, calculated on single dislocations in our model, between pure shear (usually assumed in atomistic modeling) and tensile loading (usually used in experiments), it has been demonstrated that the non-Schmid stresses can lower the critical stress by as much as 25%. Nevertheless, the critical stress in agreement with the underlying atomistic data in this model, is still a factor of about 2 to 3 higher than the experimentally observed values [62] even after properly representing the non-

Schmid stress contributions of a tensile test. Large scale DD simulations on fully interacting dislocations in micropillars show that the initial yield stress which is defined by large scale motion of screw dislocations can be lowered by at least 10% compared to the CRSS of an individual screw dislocation in tension due to internal stresses. In compression, a lowering of yield stress by as much as 17% occurs because screw dislocation motion due to the repulsive dislocation interactions in compression occurs at larger mean distance (and lower internal stresses) between screw dislocations than in tension. Once the screw dislocations begin to glide on their respective planes, a large stress-drop is observed due to generation and motion of mixed dislocations and the plastic deformation proceeds at lower stresses.

Simulations on single-slip orientated micropillars loaded in uniaxial tension and compression show double slip on the highest and second highest stressed slip systems. The large activity of the latter is because the slip direction of this slip system spans the largest length inside the pillar and has a larger probability of interaction and subsequent activation due to dislocation glide on other slip systems. This effect is more pronounced in tension because only the highest stressed slip system is only expected to be active owing to the effect of the non-glide stresses as predicted by atomistic yield criteria [9, 10].

A new mechanism of anomalous slip responsible for significant anomalous slip has been identified from simulations based on cross-kink formation and subsequent movement towards surface on the anomalous plane. The mechanism can not only account very well for the observed anomalous slip on experiments performed on W micropillars, but also for the classical anomalous slip observed in most bulk *bcc* metals. The same mechanism is active in both tension and compression and is also consistent with the reported coarse crystallographic slip traces characteristic of anomalous slip. Dislocation-dislocation interactions are the key to generating cross-kinks on the anomalous plane, since screw dislocations preferentially move on their lowest activation enthalpy planes. The simulations also provide ample evidence for the non-planar nature of the dislocation networks due to which it is unlikely for the C-D-S mechanism to be responsible for anomalous slip.

7. Outlook

In the present work, a link has been established between atomistic and the DDD model via the activation enthalpy of kink-pair nucleation. Large scale DDD simulations suggest that the geometry of the specimen plays a key role in determining the longest length of the screw dislocation which may be activated by repulsive dislocation interactions with other slip systems. Therefore, crystal plasticity models should account for the length effect of the longest screw dislocation spanning the volume of the crystal since it can be activated by kink-pair nucleation at any point along its length.

The simulations performed in this work also show that complex structures of mixed dislocations are composed of edge/mixed dislocation segments over several planes are easily generated via cross-slip. Presence of such complex structures increases the probability of intersection with other dislocations and leads to further production of mixed dislocations. This aspect emphasizes that even mixed dislocations are responsible for significant amounts of plastic flow. Although the general trend of evolution of dislocation density is similar to that observed in bulk samples of other *bcc* metals, more detailed microstructure studies are needed to confirm this behavior in micrometer sized specimens.

Three predictions have been made in this work related to the fundamental aspects of deformation in *bcc* metals which could be experimentally verified. Firstly, a method is proposed to determine the elementary slip planes in *bcc* metals from the line directions of $\langle 100 \rangle$ junctions. TEM or TEM-tomography appears to be ideal to determine the line directions of sessile junctions in experiments but the experimental confirmation requires a high accuracy. Secondly, the mechanism of repulsively interacting screw dislocations and their collective motion while maintaining a constant distance between each other can also be verified through *in situ*

experiments. Finally, the occurrence of jerky motion of screw dislocations with the aid of fast moving mixed dislocations can also be verified experimentally. Again, *in situ* TEM experiments are well-suited to verify this proposition.

The cross-kink mechanism of anomalous slip proposed in this work could also be verified through *in situ* experiments. A signature of this mechanism is the presence of uncharacteristically long mixed dislocations gliding on the anomalous plane. One end of the dislocation may be pinned or mobile and the whole configuration reminding of a single-armed source.

This work also raises some important questions which could be answered by atomistic simulations. Firstly, the interaction between mixed and screw dislocations leads to a rapid rise in the stress on a screw dislocation over very short interval of time (which depends on the speed of the mixed dislocation). Calculations based on isotropic linear elastic theory show that the local stress exceeds Peierls stress when the distance between mixed dislocation approaches within a distance of about 8 b, even though macroscopically the external applied stress is significantly lower than the CRSS of screw dislocation. At such small distances, atomistic simulations could offer more insight into the details of the mechanisms of such an interaction.

DDD simulations performed in this work also show that large scale screw dislocation motion is accompanied by repulsive cutting of screw dislocations by mixed dislocations. This would lead to formation of atomic sized kinks on screw dislocation which may change the dynamics of screw dislocation by altering its effective length. The atomic sized jogs have not been accounted for in DDD simulations because of the resolution of DDD methods which is at least a factor 100 greater than atomic dimensions. But the role of jogs on the mobility of screw dislocations could be examined in detail by atomistic simulations. Another important aspect is that this cutting would lead to generation of segments along the M111 orientation direction which also has a high Peierls stress [137, 139]. Therefore, M111 dislocations could infact be rate controlling in *bcc* metals rather than the screw dislocations as suggested by Kang et al. [139]. Further DDD simulations should also account for this additional anisotropy in the dislocation mobility due to the high Peierls stress of the M111 orientation.

A. Appendix A

A.1. Technical aspects of modeling

In addition to the general aspects of numerical modeling discussed in the section 3.3, some specific and very important considerations are necessary for screw dislocation nodes. Firstly, in a strict sense, a screw dislocation must satisfy the exact condition $\mathbf{b} \cdot \mathbf{t} = 1$ where $\mathbf{b}$ and $\mathbf{t}$ are the Burgers vector and the direction of the line segment respectively. Numerical errors limit the enforcement of this criteria. Assigning physical character to dislocation segments based on such a stringent criteria would make the physical behavior of dislocation segments highly sensitive to numerics. Due to large difference in critical stresses to move screw and non-screw segments, a small deviation from the exact condition would cause the algorithm to a assign a mixed character to an otherwise screw dislocation. Therefore the overall dynamics of dislocations can be completely changed due to numerical errors. Hence additional numerical constraints are necessary to prevent these numerical artifacts and yet allow for a transition of segment character from screw to non-screw in a physical manner consistent with atomistic studies.

The recent atomistic studies by Kang et al. [139] also reveal a sharp transition of Peierls stress in the vicinity of screw orientation implying that the transition from thermal to athermal regime of motion of screw occurs in a very narrow orientation range. Accordingly, a small deviation from the perfect screw orientation is tolerated for discriminating screw

segments from non-screw segments in the simulation. A dislocation segment is treated as non-screw if the angle between the Burgers vector and local line direction is greater than about 1.3°. This value is chosen from studies on single screw dislocations and is consistent with the atomistic studies [139].
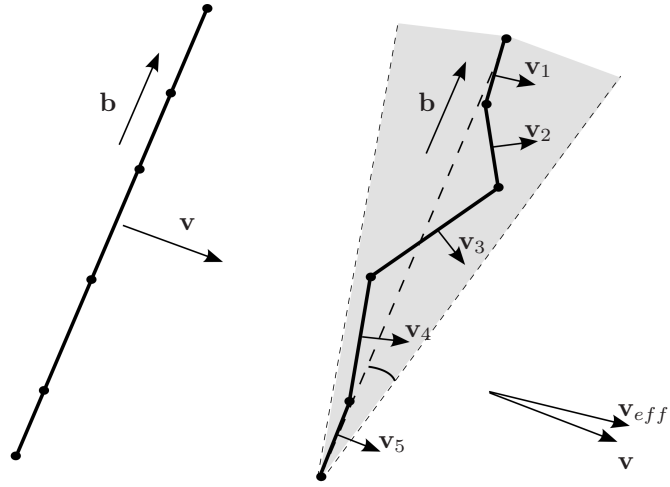

Figure A.1.: Figure shows the effective velocity of screw dislocation computed perpendicular to Burgers vector direction $\mathbf{v}$ and computed perpendicular to the local tangent $\mathbf{v}_{eff}$. Numerical errors cause a deviation of an initially perfect screw dislocation and the two velocities are not parallel. Successive updates of nodal position using $\mathbf{v}_{eff}$ lead to progressive deviation from screw orientation.

The scheme of update of the nodal positions of screw dislocation segments is another source of artifact. This is because in conventional DDD algorithms [163,176], the direction of velocity vector $\mathbf{s}$ is always perpendicular to the local line direction $\mathbf{t}$, i.e. $\mathbf{s} = \mathbf{n} \times \mathbf{t}$ consistent with the direction of the local Peach-Koehler force. An incremental update of nodal position along the $\mathbf{s}$ direction leads to a progressive deviation of the local segment orientation away from the screw direction which is clearly non-physical. This is because due to numerical errors the line direction of a screw dislocation is not exactly parallel to the Burgers vector direction.

Figure A.1 shows schematically the range of orientation around the screw direction which is numerically treated as a screw dislocation. It also shows the initially perfect screw segments can deviate from the screw orientation due to successive nodal position update along a direction perpendicular to local tangent. Instead, for a screw dislocation the direction of velocity is always computed perpendicular to the Burgers vector direction. This ensures that the algorithm for nodal position update does not influence the physics of the screw dislocation. This scheme is used in conjunction with the methodology described in section 3.3.2.

Sliding nodes
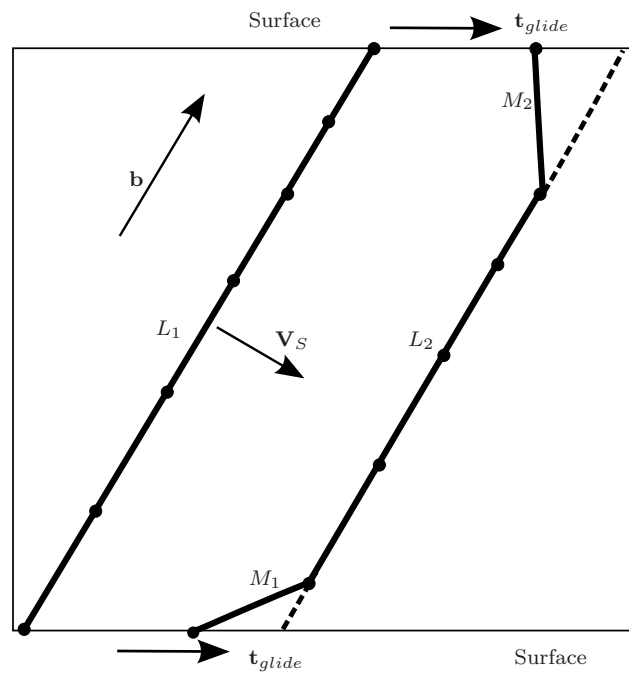
Figure A.2.: A dislocation loop L_1 with all screw segments and both ends on the surface is shown with velocity $\mathbf{V}_S$. M_1 and M_2 are mixed segments which are generated if the surface nodes are updated with a velocity given by equation A.2.

Apart from junctions, nodes which leave the surface are also treated as sliding nodes. In Weygand et al. [163] dislocations leaving the surface are constrained to glide along the intersection line of the glide plane with the local surface

$$\mathbf{t}_{A,glide} \; = \; \mathbf{n}_{gp} \times \mathbf{n}_{surf} \tag{A.1}$$

where $\mathbf{n}_{gp}$ and $\mathbf{n}_{surf}$ are unit normals of the glide plane and the local crystal surface respectively. Since the nodes on surface are constrained to glide along this direction, the resultant velocity of screw node on surface is given by

$$\mathbf{V}_{S,tglide} \; = \; (\mathbf{V}_s \cdot \mathbf{t_{tglide}}) \; \mathbf{t_{tglide}} \tag{A.2}$$

If the surface nodes glide with the velocity given by equation A.2, they may lag behind the screw direction leading to generation of mixed segments M_1 and M_2 as shown in figure (A.2). This may lead to artificial effects during during cyclic loading where a load-reversal would cause the edge component gaining in length and making the whole configuration insensitive to the Peierls stress of the screw segments.

Therefore, a further constraint is enforced on surface nodes of a screw segment such that it always remains in screw orientation. The velocity $\mathbf{V}_{S,tglide}$ of the surface node is further modified according to the equation

$$\mathbf{V}_{S,surf} = \frac{\mathbf{V}_S}{|\mathbf{V_S} \cdot \mathbf{t}_{tglide}|} \tag{A.3}$$

$\mathbf{V_S}$ is the velocity of such a node obtained from the kink-pair nucleation. Eq. (A.3) ensures that the surface node glides along the surface sweeps the same incremental distance as the in volume screw segments and remains in screw orientation. Thus the mobility of screw dislocations represents that of a bulk specimens where the surface effects do not influence the dynamics of screw dislocation.
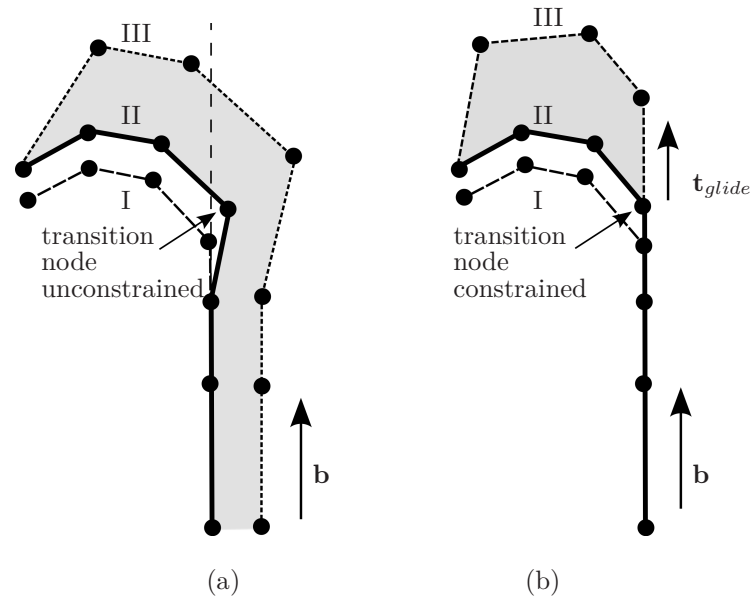
Figure A.3.: (a) From the configuration I, nodes belonging to both non-screw to screw segments may overshoot the screw direction if the lateral component of the velocity of mixed dislocation is not suppressed. Then the edge component dominates resulting in configurations II and III which makes the screw part insensitive to Peierls stress; (b) Such nodes are detected in the simulation and prescribed to glide along the screw direction leading to smooth shapes of loop from I to III.

Another material node which is also treated as a sliding node is one which connects both edge and screw segments. Such transition nodes are prescribed to glide along the Burgers vector direction. This is necessary because numerical errors may cause such node to overshoot the screw orientation by means of artificial configurations as shown in Fig. A.3. The node gets additional edge character and draws the entire screw out of its orientation. To prevent this, the transition node is given an additional glide constraint along the Burgers vectors direction which ensures that the screw-edge transition parts behave well resulting in smooth evolution of loops as shown in Fig. A.3(b).

B. Appendix B

B.1. Alternative operation of cross-kink mechanism

Fig. 4.20(d) shows schematically one possible scenario of operation of the cross-kink mechanism, where the node **B** is free to glide along the Burgers vector direction. Another possibility of operation of the mechanism after the node **A** has reached the surface if the **B** is pinned is shown schematically in Fig. B.1. The total area traced by the segment **AB** depends on the point on the surface at which the node **A** is freed on the surface. The slip trace on the surface is still created as the node **A** can glide freely along the surface even if the segment **AB** encounters resistance due to the presence of forest dislocations. The kink-complex connected at **B** glides towards the surface creating wavy slip traces.
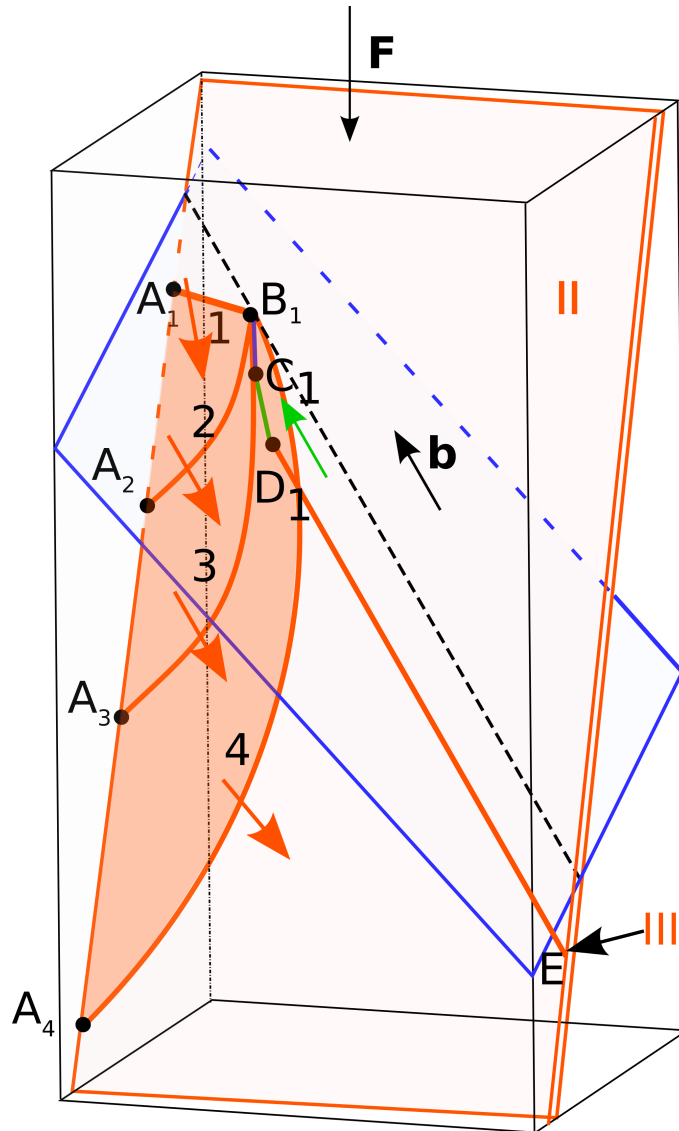
Figure B.1.: Figure shows schematically another possible mode for the operation of the single-armed source on the anomalous plane in addition to the one presented in Fig. 4.20(d). Here the node **B** remains pinned whereas the single armed source operates as shown in sequence (1-4).

B.2. Conservative motion of dislocation network

In this section, another mechanism of motion of dislocation network of $\langle 111 \rangle$ dislocation network with $\langle 100 \rangle$ junctions is presented in addition to that presented in section 5.3.5. The glide of network is surprising because $\langle 100 \rangle$ junctions are modeled as immobile.

Fig. B.2 is a snap-shot taken from the simulation in tension along the $[\bar{1}\ 4\ 9]$ orientation, which shows the operation of a $\langle 100 \rangle$ junctions. In the figure, a network of $\langle 100 \rangle$ dislocations marked **R** can also be observed. Other dislocations visible are long-screw dislocations, serrated screw dislocations connected via kinks, edge and mixed dislocations which are connected at the junction. The junctions are also of variable length. In Fig. B.2(b), a junction with a [010] Burgers vector is formed on the $(\bar{1}01)$ plane. The reaction product with Burgers vector [010] involves attractive interaction between mixed $a/2[1\bar{1}1]$ and a screw $a/2[111]$ dislocation. The circled region in Fig. B.2(a) shows the $a[010]$ junction and B.2(c) shows the junction magnified for clarity. After the reaction, the mixed dislocation glides further in the direction **T** which causes the glide of the common junction node as well. As the mixed dislocation glides further, it interaction activates the $a/2[111]$ screw dislocation near the other junction node. Thus an entire network glides forward and slip on the low-stressed $(\bar{1}01)[010]$ slip system (m = 0.29) occurs, driven entirely by the ease of glide of $\langle 111 \rangle$ mixed dislocations which are connected to the junction. The slip trace on the surface would only be created by the $a/2[111]$ screw dislocations.

Therefore, the behavior of network is quite different from that of isolated screw dislocations. A network junction occurs via the movement of neighboring $\langle 111 \rangle$ dislocations. Note that this is another mode of operation of anomalous slip.

(a)

(b)

(c)

(d)

(e)
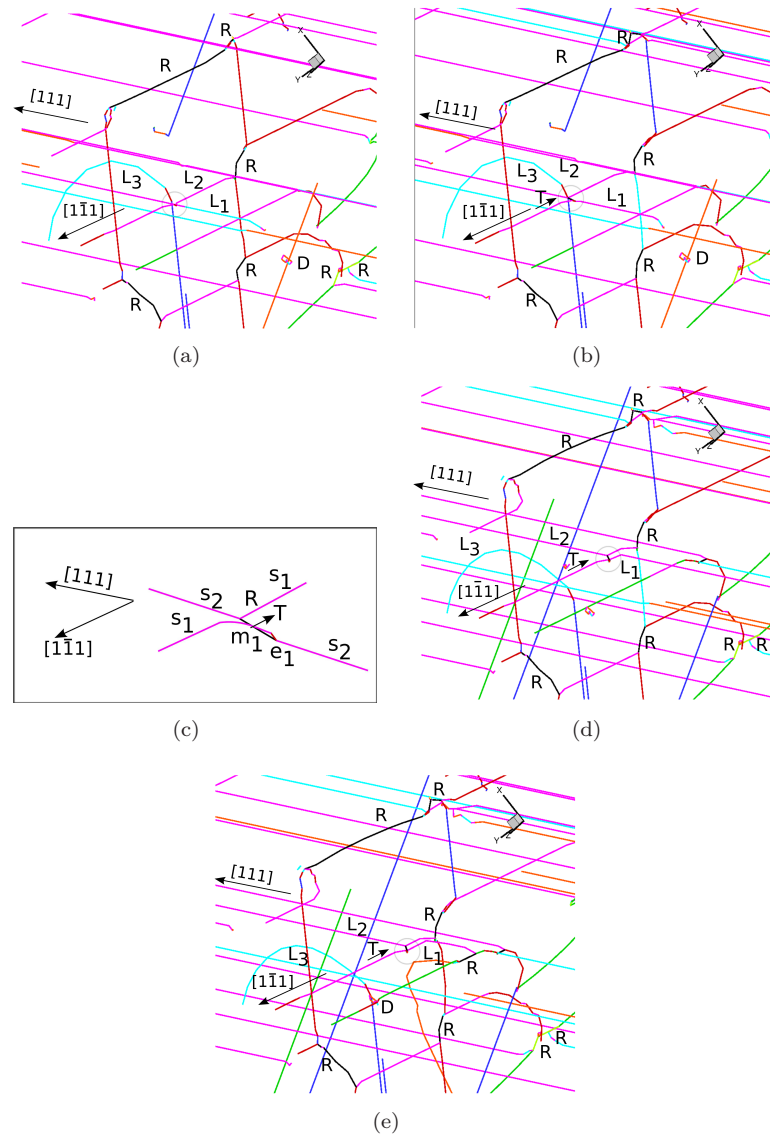
Figure B.2.: A sequence of snap-shots showing the motion of ⟨100⟩ disloca-
tions. Loops L_1, L_2 form a junction in (b) (circled). Other loops in the vicinity are
L_3 and debris loops D. (c) shows the circled region zoomed in, where locally one node
of the junction is connected to mixed ⟨111⟩ dislocation m_1 and the other end of junc-
tion to a/2[111] screw dislocation. The mixed segment drives the junction along the
T direction. The screw part of the loop L_2 glides due to its interaction with the mixed
dislocation m_1. Note that the mixed part m_1 lies on a parallel ($\bar{1}$01) plane and is
connected to the junction with the segment s_1 shown in red. There are several other
reactions **R** with the reactant ⟨111⟩ dislocations in the screw orientation.

C. Appendix C

C.1. Color scheme used in simulations

Table I

Color	Plane
	(110)
	(101)
	(011)
	($\bar{1}$10)
	($\bar{1}$01)
	(0$\bar{1}$1)

Table II

Color	b
	[1$\bar{1}$1]
	[$\bar{1}$11]
	[11$\bar{1}$]
	[111]

Figure C.1.: Table I and II show the color scheme of the dislocation lines according to their habit planes and Burgers vectors respectively.

Bibliography

[1] E. Schmid and W. Boas. Kristallplastizität. springer, berlin. 1935.

[2] J. P Hirth and J. Lothe. *Theory of dislocations*. Wiley, 1982.

[3] M. S. Duesbery. The mechanical properties of the dislocation core. *Contemp. Phys.*, 27(2):145–168, 1986.

[4] J. W. Christian. Some surprising features of the plastic deformation of body-centered cubic metals and alloys. *Metall. Trans. A*, 14:1237, 1983.

[5] V. Vitek. Structure of Dislocation cores in Metallic Materials and its impact on their Plastic behavior. *Prog. Mater. Sci.*, 36:1–27, 1992.

[6] V. Vitek. Atomic level computer modelling of crystal defects with emphasis on dislocations: Past, present and future. *Prog. Mater. Sci.*, 56:577–585, 2011.

[7] P. B. Hirsch. *In 5th Int. Conf. on Crystallography, Cambridge*, 1960.

[8] A. Seeger. The flow stress of high-purity refractory body-centred cubic metals and its modification by atomic defects. *Jour. De Phys. IV*, 5:45–65, 1995.

[9] R. Groeger, A. G. Bailey, and V. Vitek. Multiscale modeling of plastic deformation of molybdenum and tungsten: I. Atomistic studies of the core structure and glide of 1/2<111> screw dislocations at 0 K. *Acta Mater.*, 56:5401–5411, 2008.

[10] R. Groeger, V. Racherla, J. L. Bassani, and V. Vitek. Multiscale modeling of plastic deformation of molybdenum and tungsten: II. Yield criterion for single crystals based on atomistic studies of glide

of 1/2<111> screw dislocations at 0 K. *Acta Mater.*, 56:5412–5425, 2008.

[11] R. Groeger and V. Vitek. Multiscale modeling of plastic deformation of molybdenum and tungsten: III. Effects of Temperature and Plastic strain rate. *Acta Mater.*, 56:5426–5439, 2008.

[12] D. Hull and D. J. Bacon. *Introduction to dislocations.* Butterworth-Heinemann, Oxford, 4th edition, 2001.

[13] E. Orowan. Zur Kristallplastizität. III. Über den Mechanismus des Gleitvorganges. *Z. Phys.*, 89:634, 1934.

[14] M. Polanyi. *Z. Phys.*, 89:660, 1934.

[15] G. I. Taylor. The mechanism of plastic deformation of crystals. Part I. Theoretical. *Proc. Roy. Soc. A*, 145(855):362–387, 1934.

[16] R. Peierls. The size of a dislocation. *Proc. Phys. Soc. Lond.*, 52:34–37, 1940.

[17] M. Peach and J. S. Koehler. The forces exerted on dislocations and the stress fields produced by them. *Phys. Rev.*, 80(3):436–439, 1950.

[18] E. Schmid. Neuere Untersuchungen an Metallkristallen. In Proceedings of the International congress on Applied Mechanics, Delft, 1924, pages 342–353, 1924.

[19] G. I. Taylor and C. F. Elam. The Distortion of Iron Crystals. *Proc. R. Soc. A Lond.*, 112:337–361, 1926.

[20] G. I. Taylor. The deformation of crystals of β-brass. *Proc. R. Soc. A Lond.*, 118:1–24, 1928.

[21] N. P. Allen, B. E. Hopkins, and T. E. McLennan. The tensile properties of single crystals of high-purity iron at temperatures from 100 to -253 degrees C. *Proc. R. Soc. A Lond.*, 234 (1197):221–246, 1955.

[22] J. H. Hoke and R. Maddin. The deformation of molybdenum single crystals in compression. *JMPS*, 5:26–40, 1956.

[23] A. S. Keh. Work hardening and deformation sub-structure in iron single crystals deformed in tension at 298 K. *Phil. Mag.*, 12 (115):9–30, 1965.

[24] A. S. Keh and Y. Nakada. Plasticity of iron single crystals. *Can. J. Phys.*, 45:1101–1120, 1967.

[25] T. L. Altshuler and J. W. Christian. The mechanical properties of pure iron tested in compression over the temperature range 2 to 293° K. *Phil. Trans. R. Soc. Lond. A*, 261:253–287, 1967.

[26] T. Takeuchi. Temperature dependence of work-hardening rate in iron single crystals. *J. Phy. Soc. Jap.*, 26(2):354–362, 1969.

[27] S. Zwiesele and J. Diehl. Temperature and strain rate dependence of the macro yield stress of high purity iron single crystals. 5th International conference on Strength of Metals and Alloys. Pergamon press, 1979.

[28] T. E. Mitchell, R. A. Foxall, and P. B. Hirsch. Work-hardening in niobium single crystals. *Phil. Mag.*, 8 (95):1895–1920, 1963.

[29] J. W. Christian and B. C. Masters. Low-temperature deformation of body-centred cubic metals I. Yield and flow stress measurements. *Proc. Roy. Soc. A*, 281:223–239, 1964.

[30] M. S. Duesbery and R. A. Foxall. A detailed study of the deformation of high purity niobium single crystals. *Phil. Mag.*, 20:166:719–751, 1969.

[31] G. Taylor and J. W. Christian. Experiments on the deformation of niobium single crystals. I. Stress versus strain curves and slip systems in compression and tension. *Phil. Mag.*, 15 (137):873–892, 1967.

[32] G. Taylor and J. W. Christian. Experiments on the deformation of niobium single crystals II. Electronic Microscope study of Dislocation structures. *Phil. Mag.*, 15 (137):893–929, 1967.

[33] D. K. Bowen, J. W. Christian, and G. Taylor. Deformation properties of niobium single crystals. *Can. J. Phys.*, 45:903–937, 1967.

[34] R. A. Foxall, M. S. Duesbery, and P. B. Hirsch. The deformation of niobium single crystals. *Can. J. Phys.*, 45:607–629, 1967.

[35] T. Taoka, S. Takeuchi, and E. Furubayashi. Slip systems and their critical shear stress in 3% Silicon Iron. *J. Phy. Soc. Jap.*, 19:701–711, 1964.

[36] B. Sestak and N. Zarubova. Asymmetry of slip in Fe-Si Alloy single crystals. *Phys. stat. sol.*, 10:239–250, 1965.

[37] N. Zarubova and B. Sestak. Plastic deformation of Fe-3% Si single crystals in the range from 113 K to 473 K-1. Thermally activated plastic flow. *Phys. stat. sol. (a)*, 30:365–374, 1975.

[38] I. Gupta and J. C. M. Li. Stress relaxation, internal stress, and work hardening in some *bcc* metals and alloys. *Metall. Trans.*, 1:2323–2330, 1970.

[39] D. P. Ferriss, R. M. Rose, and J. Wulff. Deformation of tantalum single crystals. *Trans. Met. Soc. AIME*, 224:975–981, 1962.

[40] T. E. Mitchell and W. A. Spitzig. Three-stage hardening in tantalum single crystals. *Acta Metall.*, 13:1169–1179, 1965.

[41] R. J. Arsenault. An investigation of the mechanism of thermally activated deformation in tantalum and tantalum-base alloys. *Acta Metall.*, 14:831–838, 1966.

[42] D. Hull, J. F. Byron, and F. W Noble. Orientation dependence of yield in body-centered cubic metals. *Can. J. Phys.*, 45, 1967.

[43] T. Takeuchi, E. Kuramoto, and T. Suzuki. Orientation dependence of slip in tantalum single crystals. *Acta Metall.*, 20:354–362, 1972.

[44] A. Lawley and H. L. Gaigher. Deformation structures in zone-melted molybdenum. *Phil. Mag.*, 10:15–33, 1964.

[45] F. Guiu and P. L. Pratt. The effect of orientation on the yielding and flow of molybdenum single crystals. *Phys. stat. sol.*, 15:539–552, 1966.

[46] L. Kaun, A. Luft, J. Richter, and D. Schulze. Slip line pattern and active slip systems of tungsten and molybdenum single crystals weakly deformed in tension at room temperature. *Phys. stat. sol*, 26:485–499, 1968.

[47] A. Luft and L. Kaun. Electron microscopic investigation of the dislocation structure in molybdenum single crystals deformed in tension at 293 and 493 K. *Phys. stat. sol.*, 37:781–793, 1970.

[48] K. Kitajima, Y. Aono, and E. Kuramoto. Slip systems and orientation dependence of yield stress in high purity molybdenum single crystals at 4.2 K and 77 K. *Scripta Metall.*, 18:201–205, 1984.

[49] H. W. Schadler. Deformation behavior of zone-melted tungsten single crystals. *Trans. AIME*, 218:649–655, 1960.

[50] R. M. Rose, D. P. Ferriss, and J. Wulff. Yielding and plastic flow in single crystals of tungsten. *Trans. Met. Soc. AIME*, 224:981–990, 1962.

[51] R. G. Garlick and H. B. Probst. Investigation of room-temperature slip in zone-melted tungsten single crystals. *Trans. AIME*, 230:1120–1124, 1964.

[52] A .S. Argon and S. R. Maloof. Plastic deformation of tungsten single crystals at low temperatures. *Acta Metall.*, 14:1449–1462, 1966.

[53] J. R. Stephens. Dislocation structures in single-crystal tungsten and tungsten alloys. *Metall. Trans.*, 1:1293–1301, 1970.

[54] F. Guiu. Slip asymmetry in molybdenum single crystals deformed in direct shear. *Scripta Mater.*, 3:449–454, 1969.

[55] D. Brunner. Temperature dependence of the plastic flow of high-purity tungsten single crystals. *Int. Jour. Mater. Res.*, 8:1003–1013, 2010.

[56] M. S. Duesbery and V. Vitek. Plastic anisotropy in bcc transition metals. *Acta Mater.*, 46(5):1481–1492, 1998.

[57] G. Taylor. Thermally-activated deformation of bcc metals and alloys. *Prog. Mater. Sci.*, 36:29–61, 1992.

[58] E. Furubayashi. Behavior of dislocations in Fe-3% Si under stress. *Jap. J. App. Phys.*, 27:130–146, 1969.

[59] F. Louchet, L. P. Kubin, and D. Vesely. In situ deformation of b.c.c. crystals at low temperatures in a high-voltage electron microscope dislocation mechanisms and strain-rate equation. *Phil. Mag. A*, 39(4):433–454, 1979.

[60] A. Seeger. Why anomalous slip in body-centered cubic metals? *Mater. Sci. Eng. A*, A319-321:254–260, 2001.

[61] D. Brunner and V. Glebovsky. Analysis of flow-stress measurements of high-purity tungsten single crystals. *Materials letters*, 44:144–152, 2000.

[62] D. Brunner. Comparison of flow-stress measurements on high-purity tungsten single crystals with the kink-pair theory. *Mater. Trans. JIM*, 41, 2000.

[63] D. Brunner and J. Diehl. Strain-rate and temperature dependence of the tensile flow stress of high-purity stress α-iron above 250 K (regime I) studied by means of stress-relaxation tests. *Phys. stat. sol. (a)*, 124:155–170, 1991.

[64] D. Brunner and J. Diehl. Temperature and Strain-rate dependence of the tensile flow stress of high-purity stress α-iron below 250 K. Stress/Temperature Regime III. *Phys. stat. sol. (a)*, 124:155–170, 1991.

[65] D. Brunner and J. Diehl. Extension of measurements of the tensile flow stress of high-purity α-iron single crystals to very low temperatures. *Z. Metallkunde*, 83(12):828–834, 1992.

[66] A. Seeger and L. Hollang. The flow-stress asymmetry of ultra-pure molybdenum single crystals. *Mater. Trans. JIM*, 41:1:141–151, 2000.

[67] A. Seeger and U. Holzwarth. Slip planes and kink properties of screw dislocations in high-purity niobium. *Phil. Mag.*, 86 (25-26):3861–3892, 2006.

[68] M. Werner. Temperature and strain-rate dependence of the flow stress of ultrapure tantalum single crystals. *Phys. stat. sol. (a)*, 104(63):63–78, 1987.

[69] B. Sestak and A. Seeger. Gleitung and Verfestigung in kubisch-raumzentrierten Metallen und Legierungen: I. *Z. Metallkunde*, 68:195–202, 1978.

[70] L. P. Kubin. *Dislocations, Mesoscale Simulations and Plastic Flow*. Oxford university Press, 2013.

[71] A. Seeger. Kink theory of the flow stress of body-centered cubic metals. *Z. Metallkunde*, 72:369–380, 1981.

[72] D. Brunner and J. Diehl. The use of Stress-Relaxation Measurements for Investigations on the Flow stress of $\alpha-$Iron. *Phys. stat. sol. (a)*, 104:145–155, 1987.

[73] J. E. Dorn and S. Rajnak. Nucleation of Kink Pairs and the Peierls Mechanism of Plastic Deformation. *Trans. AIME*, 230:1052, 1964.

[74] A. Seeger. On the theory of low-temperature internal friction peak observed in metals. *Phil. Mag.*, 1:651–662, 1956.

[75] A. Seeger. The temperature dependence of the critical shear stress and of work-hardening of metal crystals. *Phil. Mag.*, 45(366):771–773, 1954.

[76] Y. Aono, E. Kuramoto, and K. Kitajima. Plastic deformation of high-purity iron single crystals. *Reports of Research Institute of Applied Mechanics*, XXIX (92):127–193, 1981.

[77] J. Riedle, P. Gumbsch, and H. F. Fischmeister. Cleavage anisotropy in tungsten single crystals. *Phys. Rev. Lett.*, 76:3594–3597, 1996.

[78] P. Gumbsch, J. Riedle, A. Hartmaier, and H. F. Fischmeister. Controlling factors for the brittle-to-ductile transition in tungsten single crystals. *Science*, 282:1293–1295, 1998.

[79] P. Gumbsch. Brittle fracture and the brittle-to-ductile transition of tungsten. *J. Nucl. Mater.*, 323:304–312, 2003.

[80] A. Hartmaier and P. Gumbsch. Thermal activation of crack-tip plasticity: The brittle or ductile response of a stationary crack loaded to failure. *Phys. Rev. B*, 71:024108, 2005.

[81] J. L. Taylor. Slip in tungsten at high temperatures. *Trans. AIME*, 236:464–470, 1966.

[82] N. K. Chen and R. Maddin. Plasticity of molybdenum single crystals. *Trans. AIME*, 10:937–944, 1951.

[83] N. K. Chen and R. Maddin. Slip planes and the energy of dislocations in a body-centered cubic structure. *Acta Metall.*, 2:49–51, 1954.

[84] H. Gough. The behavior of a single crystal of α-iron subjected to alternating torsional stresses. *Proc. Roy. Soc. A*, 118:498–534, 1928.

[85] W. Fahrenhorst and E. Schmid. Über die plastische Dehnung von $\alpha-$Eisenkristallen. *Z. Phys.*, 78:383–394, 1932.

[86] A. Seeger and W. Wasserbäch. Anomalous slip - a feature of high-purity body-centred cubic metals. *Phys. stat. sol. (a)*, 189(1):27–50, 2002.

[87] A. Seeger. Experimental evidence for the 110<->112 transformation of the screw-dislocation cores in body-centred cubic metals. *Phys. stat. sol. (a)*, 201(4):R21–R24, 2004.

[88] D. Brunner and J. Diehl. Temperature and strain-rate dependence of the tensile flow stress of high-purity stress α-iron below 250 K. Stress/Temperature Regime II and its transition to regimes I and III. *Phys. stat. sol. (a)*, 125:203–216, 1991.

[89] D. Caillard. Kinetics of dislocations in pure Fe. Part I. In situ straining experiments at room temperature. *Acta Mater.*, 58:3493–3503, 2010.

[90] D. Caillard. Kinetics of dislocations in pure Fe. Part II. In situ straining experiments at room temperature. *Acta Mater.*, 58:3493–3503, 2010.

[91] A. Luft and L. Kaun. A detailed investigation of slip line pattern and subsurface dislocation structure of molybdenum single crystals. *Phys. stat. sol. (a)*, 18:109–122, 1973.

[92] G. Taylor, R. Bajaj, and O. N. Carlson. Anomalous slip in high-purity vanadium crystals. *Phil. Mag.*, 28(5):1035–1042, 1973.

[93] R. Creten, J. Bressers, and P. De Meester. Anomalous slip in high-purity vanadium crystals deformed in compression. *Mater. Sci. Eng.*, 19:51–53, 1977.

[94] W. Wasserbäch. Anomalous slip in high-purity niobium and tantalum single crystals. *Phys. stat. sol. (a)*, 147:417–446, 1995.

[95] M. H. A. Nawaz and B. L. Mordike. Slip geometry of tantalum and tantalum alloys. *Phys. stat. sol. (a)*, 21:449–458, 1975.

[96] W. Wasserbäch and V. Novak. Optical investigation of Anomalous slip-line patterns in high-purity niobium and tantalum single crystals after tensile deformation at 77 K. *Mater. Sci. Eng.*, 73:197–202, 1985.

[97] W. Wasserbäch. Anomalous slip in high-purity tantalum single crystals after tensile deformation at 77 K. *Phil. Mag. A*, 51(4):619–628, 1985.

[98] H. Matsui and H. Kimura. Anomalous {110} slip in high-purity molybdenum single crystals and its comparison with that in V(a) metals. *Mater. Sci. Eng.*, 24:247–256, 1976.

[99] L. Hsiung. On the mechanisms of anomalous slip in bcc metals. *Mater. Sci. Eng. A*, 528:329–337, 2010.

[100] Veselỳ. The study of Deformation of Thin foils of Mo under the Electron Microscope. *Phys. stat. sol.*, 29:675–683, 1968.

[101] Veselỳ. The study of Slip Bands on the Surface of Mo Single crystals. *Phys. stat. sol.*, 29:685–696, 1968.

[102] M. D. Uchic, D. M. Dimiduk, J. N. Florando, and W. D. Nix. Sample dimensions influence strength and crystal plasticity. *Science*, 305:986–989, 2004.

[103] M. D. Uchic, P.A. Shade, and D. M. Dimiduk. Plasticity of micrometer-scale single crystals in compression. *Annu. Rev. Mater. Res.*, 39:361–386, 2009.

[104] O. Kraft, P. A. Gruber, R. Mönig, and D. Weygand. Plasticity in confined dimensions. *Annu. Rev. Mater. Res.*, 40:293–317, 2011.

[105] J. Kim, D. Jang, and J. R. Greer. Tensile and compressive behavior of tungsten, molybdenum, tantalum and niobium at the nanoscale. *Acta Mater.*, 58:2355–2363, 2010.

[106] A. S. Schneider et al. Correlation between critical temperature and strength of small-scale bcc pillars. *Phys. Rev. Lett.*, 103:105501–4, 2009.

[107] S. Brinckmann, J. Kim, and J. R. Greer. Fundamental differences in mechanical behavior between two types of crystals at the nanoscale. *Phys. Rev. Lett.*, 100:155502(1–4), 2008.

[108] A. S. Schneider, C. P. Frick, B. G. Clark, P. A. Gruber, and E. Arzt. Influence of orientation on the size effect in *bcc* pillars with different critical temperatures. *Mater. Sci. Eng. A*, 528:1540–1547, 2011.

[109] M. Zaiser, J. Schwerdtfeger, A. S. Schneider, C. P. Frick, B. G. Clark, P. A. Gruber, and E. Arzt. Strain bursts in plastically deforming molybdenum micro- and nanopillars. *Phil. Mag.*, 88:3861–3874, 2008.

[110] H. Bei, S. Shim, E. P. George, M. K. Miller, E. G. Herbert, and G. M. Pharr. Compressive strengths of molybdenum alloy micropillars prepared using a new technique. *Scripta Mater.*, 57, 2007.

[111] S. M. Han, G. Feng, J. Y. Jung, H. J. Jung, and J. R. Grooves. Critical-temperature/peierls-stress dependent size effects in body centered cubic nanopillars. *Appl. Phys. Lett.*, 102:041910, 2013.

[112] J. R. Greer, C. R. Weinberger, and W. Cai. Comparing the strength of f.c.c. and b.c.c sub-micrometer pillars: Compression experiments and dislocation dynamics simulations. *Mater. Sci. Eng. A*, 493:21–25, 2008.

[113] A. S. Schneider, B. G. Clark, C. P. Frick, P. A. Gruber, and E. Arzt. Effect of pre-straining on the size effect in molybdenum pillars. *Phil. Mag. lett.*, 90 (11):841–849, 2010.

[114] V. Vitek, R. C. Perrin, and D. K. Bowen. The core structure of $1/2\langle 111 \rangle$ screw dislocations in b.c.c. crystals. *Phil. Mag.*, 21 (173):1049–1073, 1970.

[115] Z. S. Basinski, M. S. Duesbery, and R. Taylor. Influence of shear stress on screw dislocations in a model sodium lattice. *Can. J. Phys.*, 21 (173):1049–1073, 1971.

[116] Von Neumann. Vorlesung über die Theorie der Elastizität. 1885.

[117] F. Minami, E. Kuramoto, and S. Takeuchi. Motion of screw dislocations under stress in a model b.c.c. lattice. *Phys. stat. sol. (a)*, 12:581–588, 1972.

[118] E. Kuramoto, F. Minami, and S. Takeuchi. Computer simulation of motion of screw dislocations in model b.c.c. lattices. *Phys. stat. sol. (a)*, 12:411–419, 1974.

[119] V. Vitek. Core structure of screw dislocations in body-centred cubic metals:relation to symmetry and interatomic bonding. *Phil. Mag.*, 84(3-5):415–428, 2004.

[120] K. Ito and V. Vitek. Atomistic study of non-schmid effects in the plastic yielding of *bcc* metals. *Phil. Mag. A*, 81:1387–1407, 2001.

[121] J. Marian, W. Cai, and V. V. Bulatov. Dynamic transitions from smooth to rough twinning in dislocation motion. *Nat. Mater.*, 3:158–163, 2004.

[122] S. Ismail-Beigi and T. A. Arias. Ab Initio study of screw dislocations in Mo and Ta: A new picture of plasticity in bcc transition metals. *Phys. Rev. Lett.*, 84:1499–1502, 2000.

[123] C. Woodward and S. I. Rao. Ab-initio simulation of isolated screw dislocations in bcc Mo and Ta. *Phil. Mag. A*, 81(5):1305–1316, 2001.

[124] C. Woodward and S. I. Rao. Flexible ab initio boundary conditions: Simulating isolated dislocations in bcc Mo and Ta. *Phys. Rev. Lett.*, 88(21):6402, 2002.

[125] S. L. Frederiksen and K. W. Jacobsen. Density functional theory studies of screw dislocation core structures in *bcc* metals. *Phil. Mag.*, 83 (3):365–375, 2003.

[126] M. Mrovec, R. Gröger, A. G. Bailey, D. Nguyen-Manh, C. Elsässer, and V. Vitek. Bond-order potentials for simulations of extended defects in tungsten. *Phys. Rev. B*, 75:104119, 2007.

[127] M. Mrovec, R. Gröger, D. Nguyen-Manh, D.G. Pettifor, and V. Vitek.

[128] R. Groeger and V. Vitek. Breakdown of the schmid law in bcc molybdenum related to the effect of shear stress perpendicular to the slip direction. *Mater. Sci. Forum*, 482:123–126, 2005.

[129] Q. Qin and J. L Bassani. Non-associated plastic flow in single crystals. *J. Mech. Phys. Solids*, 40(4):835–862, 1992.

[130] Q. Qin and J. L Bassani. Non-associated plastic flow in single crystals. *J. Mech. Phys. Solids*, 40(4):813–833, 1992.

[131] V. Racherla and J. L. Bassani. Strain burst phenomena in the necking of a sheet that deforms by non-associated plastic flow. *Modelling Simul. Mater. Sci. Eng.*, 15(1):S297–S311, 2007.

[132] C. Domain and G. Monnet. Simulation of screw dislocation motion in iron by molecular dynamics simulations. *Phys. Rev. Lett.*, 95:p.215506, 2005.

[133] D. Cereceda, A. Stukowski, M. R. Gilbert, S. Queyreau, L. Ventelon, M. C. Marinica, J. M. Perlado, and J. Marian. Assessment of interatomic potentials for atomistic analysis of static and dynamic properties of screw dislocations in W. *Modelling Simul. Mater. Sci. Eng.*, 25 (8):085702–085721, 2013.

[134] M. S. Duesbery and W. Xu. The motion of edge dislocations in body-centered cubic metals. *Scripta Mater.*, 39(3):283–287, 1998.

[135] W. Cai, V. V. Bulatov, J. P. Chang, J. Li, and S. Yip. *Dislocations in solids*, volume 12, chapter Dislocation core effects on mobility, pages 1–80. Nord-Holland Pub., 2004.

[136] X. Liu, S. I. Golubov, C. H. Woo, and H. Huang. Glide of edge dislocations in tungsten and molybdenum. *Mater. Sci. Eng. A*, 365:96–100, 2004.

[137] M. Yamaguchi and V. Vitek. Core structure of nonscrew $1/2\langle 111 \rangle$ dislocations on {110} planes in b.c.c. crystals I. core structure in an unstressed crystal. *J. Phys. F. : Met. Phys.*, 3:523–536, 1973.

[138] V. Vitek and M. Yamaguchi. Core structure of nonscrew $1/2\langle 111 \rangle$ dislocations on $\{110\}$ planes in b.c.c. crystals II. peierls stress and the effect of an external shear stress on the cores. *J. Phys. F. : Met. Phys.*, 3:537–542, 1973.

[139] K. Kang, V. V. Bulatov, and W. Cai. Singular orientations and faceted motion of dislocations in body-centered cubic crystals. *Proc. Nat. Acad. Sci*, 9:3221–3235, 2012.

[140] R. Groeger and V. Vitek. Explanation of the discrepancy between the measured and atomistically calculated yield stresses in body-centered cubic metals. *Phil. Mag. Lett.*, 87:113, 2007.

[141] P. Guyot and J. E. Dorn. *Can. J. Phys.*, 45:983, 1967.

[142] D. Caillard and J. L. Martin. *Thermally activated mechanisms in crystal plasticity.* Pergamon Press, 2003.

[143] M. Tang, L. P. Kubin, and G. R. Canova. Dislocation Mobility and the Mechanical Response of B.C.C. Single Crystals: A Mesoscopic Approach. *Acta Mater.*, 9:3221–3235, 1998.

[144] U .F. Kocks, A. S. Argon, and M. F. Ashby. Thermodynamics and kinetics of slip. *Prog. Mater. Sci.*, 19, 1975.

[145] L. P. Kubin, G. R. Canova, M. Condat, B. Devincre, V. Pontikis, and Y. Brechet. Dislocation microstructures and plastic flow: A 3D simulation. *Solid state phenomena*, 23 & 24:455–472, 1992.

[146] B. Devincre and M. Condat. Model validation of a 3d simulation of dislocation dynamics: Discretization and line tension effects. *Acta Metall. Mater.*, 40(10):2629–2637, 1992.

[147] L. P. Kubin and G. R. Canova. The modelling of dislocation patterns. *Scripta Metall.*, 27:957–962, 1992.

[148] J. P. Hirth, M. Rhee, and H. Zbib. Modeling of deformation by a 3D simulation of multiple, curved dislocations. *J. Computer-Aided Mater. Design*, 3:164–166, 1996.

[149] H. Zbib, M. Rhee, and J. P. Hirth. On plastic deformation and the dynamics of 3D dislocations. *Int. J. Mech. Sci.*, 40:113–127, 1998.

[150] K. W. Schwarz. Simulations of dislocations on the mesoscopic scale. I. Methods and examples. *J. Appl. Phys.*, 85 (1):108–119, 1999.

[151] N. M. Ghoniem and L. Z. Sun. Fast-sum method for the elastic field of three-dimensional dislocation ensembles. *Phys. Rev. B*, 60(1):128–140, 1999.

[152] N. M. Ghoniem, S. H. Tong, and L. Z. Sun. Parametric dislocation dynamics: A thermodynamics-based approach to investigations of mesoscopic plastic deformation. *Phys. Rev. B*, 61(2):913–927, 2000.

[153] A. Arsenlis, W. Cai, M. Tang, M. Rhee, T. Oppelstrupp, G. Hommes, T. G. Pierce, and V. V. Bulatov. Enabling strain-hardening simulations with dislocation dynamics. *Modelling Simul. Mater. Sci. Eng.*, 15:553–595, 2007.

[154] T. A. Arias and J. D. Joannopoulos. Ab initio theory of dislocation interactions: From close-range spontaneous annihilation to the long-range continuum limit. *Phys. Rev. Lett.*, 73 (5):680–683, 1994.

[155] S. Naamane, G. Monnet, and B. Devincre. Low temperature deformation in iron studied with dislocation dynamics simulation. *Int. J. Plast.*, 26:84–92, 2010.

[156] J. Chaussidon, C. Robertson, D. Rodney, and M. Fivel. Dislocation Dynamics simulations of plasticity in Fe Laths. *Acta Mater.*, 56:5466–5476, 2008.

[157] Z. Q. Wang and I. J. Beyerlein. An atomistically-informed dislocation dynamics model for the plastic anisotropy and tension-compression asymmetry of bcc metals. *Int. J. Plast.*, 10:1471–1484, 2011.

[158] E. Van der Giessen and A. Needleman. Discrete dislocation plasticity: a simple planar model. *Modelling Simul. Mater. Sci. Eng.*, 3:689–735, 1995.

[159] R. De Wit. Some relations for straight dislocations. *Phys. stat. sol.*, 20:575, 1967.

[160] D. M. Barnett. The displacement field of a triangular dislocation loop. *Phil. Mag. A*, 51(3):383–387, 1985.

[161] B. Devincre. Three dimensional stress field expressions for straight dislocation segments. *Solid state comm.*, 93(11):875–878, 1995.

[162] D. Weygand, L. H. Friedman, E. van der Giessen, and A. Needleman. Discrete dislocation modeling in three-dimensional confined volumes. *Mater. Sci. Eng. A*, 310:420–424, 2001.

[163] D. Weygand, L. H. Friedman, E. van der Giessen, and A. Needleman. Aspects of boundary-value problem solutions with three-dimensional dislocation dynamics. *Modelling Simul. Mater. Sci. Eng.*, 10:437–468, 2002.

[164] D. Weygand and P. Gumbsch. Study of dislocation reactions and rearrangements under different loading conditions. *Mater. Sci. and Eng. A*, 400-401:158–161, 2005.

[165] E. Bitzek, D. Weygand, and P. Gumbsch. Atomistic study of edge dislocations in fcc metals: Drag and inertial effects. IUTAM Symposium Mesoscopic Dynamics of Fracture Process and Materials Strength, pages 45–57. Kluwer academic publishers, 2004.

[166] E. Bitzek and P. Gumbsch. Dynamic aspects of dislocation motion:atomistic simulations. *Mater. Sci. Eng. A*, 400-401:40–44, 2005.

[167] R. Groeger. *Priv. Comm.*, 2011.

[168] B. Devincre, L. P. Kubin, C. Lemarchand, and R. Madec. Mesoscopic simulations of plastic deformation. *Mater. Sci. Eng A*, 309-310:211–219, 1996.

[169] D. Rodney and R. Phillips. Structure and strength of dislocation junction: An atomic level analysis. *Phys. Rev. Lett.*, 82(8):1704–1707, 1999.

[170] V. V. Bulatov, F. F. Abraham, L. Kubin, B. Devincre, and S. Yip. Connecting atomistic and mesoscale simulations of crystal plasticity. *Nat. Lett.*, 39:669–672, 1998.

[171] Y. T. Chou. Dislocation reactions and networks in anisotropic b.c.c. crystals. *Mater. Sci. Eng.*, 36:81–86, 1972.

[172] M. Mrovec. *Priv. Comm.*, 2011.

[173] V. V. Bulatov et al. Dislocation multi-junctions and strain hardening. *Nat. Lett.*, 440:1174–1178, 2006.

[174] R. Madec and L. P. Kubin. Second-order junctions and strain hardening in *bcc* and *fcc* crystals. *Scripta Mater.*, 58:767–770, 2008.

[175] W. Hackbusch. *Multi-grid methods and applications.* Springer-Verlag, 1980.

[176] M. Rhee, H. M. Zbib, J. P. Hirth, H. Huang, and T. D. Rubia. Models for long-/short-range interactions and cross slip in 3D dislocation simulation of BCC single crystals. *Modelling Simul. Mater. Sci. Eng.*, 6:467–492, 1998.

[177] D. Brunner. Peculiarities of work hardening of high-purity tungsten single crystals below 800 K. *Mater. Sci. Eng. A*, 387-389:167–170, 2004.

[178] F. Louchet and L. P. Kubin. Dislocation substructures in the anomalous slip plane of single crystal niobium strained at 50 K. *Acta Metall.*, 23:17–21, 1975.

[179] Y. Aono, E. Kuramoto, and K. Kitajima. Orientation dependence of slip in niobium single crystals at 4.2 K and 77 K. *Scripta Metall.*, 18:201–205, 1984.

[180] W. A. Spitzig and A. S. Keh. Orientation and temperature dependence of slip in iron single crystals. *Metall. Trans.*, 1:2751–2757, 1970.

[181] S. Ikeda. Electron microscope observation of dislocation motion in iron at low temperatures. *Jap. J. App. Phys.*, 13(5):779–786, 1974.

[182] S. Ikeno and E. Furubayashi. Behavior of dislocations in niobium under stress. *Phys. stat. sol. (a)*, 12:611–622, 1972.

[183] S. Ikeno. Direct observation of cell formation in niobium by a high-voltage electron microscope. *Phys. stat. sol. (a)*, 36:317–328, 1976.

[184] J. Richter. The influence of temperature on slip behavior of molybdenum single crystals deformed in tension in the range from 293 to 573 K I. Stress-Strain characteristics. *Phys. stat. sol.*, 40:565–572, 1970.

[185] W. Püschl. Reactions between glide dislocations and forest dislocations in anisotropic b.c.c. metals. *Phys. stat. sol. (b)*, 90:181–189, 1985.

[186] J. P. Hirth. On dislocation interactions in the fcc lattice. *J. App. Phys.*, 32 (4):700–706, 1961.

[187] L. K. Wickham, K. W. Schwarz, and J. K. Stölken. Rules for forest interactions between dislocations. *Phys. Rev. Lett.*, 83 (22):4574–4577, 1999.

[188] A. J. Opinsky and J. Smoluchowski. The crystallographic aspect of slip in body-centered cubic single crystals I. Theoretical considerations. *J. App. Phys.*, 22 (11):1380–1384, 1951.

[189] J. D. Baird and B. Gale. Attractive dislocation intersections and work hardening in metals. *Phil. Trans. Roy. Soc. A*, 257:553–592, 1965.

[190] S. M. Ohr and D. N. Beshers. Crystallography of dislocations and dislocation loops in deformed iron. *Phil. Mag.*, 10:219–230, 1964.

[191] G. M. Cheng et al. Dislocations with edge components in nanocrystalline bcc mo. *J. Mater. Res.*, 28 (13):1820–1826, 2013.

[192] H. Matsui and H. Kimura. Anomalous {110} slip and the role of co-planar double slip in *bcc* metals. *Scripta Metall.*, 9:971–978, 1975.

[193] A. J. Garratt-Reed and G. Taylor. Optical and electron microscopy of niobium crystals deformed below room temperature. *Phil. Mag. A*, 39:597–646, 1979.

[194] H. Saka, K. Noda, T. Imura, H. Matsui, and H. Kimura. HVEM in-situ observation of anomalous ($\bar{1}$10) slip in molybdenum. *Phil. Mag.*, 34:33–48, 1976.

[195] F. Louchet and L. P. Kubin. A possible explanation for the anomalous slip of *bcc* metals from *in situ* experiments. *Scripta Metall.*, 9:911–916, 1975.

[196] R. Groeger, K. J. Dudeck, P. D. Nellist, V. Vitek, P. B. Hirsch, and D. J. H. Cockayne. Effect of Eshelby twist on core structure of screw dislocations in molybdenum: atomic structure and electron microscope image simulations. *Phil. Mag.*, 91 (18):2364–2381, 2011.

[197] A. Luft. The correlation between dislocation structure and work-hardening behavior of molybdenum single crystals deformed at 293 K. *Phys. stat. sol.*, 42:429–440, 1970.

[198] H. J. Kaufmann, A. Luft, and D. Schulze. Deformation mechanism and dislocation structure of high-purity molybdenum single crystals at low temperatures. *Crys. Res. Tech.*, 19(3):357–372, 1984.

[199] A. Seeger. Peierls barriers, kinks, and flow stress: Recent progress. *Z. Metallkunde*, 93:651–662, 2002.

[200] R. Madec, B. Devincre, and L. P. Kubin. From dislocation junctions to forest hardening. *Phys. Rev. Lett.*, 89(25):255508–(1–4), 2002.

[201] L. P. Kubin, R. Madec, and B. Devincre. Dislocation intersections and reactions in *fcc* and *bcc* crystals. volume 279, 2003.

[202] R. Madec, B. Devincre, L. P. Kubin, T. Hoc, and D. Rodney. The role of collinear interaction in dislocation-induced hardening. *Science*, 301:1879–1882, 2003.

[203] M. Rhee, D. H. Lassila, V. V. Bulatov, L. Hsiung, and T. D. Rubia. Dislocation multiplication in bcc molybdenum: a dislocation dynamics simulation. *Phil. Mag. Lett.*, 81(9):595–605, 2001.

[204] C. Weinbgerger and Wei Cai. Surface-controlled dislocation multiplication in metal micropillars. *Proc. Nat. Acad. Sci.*, 105:14304–14307, 2008.

[205] A. S. Schneider, B. G. Clark, C. P. Frick, P. A. Gruber, and E. Arzt. Effect of orientation and loading rate on compression behavior of small-scale Mo pillars. *Mater. Sci. Eng. A*, 508:241–246, 2009.

[206] J. Kim and J. R. Greer. Size-dependent mechanical properties of molybdenum micropillars. *Appl. Phys. Lett.*, 93:151916(1–3), 2008.

[207] J. Richter. The influence of temperature on slip behavior of molybdenum single crystals deformed in tension in the range from 293 to 573 K II. Slip geometry and structure of slip bands. *Phys. stat. sol. (a)*, 46:203–215, 1971.

[208] C. Marichal, K. Srivastava, D. Weygand, S. Van Petegem, D. Grolimund, P. Gumbsch, and H. Van Swygenhoven. Origin of anomalous slip in tungsten. *Phys. Rev. Lett.*, 113, 2014.

[209] Veselỳ. The influence of surface orientation on yield in Mo single crystals. *Scripta Metall.*, 6:753–756, 1972.

[210] H. Matsui, H. Kimura, H. Saka, K. Noda, and T. Imura. Anomalous slip induced by the surface effect in molybdenum single-crystal foils deformed in a high voltage electron microscope. *Mater. Sci. Eng.*, 53:263–272, 1982.

[211] D. Kaufmann, A. S. Schneider, R. Mönig, C. A. Volkert, and O. Kraft. Effect of surface orientation on the plasticity of small *bcc* metals. *Int. J. Plast.*, 49:145–151, 2013.

[212] J. Senger, D. Weygand, P. Gumbsch, and O. Kraft. Discrete dislocation simulations of the plasticity of micro-pillars under uniaxial loading. *Scripta Mater.*, 58:587–590, 2008.

[213] H. Matsui and H. Kimura. A mechanism of the "unexpected {110} slip" observed in *bcc* metals deformed at low temperatures. *Scripta Metall.*, 7:905–914, 1973.

[214] G. Taylor. Comments on "a mechanism of the unexpected {110} slip observed in *bcc* metals deformed at low temperatures". *Scripta Metall.*, 8:459–462, 1974.

[215] V. V. Bulatov and W. Cai. Nodal effects in dislocation mobility. *Phys. Rev. Lett.*, 89 (11):115501 (1–4), 2002.

[216] L. Hsiung. Dynamics dislocation mechanisms for the anomalous slip in a single-crystal bcc metal oriented for single slip. Technical Report UCRL-TR-227296, Lawrence Livermore National Laboratory, 2007.

[217] D. Caillard. TEM in situ straining experiments in Fe at low temperature. *Phil. Mag. Lett.*, 89 (8):517–526, 2009.

[218] L. Hollang, D. Brunner, and A. Seeger. Work hardening and flow stress of ultrapure molybdenum single crystals. *Mater. Sci. Eng. A*, 319-321:233–236, 2001.

[219] J. Weertman. Dislocation model of low temperature creep. *J. App. Phys.*, 29 (12):1685–1689, 1958.

[220] J. J. Gilman. Escape of dislocation from bound states by tunneling. *J. App. Phys.*, 39:6086–6090, 1968.

[221] T. Oku and J. M. Galligan. Quantum mechanical tunneling of dislocations. *Phys. Rev. Lett.*, 22 (12):596–597, 1969.

[222] B. V. Petukhov and V. L. Pokrovskii. Quantum and classical motion of dislocations in a peierls potential relief. *Sov. Phys. JETP*, 36 (2):336–342, 1973.

[223] G. Leibfried. *Dislocation and mechanical properties of crystals*, chapter Thermal motion of dislocation lines, pages 495–503. New york:John Wiley, 1957.

[224] G. Alefeld. Rate theory in solids at low temperatures. *Phys. Rev. Lett.*, 12:372–375, 1964.

[225] L. Proville, D. Rodney, and M .Marinica. Quantum effect on thermally activated glide of dislocations. *Nat. Mater.*, 11:845–849, 2012.

[226] T. Suzuki and T. Ishii. *Physics of strength and plasticity*, chapter Dynamical yielding of metals and alloys. Cambridge: MIT Press, 1969.